



**TECHNISCHE
UNIVERSITÄT
WIEN**

Vienna University of Technology

DISSERTATION

Modeling and simulation concepts for advanced braided composites

ausgeführt zum Zwecke der Erlangung des akademischen Grades eines
Doktors der technischen Wissenschaften unter der Leitung von

Assoc.Prof. Dipl.-Ing. Dr.techn. Heinz Pettermann
E317

Institut für Leichtbau und Struktur-Biomechanik

eingereicht an der Technischen Universität Wien

Fakultät für Maschinenwesen und Betriebswissenschaften

von

Dipl.-Ing. Jakob Gager
Matrikelnummer 0425895
Hollitzergasse 2-6/17
1100 Wien

Acknowledgment

This work was carried out in the course of my stay at the Institute of Lightweight Design and Structural Biomechanics (ILSB) at the Vienna University of Technology, hosting a node of my employer, the Competence Center Leoben GmbH (PCCL, Austria). The funding of the PCCL within the framework of the COMET-program by the Austrian Ministry of Traffic, Innovation, and Technology and the State Governments of Styria and Upper Austria is gratefully acknowledged.

I want to express my deepest gratitude to my thesis advisor, Heinz Pettermann, His valuable feedback and positive attitude taught me to think critical and express my ideas. I could not have imagined having a better advisor and mentor for my Ph.D study. Furthermore, I wish to express my special thanks to all members of the ILSB for creating such a friendly and supportive work environment. Special thanks go to Assoc. Prof. Dieter Pahr, Prof. Helmut J. Böhm, and Prof. Franz G. Rammerstorfer as well as to my office mate Grygoriy Kravchenko. Let's not forget Maria Steininger and Gerhard Schneider for being the unofficial heart of the institute.

The micrograph measurements and experimental tests used in the thesis were carried out by the PCCL and its project partner *Institute for Carbon Composites* (LCC) from the Technical University of Munich. The valuable collaboration is gratefully acknowledged. Furthermore, I thank Prof. Gerald Pinter for acting as co-advisor.

In addition, I want to acknowledge the work of the IPython and matplotlib team for providing excellent tools to conduct state-of-the-art research relying on the open-source spirit.

Finally, I would like to thank my family for their support and especially Steffi for being the wonderful person that she is.

Contents

Abstract	IV
Kurzfassung	VI
Notations	VIII
1 Introduction	1
1.1 Length scales	3
1.2 Scope of the present work	4
2 Modeling of Braids and Weaves	6
2.1 Homogenization of fabrics	6
2.2 Failure modeling	19
3 Shell element based modeling	29
3.1 Unit cell based homogenization	30
3.2 Material based assumptions	38
3.3 Rectangular tow cross sections	39
3.4 Lenticular tow cross sections	41
3.5 Multilayer Composites	43
3.6 Braid angles different from 45 degrees	45

<i>CONTENTS</i>	III
4 Application to textile composites	47
4.1 Verification of the rectangular cross section model	48
4.2 Nonlinear behavior of a simplified Twill weave	54
4.3 Verification of the lenticular cross section model	61
4.4 Multilayer composites	64
4.5 Braided composites	73
4.6 Conclusion	87
5 Energy dissipation monitoring	89
5.1 Background	89
5.2 Energy based assessment	91
5.3 Evaluation strategies	96
5.4 Application example	98
5.5 Conclusion on energy dissipation	108
6 Summary	109
A Material parameters	111
B Textile geometries	114
C Load paths distribution	116
Bibliography	118

Abstract

The present thesis focuses on the development of an efficient modeling and simulation concept of braided and woven composites in the framework of the Finite Element Method. Due to the hierarchical nature of such textiles, a detailed representation of the underlying architecture and constituents' behavior is necessary to accurately predict their mechanical response.

To characterize the mechanical behavior of braided textiles in the perspective of material induced nonlinearities, a numerical approach based on homogenization of a periodic unit cell is applied. The common strategy found in the literature, namely continuum element based modeling of such unit cells, suffers from vast computational requirements which puts its economic application with nonlinear simulations into question. To circumvent this drawback, a modeling approach is proposed by which all constituents are discretized with Finite Elements of shell type only, which are connected using surface based couplings. The application of structural elements leads to a pronounced decrease in degrees of freedom without coarsening the discretization. Thus, the simulation time is drastically reduced, retaining accurate results at the same time. Moreover, the surface based coupling allows to incorporate cohesive behavior between the constituents to simulation intraply delamination phenomena.

In order to assess the predictive capabilities of the proposed approach, a verification study is conducted based on linear elastic assumptions comparing the proposed unit cell with a continuum element based one. In this context, the numerical efficiency of the shell element based approach is highlighted. Based on such linear elastic assumptions, the influence of the braiding angle on the elastic properties is investigated as well.

The achieved computational efficiency allows for the simulation of multilayer laminates by modeling the individual layers. This ability is used for studying the influence of different layer stacking and offset schemes on the homogenized elastic properties. Moreover, interlaminar delamination, i.e. delamination between two textile layers, due to in-plane loading is investigated as well.

A major motivation for the development of the present strategy is the possibility of efficient numerical characterization of textile composites taking into account nonlinear constituents behavior. To this end, the shell elements are equipped with an already available elasto-plasto-damage model based on continuum damage mechanics and multi-surface plasticity. By means of this set-up, the nonlinear response of different braids and weaves is predicted and compared with corresponding experimental results.

To apply these mesoscopic results at the structural level accounting for the material nonlinearities, a concept based on energy dissipation assessment is proposed. The concept relies on the evolution of the dissipated energies with respect to proportional loading paths in stress and strain space, respectively, at the unit cell level. This data is precomputed for the investigated textile, stored in a database for later usage. In a second step, it is used during post-processing of linear elastic macroscale simulation results to assess the acting loading state and predict the evolution of the material nonlinearities like damage and plasticity. In this way, various macroscopic structures featuring the same textile plies can be efficiently evaluated beyond the linear elastic regime, requiring only linear elastic simulations at the structural scale. Hence, a computationally efficient evaluation accounting for nonlinear phenomena is achieved. The concept is demonstrated by means of a generic nacelle structure made of a Twill weave carbon/epoxy laminate.

The proposed modeling strategy proves itself as a viable approach to simulate the linear and nonlinear behavior of braided as well as woven composites. In combination with the energy dissipation concept, large scale composite structures can be efficiently assessed beyond the elastic regime without conducting time and resource intensive nonlinear simulations of such structures. This helps to push the numerical evaluation of composites further and supports designing lightweight and safe parts.

Kurzfassung

Die vorliegende Arbeit beschäftigt sich mit der Entwicklung von effizienten Konzepten zur Modellierung und Simulation von geflochtenen und gewobenen Verbundwerkstoffen unter Anwendung der Finiten Elemente Methode. Um genaue Vorhersagen über das mechanische Verhalten treffen zu können, ist hierbei eine detaillierte Abbildung der Geometrie und des Verhaltens der einzelnen Bestandteile notwendig.

Zum Bestimmen des mechanischen Verhaltens eines Geflechts, unter Berücksichtigung von nichtlinearem Materialverhalten, wird eine Homogenisierungsrechnung basierend auf periodischen Einheitszellen durchgeführt. Die dazu, in der Literatur, am häufigsten angewandte Modellierungsstrategie basiert auf Kontinuumselementen. Entsprechende Modelle haben jedoch den Nachteil, dass sie sehr ressourcenhungrig sind und daher ihr Einsatz im Zuge von nichtlinearen Simulationen, im ökonomischen Sinne, eher zweifelhaft ist. Um dieses Problem zu umgehen, wird in der vorliegenden Arbeit ein Modellierungsansatz entwickelt, in dem nur Schalenelemente verwendet werden. Diese Elemente werden entsprechend über ihre Oberflächen gekoppelt und mit passenden Materialgesetzen ausgestattet. Durch die Anwendung dieser Strukturelementen wird die Anzahl der Modellfreiheitsgrade, bei gleichzeitiger Aufrechterhaltung der erzielten Ergebnisgenauigkeit, deutlich verringert. Dadurch reduziert sich auch die benötigte Simulationszeit signifikant. Zudem erlaubt die oberflächenbasierte Kopplung der einzelnen Bestandteile das Einbringen von schädigenden Interfaces und damit die Simulation von Delaminationen innerhalb einer textilen Einzelschicht. Um die Ergebnisqualität des Modellierungsansatzes zu bestimmen, wird zuerst eine Verifikationsstudie unter Annahme linear elastischen Materialverhaltens durchgeführt. Dabei wird die schalenelementbasierte Einheitszelle mit einer kontinuumselementbasierten Zelle verglichen. Diese Simulationen zeigen deutlich die erhöhte Effizienz des entwickelten Ansatzes. In weiterer Folge wird auch unter linear elastischen Annah-

men der Einfluss des Flechtwinkels auf die elastischen Eigenschaften des Verbundes untersucht.

Die erreichte Effizienz erlaubt es neben den Einzelschichten auch ganze Lamine zu simulieren. Dies wird verwendet um den Einfluss des Offsets bzw. des Lagenaufbaues von textilen Laminaten auf deren elastische Eigenschaften zu untersuchen. Durch Einbringen von schädigenden Interfacelementen kann hierbei auch Delamination zwischen zwei Einzelschichten untersucht werden. Einer der Hauptgründe für die Entwicklung der vorgestellten Strategie, ist die numerische Effizienz im Hinblick auf die nichtlineare Simulation von Geflechten. Um derartige Simulationen durchzuführen, wird ein, in einer vorherigen Dissertation entwickeltes, Konstitutivgesetz verwendet, welches basierend auf schädigungsmechanischen Konzepten und der Plastizitätstheorie, das nichtlineare Verhalten von Faserverbundwerkstoffen beschreibt. Entsprechende Simulationen werden für eine Reihe unterschiedlicher Geflechte und Gewebe durchgeführt und die Ergebnisse mit vorhandenen Experimenten verglichen.

Um die so ermittelten mesoskopischen Ergebnisse auf der Strukturebene anwenden zu können, wird in dieser Arbeit auch ein energiebasiertes Konzept vorgestellt. Dieses verwendet die auf Einheitszellenniveau berechneten Entwicklungen der dissipativen Energien zufolge von proportionaler Belastung im Spannungs- und Verzerrungsraum. Diese Energien werden für representative Belastungspfade vorberechnet, in einer Datenbank abgespeichert und während des Post-Processings der linear elastischen, makroskopischen Struktursimulation verwendet um die auftretenden Belastungszustände zu bewerten und entsprechende Vorhersagen über die Entwicklung der einzelnen Nichtlinearitäten zu treffen. Dadurch kann mittels linear elastischer Analyse eine Strukturbewertung über den linear elastischen Bereich hinaus, sehr effizient durchgeführt werden. Das Simulationskonzept wird anhand eines generischen Flugzeugtriebwerksteils, bestehend aus einem Kohlefaser-Epoxy Gewebelaminat, vor-exerziert.

Das vorgestellte Modellierungskonzept erweist sich als ein praktikabler Ansatz um das lineare und nichtlineare Verhalten von textilen Faserverbundwerkstoffen effizient zu simulieren. In Verbindung mit dem energiebasierten Evaluierungskonzept können damit große Verbundstrukturen unter Berücksichtigung von materiellen Nichtlinearitäten bewertet werden ohne diese, unter großem Zeitaufwand, nichtlinear zu berechnen. Somit können Faserverbundbauteile genauer ausgelegt werden was schlussendlich zu leichteren und sichereren Bauteilen führt.

Notations

Abbreviations

FEM	... finite element method
FRP	... fiber reinforced polymer
FPF	... first ply failure
UD	... unidirectional
CLT	... classical lamination theory
DOF	... degree of freedom

Scalars, tensors, and matrices

Throughout this thesis scalar, tensorial, vectorial quantities are addressed using the notation presented in the listing below. The individual components of such vectors or tensors may be addressed by indices. Note, that no distinction is made between physical and mathematical vectors.

Scalar notation

a, b ... scalars

Engineering tensor notation (following Nye [100])

$\mathbf{a}, \boldsymbol{\alpha}$... tensors of rank two using vector notation

\mathbf{A}, \mathbf{B} ... tensors of rank four using matrix notation

General vector/matrix notation

$\underline{\mathbf{a}}, \underline{\boldsymbol{\alpha}}$... vectors

$\underline{\mathbf{A}}, \underline{\boldsymbol{\alpha}}$... matrices

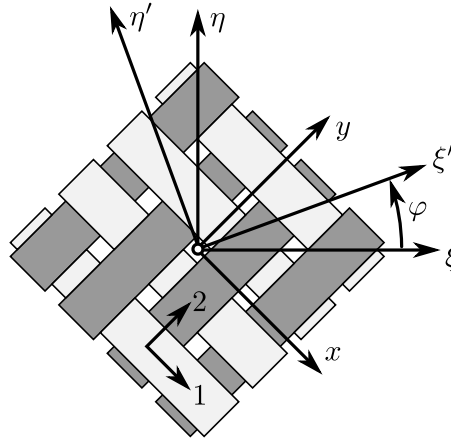


Figure 1: Textile ply with weave coordinate system, $x-y-z$; corresponding braid coordinate system, $\xi-\eta-\zeta$; a local tow coordinate system, $1-2-3$, and an auxiliary coordinate system, $\xi'-\eta'-\zeta'$.

Coordinate systems

In the present work textile fiber reinforced laminates are considered at different length scales. This necessitates the introduction of different coordinate systems. For woven plies a weave coordinate system $x-y-z$ is defined, cf. Fig. 1, aligned with the weft and warp direction. In case of braided textiles the weave coordinate system is not convenient and, therefore, a braid coordinate system $\xi-\eta-\zeta$ is defined as sketched in Fig. 1. Here, ξ denotes the braiding direction, η denotes the in-plane transverse direction, and ζ denotes the out-of-plane transverse direction. Each textile layer consists of multiple tows which feature an orthotropic behavior with the principal directions aligned with the tow coordinate system $1-2-3$. The 1-axis denotes the fiber direction and the 2-axis refers to the in-plane transverse direction. Additionally, auxiliary coordinate systems may be defined with respect to the weave or braid coordinate system indicated by $'$. Typically, these are rotated with respect to the parent system's ζ - or z -axis by angle φ (Fig. 1).

Chapter 1

Introduction

The growing demand for lightweight structures has been pushing the development of laminated composite materials for the last decades. This includes developments in the design, the modeling and simulation, the manufacturing, and the testing of composites. In this context, carbon/epoxy laminates comprising several layers of continuous unidirectional (UD) fibers are especially important due to their exceptional mechanical properties. Such laminates offer high specific stiffness combined with high specific strength and provide the possibility of tailoring the composite properties as required by the prevailing loading of the structure. In contrast to the excellent in-plane properties, laminates suffer from low interlaminar properties, as they do not have any reinforcements in thickness direction [8]. Therefore, they possess low damage tolerance, and are prone to delamination damage. To improve these shortcomings, textile composites can be used. However, the intrinsic complexity of the textile microstructure and the accompanying anisotropic nature of continuous fiber reinforced materials lead to considerable difficulties during the design phase of such textile parts as the prediction of the mechanical performance is not a straight forward task.

Textiles can be classified as woven, non-woven, braided, or knitted, based on the manufacturing technique and fabric architecture [8, 16]. In the present thesis the main focus is set on braided composites, however, due to their intrinsic similarities, braided and woven composites will be considered in the following. Braids (as well as weaves) can be further classified as two dimensional and three dimensional textiles. Here, the dimension indicates the number of possible fiber directions in space, i.e. a three dimensional braid has fibers through the thickness directions. Two dimensional

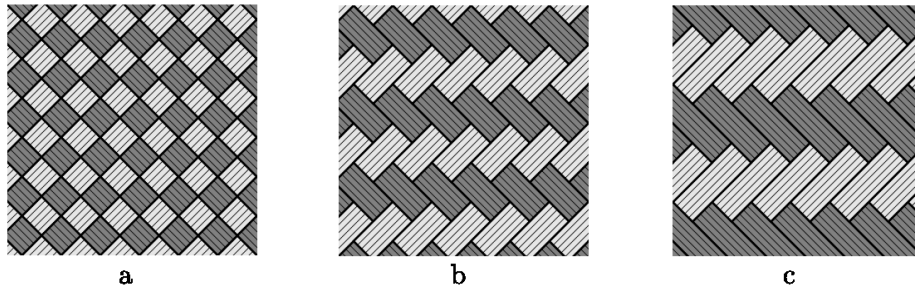


Figure 1.1: Typical biaxial braid (and weave) patterns, Diamond Braid – Plain Weave (1/1) (a), Regular Braid – Twill Weave (2/2) (b), Hercules Braid (3/3) (c).

braids may be further divided in biaxial and triaxial braids. The former feature two in-plane directions of the fiber bundles whereas the latter has tows in three in-plane directions, cf. [16]. Fundamentally, braids can be seen as a hybrid of filament-wound and woven material [5]. It features continuous fibers from one end to the other in combination with the mechanical interlocking. In the perspective of structural shell-like structures, the typically applied braiding techniques is overbraiding [16]. During this process, multiple strands of fibers are simultaneously and reproducibly placed onto a mandrel coiled into a helix. Additionally, these strands are mechanically interlocked due to the special movement of the strand carrying bobbins [5].

The intertwined nature of braids and weaves lead to some distinct features. On the one hand, the fiber undulation in these textiles reduces the in-plane stiffness and strength compared to the non-crimp laminates. On the other hand, the interwoven topology improves fracture toughness, damage tolerance, and out-of-plane properties [8]. Besides these improvements fabrics offer the possibility of cost efficient and fast manufacturing. Modern braiding machines can be used to manufacture preforms without any need for manual ply layup. Lower manufacturing cost and constant layup quality can be achieved. Moreover, there are plenty of different braiding or weaving patterns, each featuring specific properties. Examples for some different biaxial braid patterns are Diamond braids, Regular braids, and Hercules braids, see Fig. 1.1. In the field of woven textile these types are also called Plain weaves, Twill weaves, and Satin weaves [128].

Modern Braiding technique can be used to manufacture a variety of different shapes and is not limited to rope like structures. Some possible areas of application of braided composites are [5]

- pressure vessels,
- jet engine parts,
- wing flaps,
- prosthetics,
- sports, and
- architecture.

In order to fully exploit the advantages of fabrics, it is necessary – among others – to develop modeling approaches and computational methods capable of predicting the stiffness, strength, and nonlinear mechanical behavior of these composites. To this end the property governing mechanisms have to be captured and (at least phenomenologically) modeled by appropriate means. Since the architecture of the textile fabrics can be very complex, many parameters influence their mechanical performance. These parameters include the weaving/braiding pattern, yarn spacing and thickness, fiber volume fraction in the yarn, overall fiber volume fraction, etc. Besides these geometrical parameters, the material and interface properties are also important and a satisfactory model should take their nonlinear behavior into account. Here, the pronounced anisotropy sets additional challenges. Due to the interwoven topology the geometric nonlinearities have to be addressed as well.

1.1 Length scales

Dealing with laminated composites generally implies to distinguish between different length scales, Fig. 1.2. The scale of the fiber diameter (microscale) represents one end of the considered scales. Here, the behavior of the fibers, the matrix, and the fiber/matrix interaction are considered. Using numerically or analytically based homogenization techniques the material characteristics at that length scale can be described in an effective or smeared out way. The other end of the considered length scales is defined by the size of the investigated macro structure (macroscale) and involves the macroscopic loading and boundary conditions. Depending on the specific problem there might be one or more intermediate lengths scales often denoted

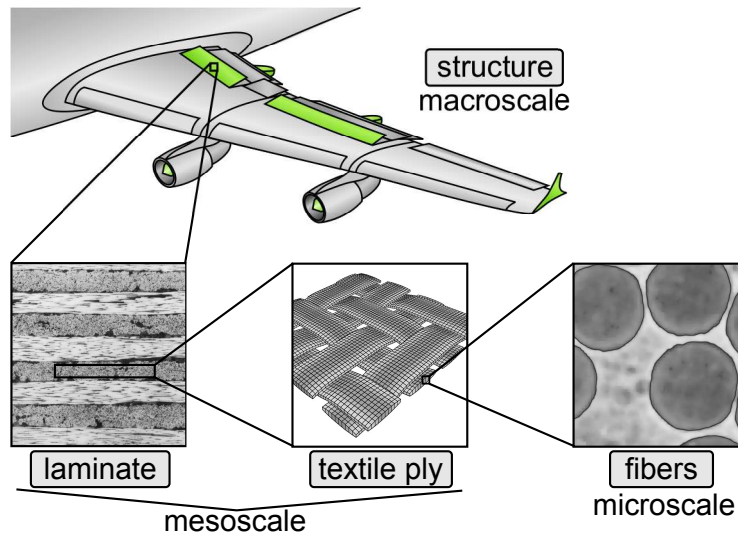


Figure 1.2: Length scales of a composite laminate comprising textile layers; from the macroscale (top¹) via laminate scale (bottom left²) and textile scale (bottom center) to the microscale (bottom right).

as mesoscale. A typical example of such an intermediate length scale is the laminate scale, which incorporates the interaction of individual plies. Here, the classical lamination theory or layered shell formulations are commonly applied. In case of textile laminates a further intermediate length scale can be introduced accounting for the ply's textile architecture. In the following, the term mesoscale will exclusively address this textile scale. Effects present at each of these length scales influence the performance of the laminate and, hence, have to be accounted for in some way.

1.2 Scope of the present work

The main objective of the present thesis is to develop an efficient approach for determining the mechanical properties and assessing the performance of carbon/fiber reinforced two dimensional biaxial braided composites with respect to structural application. This includes stiffness and strengths evaluation as well as the prediction of the nonlinear behavior at the mesoscale. Moreover, this information shall be applicable at the structural scale to allow for the assessment of composite parts. With

¹ Image based on “Control surfaces on airfoil” © 2006 A. Nordmann, used under a Creative Commons Attribution-ShareAlike license: <http://creativecommons.org/licenses/by-sa/3.0/>.

² Image taken from Nettles and Biss [97].

the main focus on the mechanical properties, other commonly found research topics in the field of textile composites like manufacturing simulation, draping simulation, permeability simulations, etc. are not treated here.

Due to the similar topologies and features the proposed techniques, initially intended for braids, will be applicable to two dimensional woven composites as well. Such woven composites might be considered as a special case of $\pm 45^\circ$ braids. Thematically the thesis addresses the two major lengths scales, i.e. the mesoscale and the macroscale. Comments on the possible inclusion of an intermediate laminate scale are given in both sections.

After a brief literature overview, the first (major) part of this thesis deals with a modeling strategy capable of predicting the nonlinear response of textile composites in an efficient manner. The approach is based on mesoscale considerations and is outlined in Chapter 3 using a 2/2 Twill type fabric as a demonstrator. A detailed verification study as well as various linear and nonlinear example simulation are presented in Chapter 4. In Chapter 5, a simulation methodology is proposed connecting the detailed nonlinear material characterization simulations at the mesoscale with large scale, industrial approved, linear elastic simulations (the macroscale). The respective ideas including a demonstrator example are presented.

Chapter 2

Modeling of Braids and Weaves – a literature review

The investigation of the relation between micro- as well as mesostructural features and macroscale properties is an essential topic when assessing new materials. A common technique to determine this relation is to apply homogenization techniques in combination with a separation of length scales assumption. The latter implies that the individual length scales are sufficiently different in size to consider gradients of macroscopic stress or strain fields as being not significant at a smaller length scale, hence, allowing for locally uniform effective (far-field) stresses and strains, respectively [11]. Likewise, the microscopic fields influence the macroscopic behavior only via their volume averages. Accordingly, the microgeometry can be “smeared out” and the resulting homogeneous material properties are applied subsequently to represent this hierarchical material at a larger scale, see Fig. 2.1. The relations linking macroscopic fields with corresponding microscopic ones are called homogenisation and localization relations, respectively. For details the reader is referred to [11]. In the following some ideas of homogenization of textile composites will be given.

2.1 Homogenization of fabrics

Micromechanics based homogenization methods may be divided into three different types, namely analytical, numerical and computational ones [99]. Computational ho-

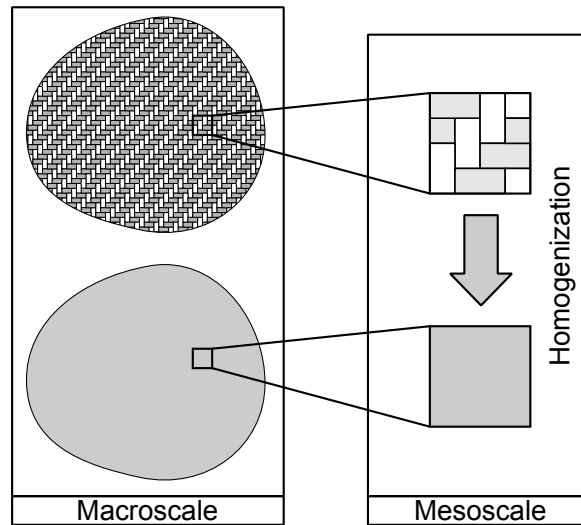


Figure 2.1: Homogenization of a heterogeneous material to derive an effective representation, adapted from [129].

mogenization, i.e. “on the fly” determination of the constitutive behavior, will not be covered here, due to the vast computational requirements, which are currently limited to simple meso- or microscale topologies. For additional information regarding computational homogenization the reader is referred to [21, 52, 53, 99]. In the following sections, some comments on and applications of analytical and numerical approaches will be given. In this context the micromechanical methods may be further divided into statistics based homogenisation models, like mean field approaches or bounding methods and discrete microstructure based models, like periodic microfield approaches [11]. In the perspective of textile composites which typically feature a theoretically periodic topology the latter approaches seem like a natural choice. However, some analytical homogenization models rely on statistical and non-periodic discrete microstructures as will be discussed later. In case of periodic microfield approaches a so called representative volume is chosen which represents all the necessary features of the textile. In the framework of the FEM such a representative volume is called unit cell (UC). Comprehensive reviews on homogenization models for braidings and weaves can also be found in e.g. [6, 25, 121].

The appropriate representation of the textile geometry and topology is a fundamental requirement for all discrete homogenization models, hence, some issues regarding the textile architecture are discussed first.

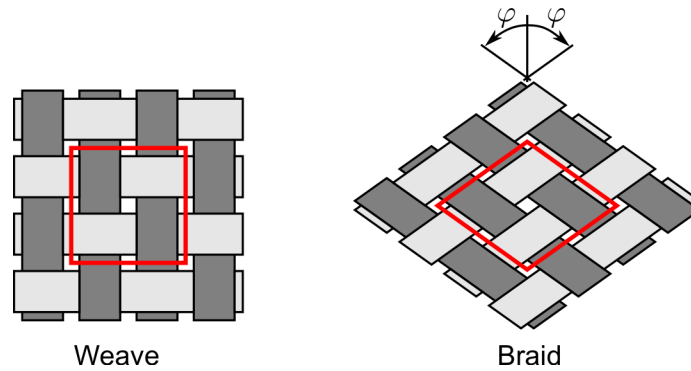


Figure 2.2: Topology of a plain weave (left) compared with a diamond braid (right). For both fabrics a possible repetitive unit cell is marked.

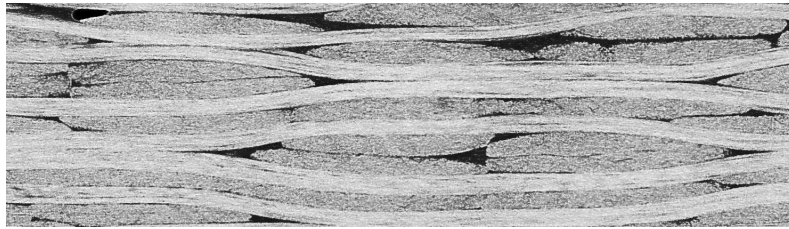


Figure 2.3: Cross section of a $2/2 \pm 45^\circ$ braid aligned with the tow direction extracted from CT data.

2.1.1 Textile architecture

The architecture of the textile is mainly influenced by the topology and the manufacturing parameters. Even though the weaving process and the braiding process are fundamentally different, weaves can be seen as a special form of flat biaxial braidings with perpendicular tow directions, see Fig. 2.2. This enables a generic treatment of both types, as conducted in the present work. Both textiles comprise only two mesoscopic constituents, i.e. the resin impregnated fiber bundles or tows and the unreinforced matrix pockets. Nevertheless, they exhibit a rather complex geometry and topology, see e.g. Fig. 2.3. It shall be noted that throughout this thesis the term geometry addresses the shape of the yarn cross sections and undulation paths, and topology denotes the braiding or weaving pattern.

Depending on the applied homogenization model the complexity of the geometry representation ranges from very simple layer analogy models to highly complex and detailed representations of realistic braidings architectures. Most of these models

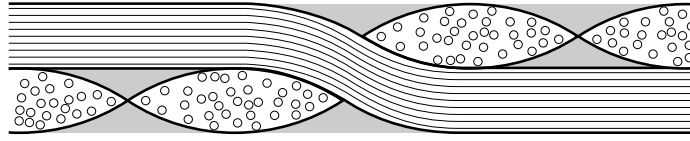


Figure 2.4: Sketch of the idealized tow and matrix geometry of a 2/2 Regular Braid. The matrix pockets are indicated in gray.

rely on informations typically obtained by measurements of polished sections, and use idealized geometry representations (Fig. 2.4) based on analytical expressions. Several groups have proposed such analytical representations for various textile geometries, e.g. [1, 36, 49, 89, 121]. However, the majority of these models represent woven fabrics only. Recently some authors have presented models for braided composites, see e.g. [60, 96, 106]. With respect to modeling, the distance between two parallel tows is an important feature. Depending on the manufacturing parameters, this gap is present or not. Former braids are called open whereas latter are denoted as dense. Dense textiles exhibit a more complicated geometry and most geometric approaches typically cannot model these. Hence, they are commonly approximated by means of open textiles. To make the modeling of fabric geometries easier, software packages have been developed, e.g. *WiseTex* [86] and *TexGen* [123]. These software packages allow for very fast fabric construction of various architectures, based on predefined parametric models. Furthermore, they often feature additional modules for the prediction of elastic properties, or the export of mesh data for subsequent Finite Element computations [138]. The major limitation of such tools is the exclusive construction of continuum element based unit cells. Alternative approaches are not, or only with substantial additions possible [17].

Recently, several research groups have obtained the textile architecture by computed tomography (CT) scanning of composite specimens, see e.g. [7, 112]. A 3D rendering of such a high resolution CT scan (the voxel size equals $7\ \mu\text{m}$) is given in Fig. 2.5. This approach seems very promising as it allows for an accurate representation of the real textile geometry. However, it may need special treatment of the fabrics to enhance the contrast between fibers and matrix, which can influence the behavior of the composite. This is especially true for carbon/epoxy composites [35]. Moreover, the direct derivation of a computational model of such a CT scan is rather laborious. Besides advanced segmentation algorithms with sophisticated tracking methods to



Figure 2.5: Rendering of a CT scan of a 2/2 Twill weave carbon/epoxy textile. Some of the unreinforced matrix pocket material is removed using segmentation tools for the sake of clarity.

identify connected regions a lot of manual intervention is necessary to create a FEM model. A further problem is the automated determination of the fiber orientations of such scanned geometries. Finally, a CT scan can only give an image of a specific spatial point, which is not necessarily representative for the whole composite and is in general not periodic.

As already indicated, the stochastic variability of the geometrical parameters of actual textiles plays an important role when defining corresponding idealized geometries. In [34] CT scans are used to assess some of these uncertainties. A similar approach is applied in [136]. Based on such stochastic data, the characterization can be enhanced using statistics as proposed in e.g. [83, 137, 140].

More or less all textiles in structural application are comprised in multilayer laminates. In this context, the stacking of the fabric layers is an important issue since the in-plane placement as well as a possible deviations in out-of-plane direction effect the laminate properties, see e.g. [71, 83, 85, 104]. The in-plane displacement – often denoted as phase shift – has been shown to directly influence the stiffness of the laminate [69, 70]. However, due to current manufacturing limitations the phase shift cannot be controlled and therefore, leads to some variability of the laminate. The out-of-plane deviation arises from the three dimensional nature of the topology and is called nesting. Nesting leads to a reduction of thickness of the laminate and thus, increases the fiber volume fraction of the laminate [85]. The amount of nesting

depends on the braid angle. Non-perpendicular tows lead to less free space and thus decrease the effect of nesting [85]. In the following nesting effects, albeit present, will not be covered explicitly. In [101] it is shown that the stress distribution is significantly different for layers near the surface of a laminate compared to layers near the center of the laminate. They further have shown that the number of plies influence the effective moduli, however, this effect is not that pronounced. The latter finding has also been reported by other research groups either based on experiments [50] or numerical simulations [45, 82].

Based on such geometrical representations analytical and numerical homogenization models, respectively, are set-up to predict the effective behavior of the investigated textile.

2.1.2 Analytical homogenization models

Analytical models allow for very fast and reasonable accurate predictions of the (in-plane) stiffness of textile composites. However, the prediction of strength values is vague in most cases. Furthermore, the treatment of nonlinearities is available mostly in simplified forms only. The majority of the proposed analytical models is defined for woven composites only, nevertheless, due to the similarities a direct application with braids is straightforward in most cases. A few analytical models are given next.

The most fundamental analytical models may be the classical upper and lower bounds proposed by Hill [65]. As such models do not rely on the actual geometry they give only rough approximations of the effective material properties. In the early 80s, Ishikawa and Chou [68], often called the “pioneers of textile mechanics”, have presented three different models for the prediction of the in-plane elastic properties of 2D woven fabrics based on the classical lamination theory (CLT), namely the *mosaic model*, the *fiber undulation model*, and the *bridging model*. The *mosaic model* divides the composite into different patches of cross ply laminates. These patches are individually treated by CLT and then combined by a stress and strain coupling scheme, respectively to form some upper and lower bounds of the in-plane elastic properties. This model does not consider the fiber undulation and continuity. The second model, the *fiber undulation model*, takes into account the fiber continuity and the undulation of the warp yarn, i.e. the yarn which is supposed to be oriented

in loading direction. The warp yarn is divided into sub-volumes which in-turn are assessed using CLT and combined by means of an iso-stress assumption. However, the ondulation of the fill yarn is not considered. The third model presented, the *bridging model*, is a combination of the former two, especially suited for satin weaves [121] and uses a combination of iso-strain as well as iso-stress couplings. All three models have been also applied to analyze the nonlinear elastic behavior of woven fabric composites [66]. In [95] and [94] these classical models are further extended to account for the ondulation of the warp and weft yarns.

Besides these fundamental models, a different, yet very simple model is the *analogous laminate* model, see e.g. [108]. The composite, braiding or weave, is substituted by individual layers of UD plies representing the tow directions, which are treated by CLT. Puck [108] suggests that a single woven layer should be separated into at least three layers – one for each yarn direction and one representing the matrix. Due to the lack of ondulation the individual ply properties have to be “artificially” adapted using knockdown factors to reasonably represent a textile layer. In [28] a similar approach is used to characterize triaxially braided composites. A model to predict the elastic stiffness properties of triaxially braided composites has been proposed in [12]. The authors used analytical based geometry descriptions and derived the elasticity tensor by appropriate coordinate transformations and volume averaging. More advanced analytical models like *MESOTEX* (MEchanical Simulation Of TEXtiles), see e.g. [120], are capable of predicting elastic properties, damage evolution and effect, as well as strength. Using a Tsai-Wu failure criterion for the tows, a Von-Mises yield criterion for the matrix, and after first ply failure a ply-discount method, the nonlinear behavior of fabrics can be predicted. Based on the concept of the analogous laminate, in [42] an advanced analogous laminate model for biaxial braided composites is derived. The model includes a modified version of the ply damage model proposed in [80] enriched by a matrix plasticity model.

Further analytical methods are, among others the 2D woven fabric strength model based on the method of cells [94], the method of inclusions used e.g. along with *Wise-Tex* [138], the 3D micromechanics model for woven composites [36], a Mori-Tanaka based model proposed in [55], and the micromechanical bridging model developed in [66]. In [126] some reviews of the mentioned analytical models including a juxtapo-

sition with a numerical UC approach is given. Further reviews can be found in [62] and [25].

2.1.3 Numerical homogenization models

The second group of homogenization models is based on numerical computation tools. Since most of the current structural simulations are based on the Finite Element Method (FEM), only models suited for FEM treatment are considered next. Within the framework of the FEM the majority of the approaches rely on a unit cell for the homogenization procedure, i.e. a representative volume unit of the textile is meshed and analysed. The most intuitive – and common – modeling strategy is based on a one-to-one representation of the two constituents using three dimensional continuum elements. In the literature plenty of papers can be found applying this approach to compute the elastic and strength properties of textiles, e.g. [29, 58, 59, 69, 87]. Blacketter et al. [10] was one of the first who included geometric and material induced nonlinearities into such UCs. This continuum element based approach has also been applied to model triaxial braid as proposed by [91, 98, 124]. Recently, biaxial failure envelopes of Twill weaves taking into account progressive tow damage, matrix plasticity, and tow-matrix-delamination are published in [33]. Due to the complex textile geometry, such continuum element based models easily reach a large number of DOFs which in-turn might exceeds computational capabilities. This is especially true in the perspective of nonlinear simulations. Furthermore, the glancing intersections of the tows and matrix pockets leads to distorted elements deteriorating the quality of the FEM results. Figure 2.6 shows such a continuum element based unit cell of a plain weave type textile, with some matrix pocket elements removed for clarity.

The same geometric representations can also be meshed using regular meshes, so called “voxel” meshes [32, 107]. This significantly simplifies the meshing process as only the required material has to be assigned to the particular element. Moreover, CT scan data may be used directly to obtain a detailed representation of the actual geometry. However, the required resolution needs to be high resulting in tremendous voxel meshes. These are typically far beyond the computational capabilities of state-of-the-art workstations and need special servers or super-computers to be usable. A

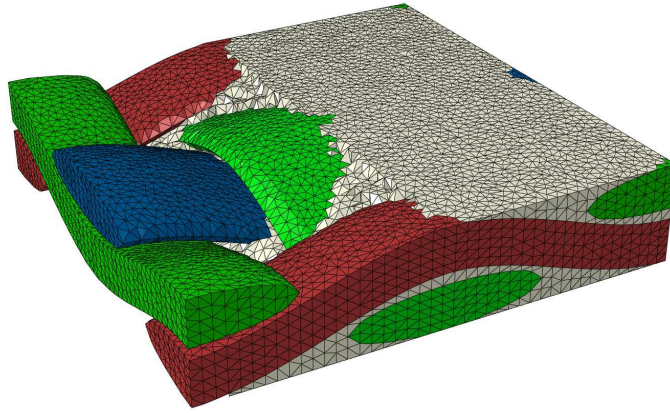


Figure 2.6: Continuum element based unit cell of a plane weave. Some matrix elements are removed highlight the complex internals.

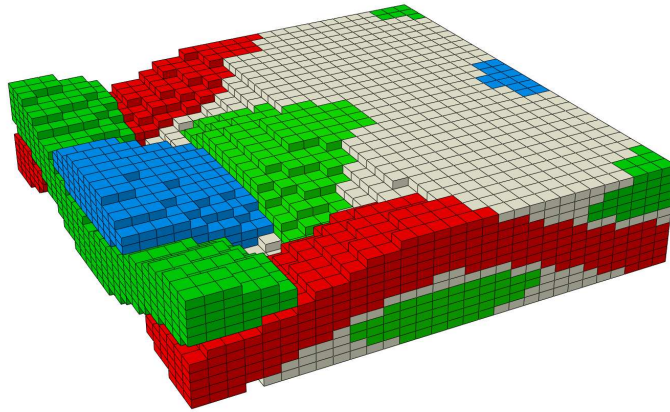


Figure 2.7: Voxel mesh based unit cell of a plain weave, again some matrix elements are removed to highlight the tow paths.

rather coarse voxel mesh of the plain weave shown in Fig. 2.6 is shown in Fig. 2.7. Again some matrix elements are removed for clarity.

To cope with the problems of high number of DOFs and distorted elements present in these classical continuum element based models, various approaches have been presented in the literature. A few of them will be discussed next.

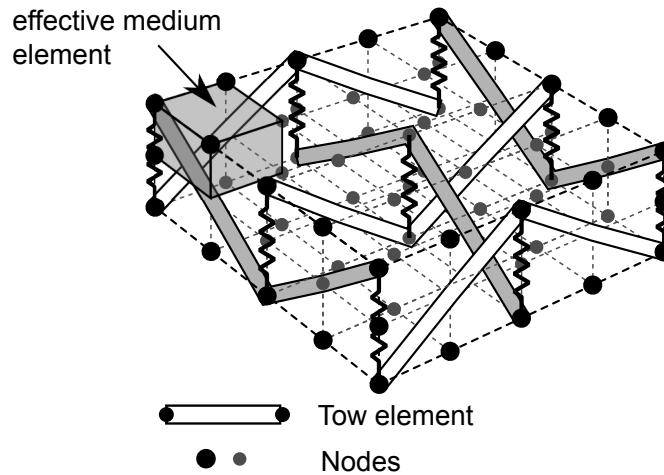


Figure 2.8: Sketch of the Binary Model of a woven composite [22].

Cox et al. [22] and [143] developed the so-called *Binary Model*, see Fig. 2.8. In this model the axial properties of the tows are represented by two-noded truss elements, and the transverse stiffness, the in-plane shear stiffness, and the Poisson's effects of the composite are represented by solid “effective medium” elements. The material data for both material types are derived by micromechanical models. The FEM mesh of the effective medium is a regular one occupying the whole unit cell space. To account for the surplus of effective matrix material the stiffness of the tow material is reduced adequately. The tows and the effective medium elements are connected by appropriate spring couplings. This approach allows for a simple mesh generation even for complex textile architectures since no special treatment of distorted elements is necessary. In [144] the binary model is applied to predict the ultimate strength of textile composites. Similar to the binary model, the *parallelogram spring model* has been developed to deal with 2D braided composites [130]. This model utilizes 1D spring elements as well as solid elements for discretizing the fabric unit cell. A further enhancement of the binary model is proposed in [17] which uses beams instead of trusses to model the embedded tows. This way the bending stiffness of the tows can be represented more accurately. Following the basic idea of the binary model, the *Domain Superposition Technique*, see Fig. 2.9 has been proposed in [72]. Like the binary model, this approach models the matrix material by a regular FEM mesh. However, the tows are represented by volume elements too, instead of the truss elements used in the binary model. This leads to the problem of overlapping areas of the tow and matrix elements. Nevertheless, the tow cross section and ondulation

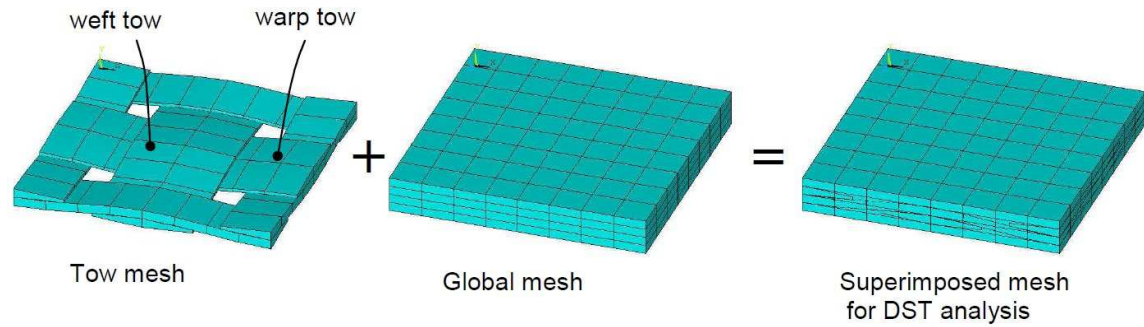


Figure 2.9: Domain Superposition Technique applied to a plain weave unit cell, taken from [72].

can be modeled in a more realistic way. The coupling of the tows with the regular matrix elements needs special attention.

In [75, 76] a fabric unit cell discretization scheme has been proposed applying eXtended Finite Elements (XFEM), see Fig. 2.10. The interfaces between the tows and matrix pockets are realized using an enrichment function within the element definition. With this method a simple regular mesh can be used, and only the elements containing one or more interfaces have to be enriched appropriately. Due to the application of special elements the approach needs a lot of development and implementation work. In [92] a similar XFEM based approach is applied to represent complex microstructures including textiles. A *plate model* for modeling plain woven fabrics has been proposed in [77]. The tows and the adjacent matrix pockets (see Fig. 2.11) are represented by layered shell elements. Two of these layered shell elements form the total thickness of the plain weave. Between their reference planes a single layer of continuum elements is placed to model a thin layer of matrix material. These user defined continuum elements share the nodes of the shell elements and thus, have to account for the shell kinematics implicitly. They allow for the computation of the interface loads. To predict the strength of the fabric, the degradation of the tows is simulated by stiffness reduction factors.

Various other methods are reported in the literature like the postprocessing method [142] (applying macro element formulations), the finite multiphase element method [15], or the dry fabrics simulation based on individual fiber treatment [37, 139].

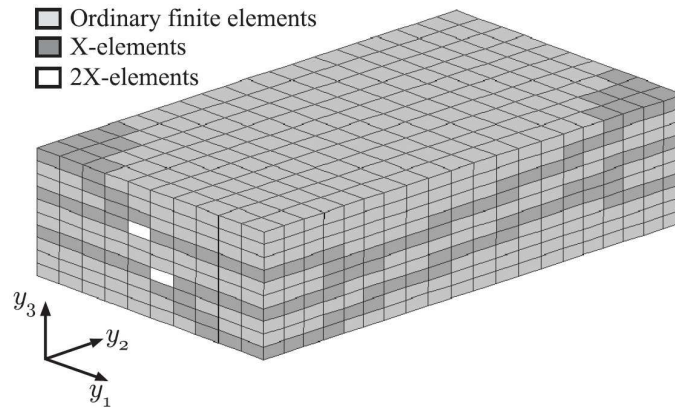


Figure 2.10: Mesh for the XFEM based fabric simulation, taken from [76].

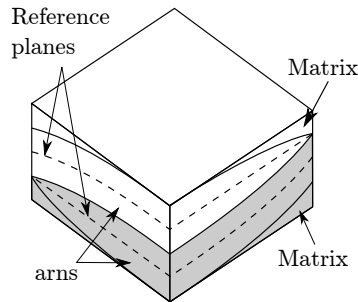


Figure 2.11: Sketch of the plate model [77], quarter of plain weave unit cell with two plate elements (gray, white). The shell reference planes are indicated as dashed lines.

In the present thesis a shell element based modeling strategy is proposed aiming at an efficient treatment braided and woven composites. The strategy is discussed in Sec. 3 and published in [44, 45, 47].

2.1.4 Boundary conditions

Besides the appropriate geometrical description the application of reasonable boundary conditions is a crucial point when setting up homogenization models. Proper boundary conditions allow for minimizing the unit cell size and, thus, allow for efficient computation. One may distinguish between in-plane and out-of-plane boundary conditions. Starting with the in-plane ones, most of the numerical models apply symmetry and periodic boundary conditions, respectively, describing a representa-

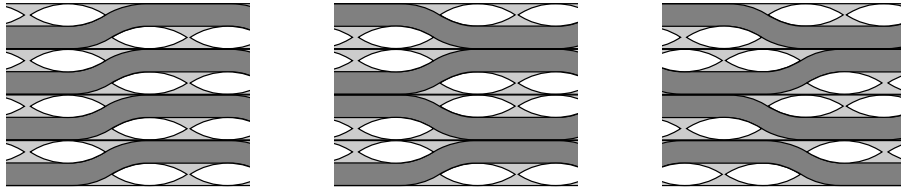


Figure 2.12: Sketch of woven laminate cross sections with in-phase (left), out-of-phase (middle) and random (right) ply stacking.

tive volume element of a infinitely large textile plate, see e.g. [11]. A combination of periodic and symmetry boundary conditions can be used to further decrease the size of the textile unit cell, see e.g. [31]. A similar approach is proposed in [58]. Pahr and Rammerstorfer [103] proposed periodic boundary conditions to represent plane periodic media. These boundary conditions account for global bending and twisting of a shell-like structure, and thus, implicitly assume a plane stress assumption in thickness direction. Geers et al. [52] and Coenen et al. [21] proposed similar plane periodic boundary conditions based on higher-order homogenization in the framework of computational homogenization are published in [52] and [21].

The second type of boundary conditions, i.e. the out-of-plane ones, are especially important in the perspective of multilayer laminates, which is actually the common case. Here, a further source of complexity appears, i.e. the influence of adjacent layers.

Various approaches can be found in the literature to account for the influence of adjacent layers. A common strategy is to apply distinguished out-of-plane boundary conditions to the single layer unit cell representing the “extreme” cases of in-phase and out-of-phase stacking, see Fig. 2.12. The former are realised by utilizing periodic boundary conditions in thickness direction, whereas the latter ones can be attained by symmetry boundary conditions, see e.g. [33, 71]. The respective effective responses are treated as some upper and lower estimates, respectively.

In [70] an advanced set of boundary conditions has been proposed which mimic the constraint applied by adjacent layers. These boundary conditions allow for the distinction of different positions of the ply within the laminate, arbitrary interply shifts and user-defined numbers of layers. The approach is based on scaled out-of-plane displacements of the textile applied as boundary conditions, see [69, 70].

A less widespread but also possible approach is the explicit modeling of multiple layers within the unit cell [70, 83]. The approach is heavy in computational demands and thus, often restricted to a coarse mesh and linear elastic simulation. However, a physical interaction of the individual layers can only be ensured if all layers are present within the model. This is especially true if nonlinear phenomena like, damage and delamination are of interest.

2.2 Failure modeling of UD-like composites and interfaces

Owing to the multi-scale nature of textile composites, the individual constituents at the mesoscale, i.e. the tows and unreinforced matrix pockets, use effective material representation. In most cases the impregnated fiber bundles (tows) are treated like classical UD composites, cf. [23, 84]. Therefore, various approaches are available to compute the respective smeared out material properties. To represent UD plies several models have been published featuring elastic, elastic-plastic [124], hypo-elastic [7], as well as ply failure and damage behavior [41]. For the unreinforced matrix pockets, a common approach is to use the bulk properties of the resin material. Note that detailed investigation of the unreinforced matrix pockets would require the simulation of curing in a non-uniform temperature distribution, which leads to highly heterogeneous residual stress fields and material properties, as stated in [124].

This section deals with material models originally developed for UD plies to predict the anisotropic nonlinear behavior and strength of fibrous materials as well as available interface models. Within the framework of laminated composites two fundamentally different failure modes are distinguished as being intra-laminar and inter-laminar failure. Former describes failure modes present within the individual plies. Here, fiber- and matrix dominated modes are targeted. The second type, inter-laminar failures, appear between the plies, typically in form of interface delamination. Both types require different approaches which will be briefly addressed in the following, starting with the intra-laminar ones.

2.2.1 Intra-laminar damage modeling in FRP composites

As already stated, a rather common approach is to treat the tows like UD plies. This way, the nonlinear material models, published over the years can be used within the textiles. The core of the any material model is the constitutive law linking the stresses increments and strains increments. This link may become nonlinear at elevated loads accounting for some material degradation or yielding effects. Classically, material models for fiber reinforced polymer (FRP) plies are implemented in a plane stress formulation as they are commonly used for shell-like structures. However, when applied to three dimensional textile composites, especially braids and weaves, the plane stress formulation cannot capture the out-of-plane behavior. Depending on the modeling approach employed, a triaxial formulation of the constitutive law may be required, as proposed in [58]. Several research groups have implemented such triaxial damage models to predict the nonlinear response of textiles, see e.g. [24, 58, 86, 127]. All these models are used in conjunction with a three dimensional continuum element based discretization of the textile unit cell. Since the aspired modeling strategy is based on Finite Elements of shell type implying a plane stress state, a plane stress formulation is sufficient, in the present work. Numerous material models for FRP plies featuring a plane stress formulation and allowing for stiffness degradation can be found in the literature, see e.g. [9, 51, 117]. Some of these are further equipped with plasticity models to allow for strain accumulation as well [39, 58, 118]. Latter is important if pronounced in-plane shear or transverse compressive stresses arise as shown e.g. in [134].

The considered approaches for the degradation of the stiffnesses are based on continuum damage mechanics or related methods. In the following, some general remarks on damage models are given. Afterwards, special focus is laid on the damage model for UD plies readily available in the general purpose FEM program Abaqus/Standard v6.12 (*Dassault Systèmes Simulia Corp., Providence, RI, USA*), denoted as *ED-model*, and the model proposed in [116] and [38] denoted as *EPD-model*. Since all considered damage model assume a plane stress state, the term transverse denotes the direction in-plane, perpendicular to the fibers in the following.

The prediction of the nonlinear behavior and strength of fiber reinforced composites is a demanding topic, which is still heavily investigated. Various research groups have worked on this topic for the last decades, proposing numerous approaches. The

simplest approach to obtain “strength informations” is to apply a First Ply Failure (FPF) criterion combined with a linear elastic constitutive law. These criteria predict the load level at which the first intra-laminar failure occurs (or are assumed to occur) in the ply. They are widely used and implemented in most commercial FEM codes. Basically, they are given in terms of analytical equations either based on geometrical fitting or phenomenological based methods, to evaluate the laminate based on the currently acting loading state. Due to their analytical nature FPF criteria allow for fast evaluations, and thus, are often used during the initial design stage. Since the first appearance of failure within a laminated structure is not necessarily associated with the ultimate failure, the FPF method leads to conservative designs for many load cases.

There are numerous FPF models available categorized into two groups which are the generalized failure criteria and physically based criteria. Prominent representatives of the former are the maximum stress [73] and maximum strain criteria [73] or polynomial based ones like Tsai-Wu and Tsai-Hill, respectively, [131]. Published physically based criteria are e.g. the Hashin [63], Puck [108], Cuntze [26] or LaRC [105] criterion. The majority of the FPF criteria in use are the generalized ones, since they require only standard engineering ply properties which are easier to obtain. A comprehensive overview of FPF criteria can be found in e.g. [67]. The nonlinear response of a laminated structure cannot be predicted by FPF criteria, since they are applied as postprocessing routines after the simulation was conducted. The current thesis does not directly deal with FPF criteria, but they act as damage initiation criteria within the damage models considered.

A more sophisticated way to predict the strength of a material is to simulate its degradation and resulting nonlinear behavior until failure, or until a certain critical value is reached. Such simulations provide additional information about the nonlinear response, but require more advanced material models, and material data, at the same time. The simulation of the degradation can be achieved by applying continuum damage mechanics. Typical damage models comprise two main parts. The first part is the damage initiation criterion, also known as damage activation criterion or failure criterion. This criterion is necessary to assess the damage onset based on the prevailing stress and strain state, respectively. The second part is the degradation model which deals with the damage evolution and the resulting material degradation.

Basically, all FPF criteria can be used as initiation criterion, and various degradation models can be found in the literature.

Initiation criterion

As already mentioned, most damage models use a FPF criteria to predict the onset of material damage. The two groups of FPF introduced before, generalized and physically based criteria are also denoted as *mode independent* and *mode dependent* initiation criteria in this context, see [51]. Mode independent criteria do not directly identify the failure mode, they merely assess the severity of the loading state based on one scalar equation. A widely used mode independent criterion is the Tsai-Wu criterion (see e.g. [3]), defined as

$$F_{ij} \sigma_i \sigma_j + F_i \sigma_i \leq 1 . \quad (2.1)$$

Here, F_i and F_{ij} are strength parameters, and σ_i and σ_j are the components of the vector of stress components, see e.g. [3]. This criterion can be seen as a generalization of the Tsai-Hill and Hoffmann criterion. If desired, the identification of the failure mode is possible by introducing failure indices, see e.g. [67]. Mode dependent criteria use different equations for the assessment of different failure modes. Typically a distinction is made between matrix and fiber failure in tension as well as in compression and shear induced damage is commonly captured by additional terms in the matrix or fiber damage formulations, see e.g. [110]. Two notable mode dependent failure criteria are the criterion proposed by Hashin [63], and the one developed by Puck and Schürmann [109]. The former evaluates the stress state within the *ED-model* and the later is used in a plane stress version within the *EPD-model*.

To assess the onset and progression of damage, many models apply some “effective” stress tensor. The link between the effective and nominal stresses can be postulated, e.g. within the *ED-model*, see [88], or determined based on the principle of strain equivalence. Before damage initiates the effective stress and the nominal stress tensor are typically equal. Based on the formulation and implementation the use of an effective stress tensor may lead to some inaccuracies, see e.g. [118]. Hence, not all models rely on effective stresses to evaluate the damage onset and progression, e.g. the *EPD-model*.

Degradation models

The degradation model deals with the damage evolution and the accompanying degradation of the material properties. Two types of degradation models can be distinguished. There are *sudden degradation models* and *gradual degradation models*, see [51]. In sudden degradation models specific entries of the elasticity tensor are reduced instantaneously to zero or some fraction of the undamaged values if the initiation criterion predicts damage. Hence, no particular damage evolution is modeled. The simplest sudden degradation model is the *total ply discount method*, where all moduli are reduced to zero. Modifications of the total ply discount method reduce only selected moduli to zero based on the acting loading state. A comprehensive review of sudden degradation models can be found in [51].

In gradual degradation models one or more stiffness values are gradually reduced following a functional relation with respect to an evolving variable. Typically, some strain or stress measure is used to describe the evolution of so called damage variables. These variables grow during the load increase and act on the elasticity or compliance tensor. Depending of the type of damage model applied there are scalar, vectorial, or tensorial damage variables. Many of the gradual degradation models are reviewed in [51].

In the following, two damage models particularly important for the present work will be discussed more thoroughly.

2.2.2 FRP damage model available in Abaqus (*ED-model*)

The damage model for continuous FRP plies which comes with the commercial FEM code Abaqus/Standard v6.12 predicts the damage onset based on the Hashin criterion [63]. It features an elastic brittle damage behavior, i.e. after the elastic regime, a linear strain softening formulation degrades the material properties, and assumes no plastic deformation. The model was originally developed in [81] and is only applicable to plane stress elements. It applies an effective stress tensor formulation to evaluate the damage initiation and propagation. The vector of effective stress components,

$\hat{\boldsymbol{\sigma}} = [\hat{\sigma}_{11}, \hat{\sigma}_{22}, \hat{\tau}_{12}]^T$, and the vector of true stress components, $\boldsymbol{\sigma} = [\sigma_{11}, \sigma_{22}, \tau_{12}]^T$, are linked by the damage operator matrix, $\underline{\underline{\mathbf{M}}}$, as

$$\hat{\boldsymbol{\sigma}} = \underline{\underline{\mathbf{M}}}\boldsymbol{\sigma} . \quad (2.2)$$

Here, direction 1 refers to fiber direction and direction 2 denotes the transverse direction. Prior to any damage initiation the damage operator matrix equals the identity matrix, thus, the effective stress tensor equals the true stress tensor. But once, the damage initiates and evolves for at least one mode, the damage operator becomes significant in the damage criterion.

The Hashin damage criterion considers four different damage mechanisms, or modes. Fiber tension, fiber compression, matrix tension, and matrix compression are distinguished and treated separately, see [64]. All of these damage modes effect their corresponding damage variables. Depending on the parameters, the individual modes capture the shear loading as well. The damage operator matrix is defined as

$$\underline{\underline{\mathbf{M}}} = \begin{pmatrix} \frac{1}{1-d_f} & 0 & 0 \\ 0 & \frac{1}{1-d_m} & 0 \\ 0 & 0 & \frac{1}{1-d_s} \end{pmatrix} , \quad (2.3)$$

with the internal damage variables d_f , d_m , and d_s . The damage variables d_f and d_m can have different values for tension and compression, which will be denoted by subscripts t and c. Here, the shear damage variable, d_s , is directly related to the other damage variables as

$$d_s = 1 - (1 - d_{ft})(1 - d_{fc})(1 - d_{mt})(1 - d_{mc}) . \quad (2.4)$$

The evolution of the damage variable for each individual mode is characterized by the respective critical dissipated fracture energy (G_c), and directly controlled by the equivalent displacements as,

$$d_i = \frac{\delta_{i,\text{eq}}^f (\delta_{i,\text{eq}} - \delta_{i,\text{eq}}^0)}{\delta_{i,\text{eq}}^f (\delta_{i,\text{eq}}^f - \delta_{i,\text{eq}}^0)} , \text{ with } i \in \{\text{ft}, \text{fc}, \text{mt}, \text{mc}\} . \quad (2.5)$$

Here, δ_{eq}^0 is the equivalent displacement at damage initiation, and δ_{eq}^f is the equivalent displacement at which the material is completely damaged. The equivalent displacements are computed for each damage mode following the equations given in [64]. For example the equivalent displacement and the equivalent stress in the matrix tension regime are expressed as

$$\delta_{\text{mt,eq}} = L^c \sqrt{\langle \varepsilon_{22} \rangle^2 + \varepsilon_{12}^2} \quad , \quad (2.6)$$

$$\sigma_{\text{mt,eq}} = \frac{\langle \sigma_{22} \rangle \langle \varepsilon_{22} \rangle + \tau_{12} \varepsilon_{12}}{\delta_{\text{eq}}^{\text{mt}} / L^c} \quad . \quad (2.7)$$

The $\langle \rangle$ represents the Macaulay bracket operator, defined for every $x \in \mathbb{R}$ as $\langle x \rangle = (x + |x|)/2$. To reduce the mesh dependency in the softening regime a characteristic length, L^c , is introduced. This approach is known as mesh adjusted softening. Furthermore, the model features viscous regularization capabilities to improve the convergence behavior of the implicit solution scheme.

As shown in [118] this model is, strictly speaking, applicable to single layer composites only. The stresses in the damaged elements tend to zero which is only valid for the failed area, and not for the finite area represented by the element undergoing degradation. Nevertheless, preliminary simulations show that the model predicts reasonable results for load cases without pronounced plastic deformation, i.e. without dominant in-plane shear and transverse compressive stresses.

2.2.3 Elasto-plasto-damage model (*EPD-model*).

The second damage model considered is a phenomenological constitutive law for unidirectional FRP plies proposed by Flatscher and Pettermann [39]. Here, the nonlinear material description comprises elastic, plastic, and damage characteristics including softening. The implemented damage model accounts for stiffness degradation attributed to microscopic brittle matrix cracking, fiber/matrix debonding, as well as progressive fiber failure. The model distinguishes between distributed damage, i.e. stiffness degradation accompanied by strain hardening, and localized damage, i.e. stiffness degradation accompanied by strain softening.

The onset of distributed damage is predicted by recourse to the FPF criterion defined by Puck [108] in the plane stress formulation. Besides the prediction of damage

onset the criterion allows for determination of the failure modes including the so called *fracture plane*, i.e. the plane parallel to the fiber direction with the highest risk of failure, see [111]. Applying this criterion the factors of exertion in fiber and transverse to the fiber direction can be computed which in-turn are used to evaluate the damage variables for the individual damage modes. Here, one damage variable is used to describe the fiber dominated phenomena (damage in fiber direction), and three damage variables are used to describe the matrix dominated phenomena (damage perpendicular to the fiber direction). Damage in fiber direction directly leads to strain softening, whereas damage in the transverse direction, features strain hardening followed by strain softening. The evolution of the damage variables for the matrix dominated phenomena is controlled by the analytical function

$$\xi^{(m)} = k_d^{(m)} \left(f_E^{(m)} - 1 \right)^2, \quad (2.8)$$

with the evolution parameter $k_d^{(m)}$, and the factor of matrix exertion $f_E^{(m)}$. Taking into account the predicted fracture plane angle the individual damage variables are derived from $\xi^{(m)}$ as given in [39]. Based on these damage variables the compliance tensor of the damaged ply material is computed applying micromechanical ideas based on the Mori-Tanaka method, cf. [38] and [116]. To this end the damage variables are interpreted as volume fractions of fictitious inhomogeneities (voids) embedded in the material, denoted as populations. The resulting homogenized compliance tensor represents the compliance tensor of the damaged material point and is computed as

$$\mathbf{C} = \left(\mathbf{I} + \sum_p \mathbf{D}^{(p)} \right) \mathbf{C}^{(0)}, \quad (2.9)$$

where $\mathbf{C}^{(0)}$ is the compliance tensor of the undamaged ply material and \mathbf{I} stands for the symmetric fourth order identity tensor. The tensor $\mathbf{D}^{(p)}$ denotes a fourth order tensor associated to the population p which reads

$$\mathbf{D}^{(p)} = \frac{\xi_p}{1 - \xi} \left[\mathbf{I} - \mathbf{S}^{(p)} \right]^{-1}, \quad (2.10)$$

for the case of inhomogeneities with zero stiffness. Here, the quantity ξ_p denotes the volume fraction of the considered population p , ξ is the total volume fraction of all inhomogeneities introduced, and $\mathbf{S}^{(p)}$ is Eshelby tensor associated to population

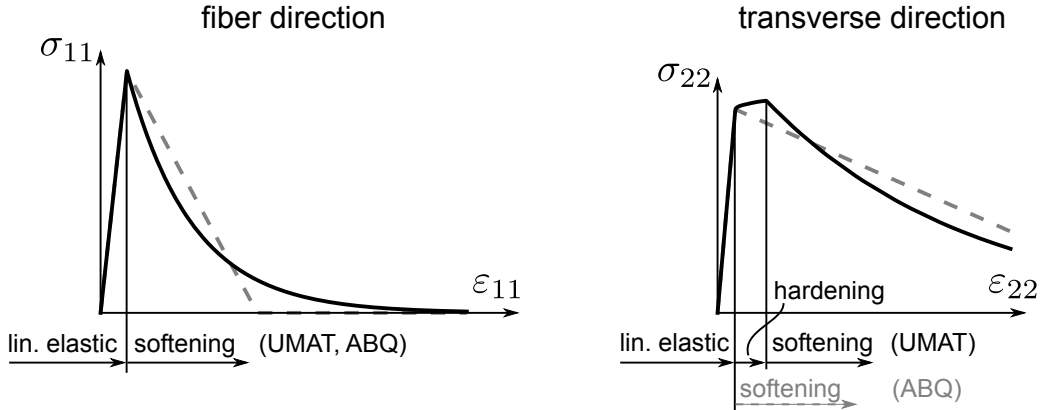


Figure 2.13: Juxtaposition of the nonlinear stress-strain response of the *EPD-model* (solid line) and the *ED-model* (dashed line) using identical material properties with respect to tensile loading in fiber (left) and transverse direction (right).

p. After reaching a specific damage state, exponential strain softening is initiated. The damage evolution in the softening regime is controlled by equivalent strains and formulated based on fracture energies. For the equivalent stresses and strains the relation

$$\hat{\sigma} = \hat{\sigma}_c \exp[-k_l(\hat{\epsilon} - \hat{\epsilon}_c)] \quad (2.11)$$

is required to hold. Here, $\hat{\sigma}_c$ and $\hat{\epsilon}_c$ refer to the equivalent stresses and equivalent strains, respectively, which are predicted at softening onset and k_l is the damage evolution variable, see [38]. Similar to the *ED-model* introduced before a characteristic length is used to alleviate the mesh dependency. To improve the convergence behavior of the numerical computation a viscous regularization scheme is implemented. Besides these damage capabilities the constitutive law allows for unrecoverable strain accumulation, described by two plasticity mechanisms. For a detailed description of this material law the reader is referred to [38–41]. Both introduced material models are designed for plane stress conditions only. However, the *EPD-model* can be used with three dimensional continuum elements bearing the limitation that only the in-plane components of the stress and strain tensor are taken into account when evaluating the damage evolution. Figure 2.13 juxtaposes the two introduced material models for tension in and transverse to the fiber direction.

2.2.4 Interface damage models

To model the inter-laminar damage of laminated composites various approaches are possible. There are the “smeared” approaches, i.e. including the interfacial damage into the adjacent material [74], interface damage model approaches such as cohesive zone elements [2], and there are fracture mechanics based approaches such as the virtual crack closure technique [79]. However, the simulation of delamination based on fracture mechanics methods is tricky, due to the requirement of pre existing cracks. The judgment of the spatial distribution and size of these initial flaws is not straight forward and the modeling can be problematic as well. A common way to deal with debonding and delaminations within the framework of the FEM is to apply interface damage models like cohesive zones, which are readily available in most commercial FEM packages. Nevertheless, several research groups work on enhanced cohesive zone models, e.g. [61, 113]. In [30] cohesive zone elements to be used with shell elements have been proposed which account for the shell kinematics implicitly, and allow for direct coupling of shell structures. Despite their advantages, the application of cohesive zone elements to model delamination in laminated structures comprising multiple plies may be cumbersome since each ply and also each interface has to be modeled individually. Furthermore, it has shown that the size of the cohesive elements has to be small to predict accurate responses [132].

When looking at the cohesive formulations available within Abaqus a further model may be notable, i.e. the surface based cohesive behavior. This formulation, implemented in the contact framework, allows for efficient interface modeling since no additional elements have to be defined. Both cohesive formulations, i.e. element as well as contact based, assume a linear elastic traction separation relation prior to damage onset. Multiple damage initiation criteria are available based on stresses or separations, e.g. maximum stress, quadratic stress, etc. [64]. The damage evolution can be specified to be linear, exponential, or user-defined and can be based on fracture energies or displacements. Furthermore, various mode-mix criteria are available which is especially important for interface delamination between materials with dissimilar properties. Considering a carbon-epoxy laminate it has been shown that the available Benzeggagh-Kenane (BK) mode-mix criterion yields more accurate results than the widely used power law criterion [13]. To improve the convergence behavior with implicit simulations a viscous regularization scheme is available as well.

Chapter 3

Shell element based modeling of textile composites

The proposed modeling strategy is based on the discretization of the fabric unit cell geometry entirely by shell elements. These structural elements condense the three dimensional nature of the constituents into a surface representation. This leads to a substantial decrease of the number of DOFs, enabling computationally less costly simulations which becomes particularly important when treating nonlinearities. The application of shell elements is reasonable since it is a common practice to assume fairly low thickness-to-width ratios of the tows when modeling weaves and biaxial braids, see e.g. [86]. Of course, other textiles types with high thickness-to-width ratios, like e.g. knits, cannot be treated by the present approach. A major point within the present modeling approach is to start with an orthogonal, i.e. weave-like, braid. Due to this assumption the cross sections can be modeled as being uniform along the ondulation paths. Typical geometrical idealizations like perfect periodic weaving patterns, and generic cross sectional shapes (lenticular, rectangular) are applied. The non-uniform cross sections, characteristic for braids with braiding angles different than 45° , are achieved by a subsequent, virtual shearing of the textile, cf. [57].

In the perspective of numerical material characterization the modeling approach is tightly related to the applied homogenization approach. For this reason some general remarks on unit cell considerations are discussed first.

3.1 Unit cell based homogenization

A common approach found in the literature to compute the effective material properties of heterogeneous materials is to apply homogenization. The current work is based on a first order numerical homogenization technique and applying the separation of length scales concept [11]. This requires that the considered individual length scales are sufficiently different in size. Moreover, in case of first order homogenization theory it is assumed that the effective stress and strain fields at the lower length scale can be considered as being gradient free. The latter requirements are only fulfilled to a certain extent when dealing with textiles due to the size of the unit cell with respect to the structural size. Hence, it is important to keep these assumptions in mind when applying the computed effective properties to a larger scale. The restrictions may be eased if a higher order homogenization scheme is applied, see e.g. Kouznetsova et al. [78]. Moreover, additional means are necessary if strain localization is to be included in the simulations [20].

Implicitly, when dealing with textile composites a periodic mesostructure is assumed which can be characterized by the periodic arrangement of the constituents making up the macroscopic heterogeneous material. A possible solution strategy to this type of boundary value problems involves the definition of a repetitive volume element, i.e. a unit cell (UC), to describe the periodic medium. Based on this small subset (UC) the response of the whole medium can be predicted. One may distinguish between one, two, or three dimensional periodicity, characterized by using so called periodicity vectors $\underline{\mathbf{p}}$, cf. [4]. The dimension of the respective unit cells is always greater or equal the dimension of the underlying periodicity. Such a periodic UC permits for any shift vector $\underline{\mathbf{t}} = i\underline{\mathbf{p}}_A + j\underline{\mathbf{p}}_B + k\underline{\mathbf{p}}_C$ with $\{i, j, k\} \in \mathbb{Z}$ and A, B, C being the direction indices of the periodicity vectors, that any spatial varying field quantity (geometrical, mechanical, etc.) P at any location $\underline{\mathbf{x}} \in \text{UC}$ fulfills

$$P(\underline{\mathbf{x}}) = P(\underline{\mathbf{x}} + \underline{\mathbf{t}}). \quad (3.1)$$

Of course, this includes stresses and strains as well, hence all investigations can be conducted on the domain of the UC without loss of information. This implies continuous stresses and compatible deformations at corresponding borders throughout the whole loading history. Compatible deformations ensure that no separation or

overlapping occur and respective displacement fields are often called strain-periodic [103]. In this context the periodicity vectors follow the macroscopic deformation of the unit cell.

For the present problems, i.e. textiles, a two dimensional or plane periodicity is assumed. The corresponding UC is set up in the three dimensional space as will be discussed later.

3.1.1 Choice of unit cell boundaries

Each periodic micro-structure can be represented by means of various different UCs. For the present case of two dimensional braided textiles featuring 2/2 Twill characteristics some possible UCs (not exhaustive) are given in Fig. 3.1. It can be clearly seen that the size of the UC significantly depends on the chosen boundaries. However, more complex boundaries typically dictate more complex coupling relations between the nodes at the UC boundaries. A UC with borders aligned with the tow directions (a), is commonly larger as such with optimized periodicity vectors (b). As with general structures, symmetry boundary conditions may be applicable to further decrease the size of UCs (c). The white arrow and the dashed line indicates the symmetry direction and rotational symmetry axis, respectively. However, symmetry conditions require symmetry loading as well, hence, not all loading conditions are permitted, cf. [11].

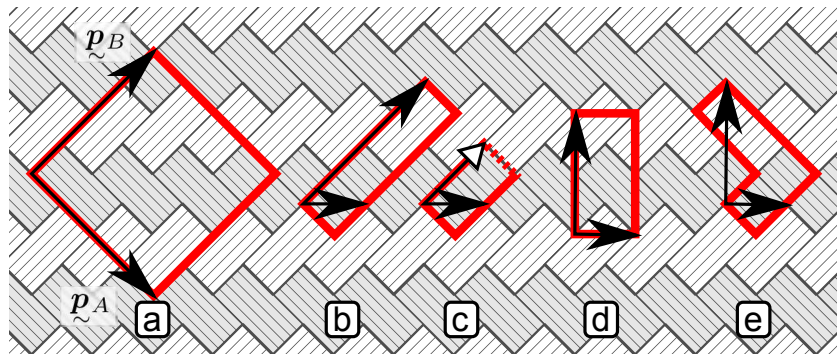


Figure 3.1: Some possible unit cells to capture the periodic microstructure of a 2/2 Twill type textile with the periodicity vectors displayed; (a) classical approach, (b) offset reduced UC [60], (c) offset, symmetry reduced UC [32], (d) braid orientated UC, cf. [106], (e) further possible UC.

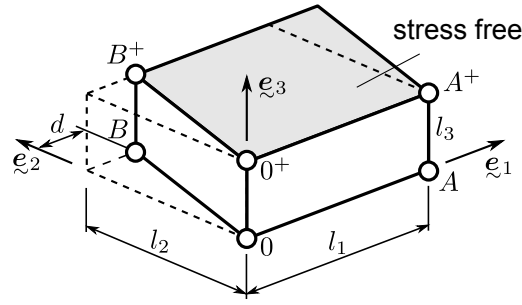


Figure 3.2: Unit cell definition for a plane periodic media with non-orthogonal periodicity vectors including master nodes [103].

In the present study a UC aligned with the tow directions is used, due to its general and simple representation. Nevertheless, it may be noted that the proposed approach is not limited to this type of UCs and other representations may be used as well. Of course, the required boundary conditions have to be adapted accordingly.

3.1.2 The master node concept

The UC as being part of an infinite plane periodic medium is subjected to effective, far field loads. Following the assumptions of first order homogenization theory these far field loads have to be gradient free. With respect to a structural point of view, a layer of fabric is assumed to behave like a thin shell. This implies that the macroscopic loading has to fulfil the plane stress assumptions. Of course, local stresses are not obliged to this constraint. The mean deformation of the UC with respect to the macroscopic stresses and strains, respectively, can be described using some particular characteristic nodes, the so called master nodes [11]. The latter are commonly located at the corners of the unit cell perimeter, see circles in Fig. 3.2. In this figure, l_1 , l_2 , and l_3 are the unit cell's dimensions in x , y , and z direction, respectively, and 0 , 0^+ , A , A^+ , B as well as B^+ are the master nodes. In the present case the “shear shift” d characterizes the no-orthogonality of the periodic medium. If the periodic boundary conditions are implemented in a way to be driven by these master nodes, they can be used to apply given macroscopic stresses or strains by means of appropriate master node forces and displacements, respectively, only. Moreover, using inverse relations it is also possible to derive the effective stresses and strains, respectively, with respect to some applied macroscopic loading using the master node forces and

displacements only. Using this approach the whole macroscopic loading and the respective effective response determination can be handled by means of these master nodes alone. Six master nodes are required to introduce the macroscopic loading scenarios in-plane tension and compression, in-plane shear, bending, and twisting. In this context, macroscopic rotations and moments are realized via a pair of master node displacements or forces.

The thin shell formulation together with the first order homogenization enforce the transverse shear deformation to be zero. Albeit a thick shell assumption would be applied a constant transverse shear stress would require a gradient in the bending moment which conflicts with the assumption of constant macroscopic loading throughout the whole unit cell, see e.g. [11]. To cope with such a situation, the introduction of appropriate volume forces would be required, cf. [125].

3.1.3 Plane periodic boundary conditions

The considered textile composite is treated as a thin, plane periodic structure. As the UC represent only a small subset of an infinite space, the surrounding medium has to be accurately replaced by boundary conditions. In the present case these are commonly called plane periodic boundary conditions implying a plane stress assumption in thickness direction. The boundary conditions link the nodes along the unit cell lateral sides with the appropriate opposite nodes and ensure the periodicity of the displacement fields, i.e. make the two sides fit exactly together without any separation or overlapping. This holds true for the undeformed as well as deformed states. As structural finite elements are used, the boundary conditions include the nodal translations as well as the rotations. The equations derived in the following are based on the assumptions of first order homogenization.

For each point $\underline{\boldsymbol{x}}$, with $\underline{\boldsymbol{x}} \in \mathbb{R}^2$, the displacement in a strain-periodic field can be expressed as (see e.g. Anthoine [4])

$$\underline{\boldsymbol{u}}(\underline{\boldsymbol{x}}) = \boldsymbol{\mathcal{E}} \cdot \underline{\boldsymbol{x}} - \boldsymbol{\chi} \cdot \underline{\boldsymbol{x}} x_3 + \underline{\boldsymbol{u}}^p(\underline{\boldsymbol{x}}) , \quad (3.2)$$

$$u_3 = \frac{1}{2} \boldsymbol{\chi} \underline{\boldsymbol{x}} \cdot \underline{\boldsymbol{x}} + u_3^p(\underline{\boldsymbol{x}}) , \quad (3.3)$$

with $\boldsymbol{\mathcal{E}}$ is the mean strain tensor, $\boldsymbol{\chi}$ is the mean curvature tensor and u_i^p is a periodic displacement field which fulfills Eq. (3.1).

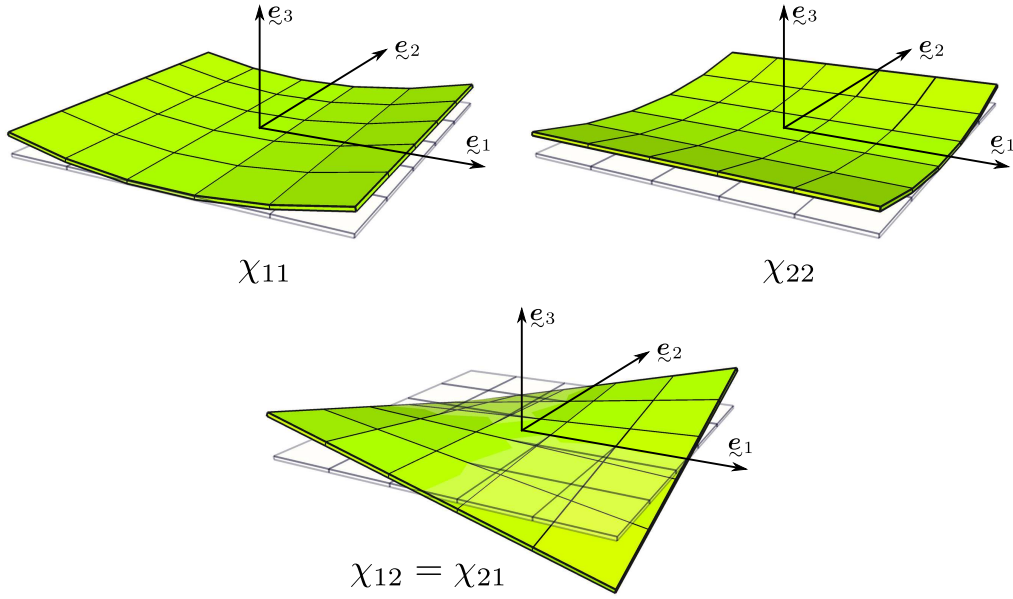


Figure 3.3: Visualization of the individual macro curvature components χ_{ii} applied to a simple quadratic plate, with shifted origin.

The mean curvature tensor accounts for macroscopic bending and twisting. Its components are visualized in Fig. 3.3. Based on these equations the relation between the master node displacements and the mean strain and curvature tensors can be derived following Pahr and Rammerstorfer [103] as

$$\underline{\underline{U}} = \underline{\underline{\boldsymbol{\varepsilon}}} \cdot \underline{\underline{P}}, \quad \text{and} \quad \underline{\underline{R}} = \underline{\underline{\boldsymbol{\chi}}} \cdot \underline{\underline{P}}. \quad (3.4)$$

Here, the so called generalized master node displacement tensor and generalized rotation tensor, defined as

$$\underline{\underline{U}} = \begin{pmatrix} U_1 & V_1 \\ U_2 & V_2 \end{pmatrix}, \quad \text{and} \quad \underline{\underline{R}} = \begin{pmatrix} -R_2 & -S_2 \\ R_1 & S_1 \end{pmatrix}, \quad (3.5)$$

are used to simplify the respective equations. $\underline{\underline{P}} = (\underline{\underline{p}}_A, \underline{\underline{p}}_B, \underline{\underline{p}}_C)$ denotes the generalized periodicity tensor as defined in [102]. The generalized displacements are related to the master node displacements as proposed by Pahr and Rammerstorfer [103] as

$$U_1 = \frac{1}{2} ((u_1^{A+} + u_1^A) - (u_1^{0+} + u_1^0)), \quad (3.6)$$

$$U_2 = \frac{1}{2} ((u_2^{A+} + u_2^A) - (u_2^{0+} + u_2^0)) , \quad (3.7)$$

$$U_3 = \frac{1}{2} ((u_3^{A+} + u_3^A) - (u_3^{0+} + u_3^0)) + \left(R_1 - R_2 \frac{d}{l_2} \right) \frac{l_2}{2} , \quad (3.8)$$

$$V_1 = \frac{1}{2} ((u_1^{B+} + u_1^B) - (u_1^{0+} + u_1^0)) , \quad (3.9)$$

$$V_2 = \frac{1}{2} ((u_2^{B+} + u_2^B) - (u_2^{0+} + u_2^0)) , \quad (3.10)$$

$$V_3 = \frac{1}{2} ((u_3^{B+} + u_3^B) - (u_3^{0+} + u_3^0)) + S_2 \frac{l_1}{2} , \quad (3.11)$$

with the generalized rotations R and S are expressed as

$$R_1 = -\frac{1}{l_3} ((u_2^{A+} - u_2^A) - (u_2^{0+} - u_2^0)) , \quad (3.12)$$

$$R_2 = \frac{1}{l_3} ((u_1^{A+} - u_1^A) - (u_1^{0+} - u_1^0)) , \quad (3.13)$$

$$R_3 = \frac{1}{l_3} ((u_3^{A+} - u_3^A) - (u_3^{0+} - u_3^0)) = 0 , \quad (3.14)$$

$$S_1 = -\frac{1}{l_3} ((u_2^{B+} - u_2^B) - (u_2^{0+} - u_2^0)) , \quad (3.15)$$

$$S_2 = \frac{1}{l_3} ((u_1^{B+} - u_1^B) - (u_1^{0+} - u_1^0)) , \quad (3.16)$$

$$S_3 = \frac{1}{l_3} ((u_3^{B+} - u_3^B) - (u_3^{0+} - u_3^0)) = 0 , \quad (3.17)$$

$$T = -\frac{1}{l_1 l_3} ((u_2^{A+} - u_2^A) - (u_2^{0+} - u_2^0)) . \quad (3.18)$$

With these the relation between the displacements of two corresponding points D and D' with $\underline{\boldsymbol{x}}^{D'} = \underline{\boldsymbol{x}}^D + \underline{\boldsymbol{t}}$ can be expressed as

$$\begin{aligned} \underline{\boldsymbol{u}}^{D'} - \underline{\boldsymbol{u}}^D &= \underline{\boldsymbol{\mathcal{E}}} \cdot \underline{\boldsymbol{t}} - \underline{\boldsymbol{\chi}} \cdot \underline{\boldsymbol{t}} \cdot x_3^D \\ &= \underline{\boldsymbol{U}} \underline{\boldsymbol{P}}^{-1} \cdot \underline{\boldsymbol{t}} - \underline{\boldsymbol{R}} \underline{\boldsymbol{P}}^{-1} \cdot \underline{\boldsymbol{t}} \cdot x_3^D . \end{aligned} \quad (3.19)$$

Nodal rotations. As the aspired element types are shell elements, i.e. structural elements, additional equations have to be added to deal with the nodal rotations. In the style of Eq. (3.2), for every point $\underline{\boldsymbol{x}}$, with $\underline{\boldsymbol{x}} \in \mathbb{R}^2$ the vector of in-plane nodal rotation angles $\underline{\boldsymbol{\varphi}}$ can be expressed as

$$\underline{\boldsymbol{\varphi}} = \underline{\tilde{\boldsymbol{\chi}}} \cdot \underline{\boldsymbol{x}} + \underline{\boldsymbol{\varphi}}^p . \quad (3.20)$$

In this context $\tilde{\chi}_{\approx}$ is a slightly modified version of the mean curvature tensor χ defined as

$$\tilde{\chi}_{\approx} = \begin{pmatrix} \chi_{21} & \chi_{22} \\ -\chi_{12} & -\chi_{11} \end{pmatrix}, \quad (3.21)$$

and φ^p is a periodic nodal rotation field.

For two corresponding points D and D' , with $\mathbf{x}^{D'} = \mathbf{x}^D + \mathbf{t}$ the nodal rotation angles can be expressed as

$$\begin{aligned} \varphi^D &= \varphi(\mathbf{x}^D) &= \tilde{\chi}_{\approx} \cdot \mathbf{x}^D + \varphi^p(\mathbf{x}^D), \\ \varphi^{D'} &= \varphi(\mathbf{x}^D + \mathbf{t}) &= \tilde{\chi}_{\approx} \cdot (\mathbf{x}^D + \mathbf{t}) + \varphi^p(\mathbf{x}^D + \mathbf{t}). \end{aligned}$$

Using Eq. (3.1) these equations can be combined resulting in the relation

$$\varphi(\mathbf{x}^D + \mathbf{t}) - \varphi(\mathbf{x}^D) = \tilde{\chi}_{\approx} \cdot \mathbf{t}, \quad (3.22)$$

which links the rotation of two corresponding points using the modified mean curvature tensor. Using the generalized rotations this can be further expressed as

$$\varphi(\mathbf{x}^D + \mathbf{t}) - \varphi(\mathbf{x}^D) = \begin{cases} \begin{pmatrix} R_1 & R_2 \end{pmatrix}^T, & \text{if } \mathbf{t} = \mathbf{p}_A \\ \begin{pmatrix} S_1 & S_2 \end{pmatrix}^T, & \text{if } \mathbf{t} = \mathbf{p}_B \end{cases} \quad (3.23)$$

The local out-of-plane rotations are not affected by the plane curvature tensor, thus, the respective relation reads

$$\varphi_3(\mathbf{x}^D + \mathbf{t}) - \varphi_3(\mathbf{x}^D) = 0. \quad (3.24)$$

The necessary MPCs and master nodes definitions are implemented in the boundary condition generator provided by the in-house software `medtool 3.7` (*developed by D. H. Pahr, Institut of Lightweight Design and Structural Biomechanics, Vienna University of Technology*).

3.1.4 Homogenized stresses and strains

The periodic boundary conditions use the master nodes to link corresponding nodes of the unit cell sides. Moreover, they can be used to impose a given deformation to the UC using Eq. (3.4). As indicated in Sec. 3.1.2 the master node displacements and forces can also be used to read out the effective behavior of the UC. Following Pahr and Rammerstorfer [103] the master node forces can be related to the homogenized stress resultants as

$$\underline{\underline{\mathbf{N}}} = \frac{1}{2l_1l_2} \left(\underline{\underline{\mathbf{F}}} \cdot \underline{\underline{\mathbf{P}}}^T + \underline{\underline{\mathbf{P}}} \cdot \underline{\underline{\mathbf{F}}}^T \right), \quad (3.25)$$

and to the homogenized resultant moments as

$$\underline{\underline{\mathbf{M}}} = \frac{l_3}{2l_1l_2} \left(\Delta \underline{\underline{\mathbf{F}}} \cdot \underline{\underline{\mathbf{P}}}^T + \underline{\underline{\mathbf{P}}} \cdot \Delta \underline{\underline{\mathbf{F}}}^T \right). \quad (3.26)$$

Where, $\underline{\underline{\mathbf{F}}}$ is the generalized master node force tensor defined as

$$\underline{\underline{\mathbf{F}}} = \begin{pmatrix} F_1^{A+} + F_1^A & F_1^{B+} + F_1^B \\ F_2^{A+} + F_2^A & F_2^{B+} + F_2^B \end{pmatrix}, \quad (3.27)$$

and $\Delta \underline{\underline{\mathbf{F}}}$ reads

$$\Delta \underline{\underline{\mathbf{F}}} = \frac{1}{2} \begin{pmatrix} F_1^{A+} - F_1^A & F_1^{B+} - F_1^B \\ F_2^{A+} - F_2^A & F_2^{B+} - F_2^B \end{pmatrix}. \quad (3.28)$$

With these equations the homogenized stress resultants can be obtained using the master node forces only. In a similar fashion the homogenized strains and curvatures can be derived using the inverse of Eq. (3.4) which leads to

$$\underline{\underline{\boldsymbol{\varepsilon}}} = \frac{1}{2} \left(\underline{\underline{\mathbf{U}}} \cdot \underline{\underline{\mathbf{P}}}^{-1} + (\underline{\underline{\mathbf{P}}}^{-1})^T \cdot \underline{\underline{\mathbf{U}}}^T \right), \quad (3.29)$$

and

$$\underline{\underline{\boldsymbol{\chi}}} = \frac{1}{2} \left(\underline{\underline{\mathbf{R}}} \cdot \underline{\underline{\mathbf{P}}}^{-1} + (\underline{\underline{\mathbf{P}}}^{-1})^T \cdot \underline{\underline{\mathbf{R}}}^T \right). \quad (3.30)$$

Using the inverse relation of Eq. (3.25) and Eq. (3.26), respectively, the master nodes can be used to apply macroscopic loads in a force controlled way. For details the reader is referred to [103]. All these equations are implemented in python scripts to enable automated pre- and post-processing of the textile unit cells.

For the special case of pure membrane states, the stress resultants can also be expressed as homogenized stresses assuming equal values through the whole thickness. For simplicity reasons, respective effective, homogenized stress and strain components, respectively, are addressed as σ_{ij} and ε_{ij} for the rest of this thesis.

3.2 Material based assumptions

The two mesoscopic constituents of the braid, i.e. tows and unreinforced matrix pockets, are to be represented not only in a geometrical sense but also by means of appropriate material models. Focusing on the elastic symmetries, the tows can be treated like classical UD plies, i.e. featuring transversely isotropic symmetry, cf. [23]. This assumptions allow to apply available UD data and material models originally developed for UD composites in the framework of textile composites, cf. Sec. 2.2. In this context, constitutive models featuring intra-ply damage modes and plasticity are addressed. Of course, the local material orientation has to follow the tow path undulation to accurately match the proposed symmetry.

The unreinforced matrix pockets are areas of “pure” resin material. Typical polymeric matrix materials exhibit isotropic behavior in elastic range and are commonly modeled using an elastic-plastic constitutive law [33, 77]. As most polymers show a pressure dependent yield behavior, a Drucker-Prager type plasticity model is a typical choice [33, 56]. Additional measures can be included to take care of large hydrostatic pressures, e.g. capping of the yield surface, cf. [64].

The aspired modeling approach features shell elements only, thus, a plane stress representation is sufficient for both constituents. This, of course, simplifies the models significantly, but neglects possible out-of-plane effects. As long as only thin plies, i.e. tows with a large width to thickness ratio and a small crimp, are considered, this assumption remains reasonable. In case of thick and highly crimped textiles a three dimensional approach based on continuum elements is to be preferred against the proposed shell element based one. With respect to the matrix pockets material, a plane stress assumptions simplifies the model substantially, as no hydrostatic pressure can be applied. Nevertheless, a Drucker-Prager type plasticity model may be used to take care of the different response in tension and compression.

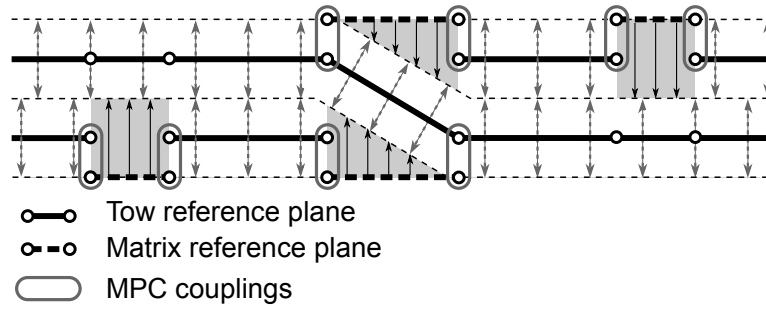


Figure 3.4: Cross section of a simplified 2/2 Twill Weave with rectangular cross sections indicating the shell reference planes, shell offset, and shell thicknesses. Matrix pockets are shaded, circles represent feature edges (not nodes) and the additional MPC couplings are indicated.

3.3 Rectangular tow cross sections

To set-up a unit cell the individual constituents have to be represented appropriately. As numerical efficiency is a main concern, the present approach uses shell elements only. In the following, the corresponding elements will be addressed as tow and matrix shells, respectively. Due to the manufacturing process, the tows are interwoven and the cross sectional shape is formed according to the tow undulation paths. The present strategy idealizes the architecture such that the tow cross section and the undulation path match perfectly. The individual tows, i.e. the resin impregnated bundles of fibers, are treated as UD laminae represented by shell elements. Their reference planes are defined as the mid-surfaces of the tows, as sketched in Fig. 3.4 (thick solid line). Due to the assumption of a rectangular cross section the shell thickness is modeled as being constant along the whole tow. In Fig. 3.4 the dotted arrows visualize the shell thickness and the corresponding thickness direction. The modeling of the complementary geometry of the unreinforced matrix (shaded areas in Fig. 3.4) is not that straightforward. However, a uniform and simple treatment of the complex matrix geometry is attained by placing the shell reference surfaces for the matrix shells at the unit cell top and bottom surfaces as sketched in Fig. 3.4 (thick dashed lines). To fill the matrix pocket areas according to the local geometry, a variable shell thickness is applied. Figure 3.4 shows the required shell thickness variations and directions by solid arrows. For tows with a rectangular cross section, two layers of matrix shells are sufficient, but a more realistic cross section like a lenticular one, requires more layers of matrix shells placed within the unit cell, as will

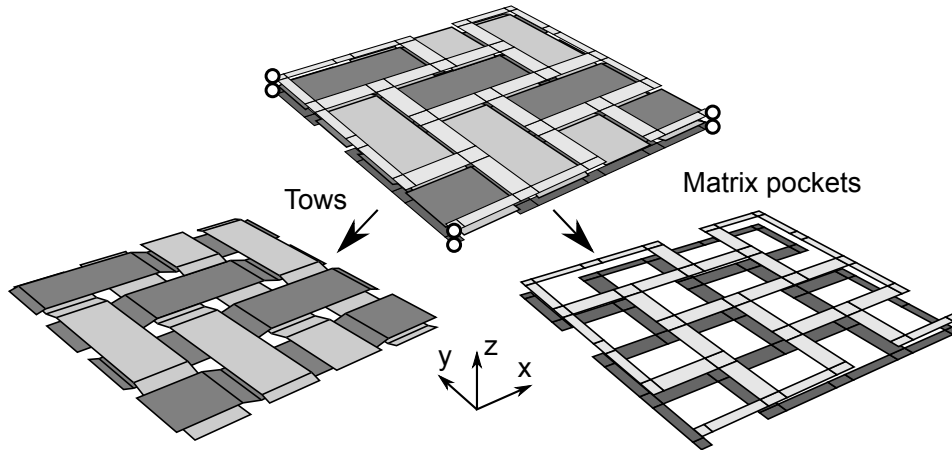


Figure 3.5: Shell element based unit cell assembled (top) and disassembled into tow reference planes (left) and matrix reference planes (right) for the 2/2 Twill Weave unit cell, white circles (top) mark the unit cell master nodes.

be discussed later. A complete unit cell of a simplified 2/2 Twill Weave is shown in Fig. 3.5 in an assembled and disassembled view. The sparse and net-like structure of the matrix pockets is clearly visible.

Since the modeled tow and matrix shells are not connected directly, i.e. they don't share any common nodes, additional links have to be introduced. Within the present approach, two tows are modeled as touching each other at the overlapping areas without any additional layer of matrix in between. At these overlapping areas, the adjacent tow surfaces are coupled appropriately, taking into account the shell thickness as well as the shell element kinematics. Two possible coupling tools are the readily available surface ties and a cohesive coupling based on a contact model in Abaqus. The same type of surface couplings are also used to link the matrix shells to the corresponding matrix and tow shells, respectively. As presented in [44] damageable interfaces may be defined to study “intra-ply” delamination phenomena, i.e. delamination within a ply.

The rectangular cross section necessitates additional couplings to take care of the cross sectional joints not sufficiently captured by the surface couplings. To this end, the edges of the matrix shells are linked to their corresponding tow edges by means of multiple point constraints (MPCs) as indicated by the rounded rectangles in Fig. 3.4. These constraints mimic the underlying shell kinematics and couple the nodal DOFs

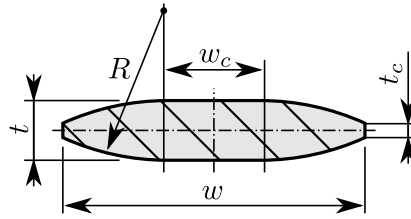


Figure 3.6: Generic lenticular based tow cross section.

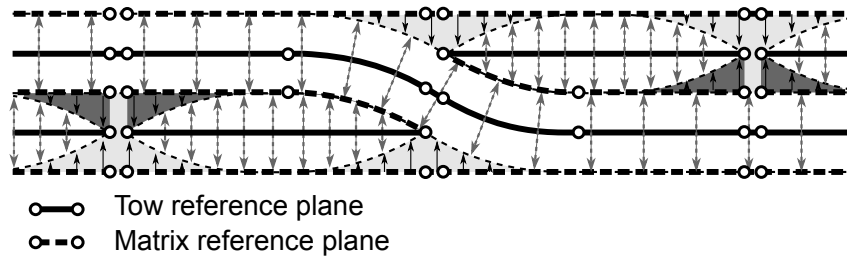


Figure 3.7: Cross section detail of a 2/2 Twill Weave with lenticular cross sections indicating the shell reference planes, shell offset, and shell thicknesses. Matrix pockets are shaded, circles represent feature edges (not nodes) and the dark shaded regions indicate the additional matrix pockets.

based on the shell thickness and nodal rotations and prevent cleavage of the respective constituents.

This modeling approach is implemented as a standalone python 2.6.6 [135] preprocessor script and published in [44].

3.4 Lenticular tow cross sections

The rectangular cross sections applied before are a rather rough representation of real textile tow cross sections. Hence, in the following, the tows will feature a lenticular based cross section as sketched in Fig. 3.6. To set up the single ply unit cell with lenticular tow cross sections following Fig. 3.7 the tows feature a variable thickness along their width. Moreover, the previous approach has to be extended to deal with the additional unreinforced matrix pocket wedges appearing between the tows at the junction points. Similar to before, two layers of matrix shell elements positioned at the unit cell's top and bottom surface are used to model the pure resin areas. Due to the lenticular shape of the tows and the corresponding gradual variation in

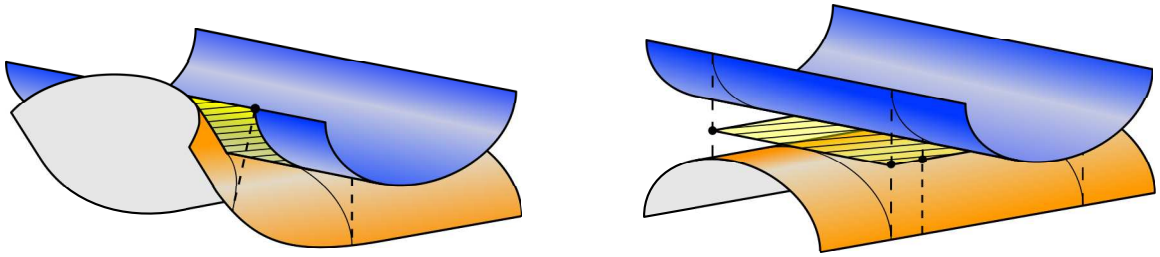


Figure 3.8: Modeling approach of the additional matrix pocket shells to cope with the straight-curved (left) and straight-straight (right) case.

shell thickness the whole top and bottom areas are represented with shell elements, here. Depending on the local, geometrical configuration of the tows at the cross-over points, one can distinguish between three different geometrical cases and respective modeling approaches.

- Ⓐ **curved-curved** Here, both tow paths are locally curved. Based on the assumptions no matrix pockets are modeled in between the tows. Instead, a surface based coupling is directly applied.
- Ⓑ **straight-curved** One tow remains straight whereas the other one is in an undulation state, see Fig. 3.8 (left). The respective intermediate matrix pocket shell reference planes are placed at the inner surface of the straight tow (hatched area). A shell offset and a variable thickness formulation is applied to fill the gap between both tows. Again, surface based couplings are used to connect the tows with the matrix pockets.
- Ⓒ **straight-straight** In this case both tows remain straight, as sketched in Fig. 3.8 (right). The respective reference planes for the matrix pockets are modeled at the center of the UC (hatched area). As Abaqus does not allow to specify a nodal based offset, the shells are doubled assigning a positive offset to one layer and a negative offset to the other. Again, a nodal thickness variation is used. These two super-imposed layers of shells are tied together and both are linked appropriately to the surrounding tows using respective coupling measures.

In the case of a 2/2 Twill topology, each cross-over point feature all of the defined geometrical cases – one at each quadrant, see Fig. 3.9 (left). For clarity, Figure 3.9 (right) shows the respective intermediate matrix pocket shell elements with expanded thickness in an exploded view. In this figure the white hatched area represents the shell reference plane of the lower intermediate shell elements. Similar, the reference

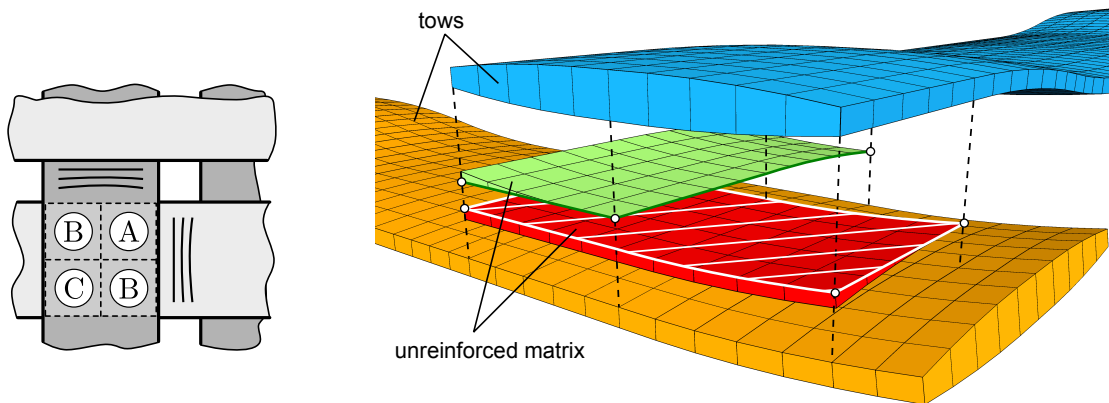


Figure 3.9: Sketch of the geometrical cases in a 2/2 Twill cross-over point (left) and exploded view of the respective shell elements with expanded shell thickness (right). The white hatched area is the reference plane of the lower shell elements, the dots correspond to the feature points in Fig. 3.10.

plane of the upper shell elements is located on the bottom side of these elements. The white dots indicate the feature points as defined in Fig. 3.7. Of course, different braiding patterns result in a different distribution of the geometrical cases.

To represent the local geometry accurately, the shell elements feature a non-uniform shell thickness as clearly visible in Fig. 3.9. Using this modeling approach, all matrix pockets are represented. The individual constituents are again coupled using surface based measures. As these couplings internally introduce a master-slave hierarchy, a bottom-up approach ensures consistent couplings. The additional constraints at the tow edges as required with rectangular cross sections are not necessary here.

Similar to the rectangular cross section modeling strategy an open textile topology is implied, thus, additional measures might be necessary to accurately treat dense textiles.

3.5 Multilayer Composites

As already discussed in Sec. 2.1.4, various approaches are published to deal with multilayer composites. The most common approach of using distinguished out-of-plane boundary conditions can be applied here partially. Representation of out-of-

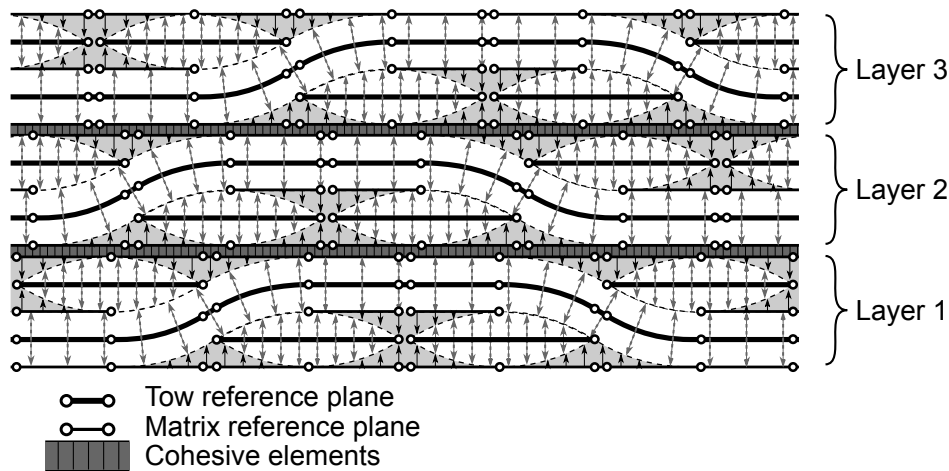


Figure 3.10: Sketch of a cross section of a three layer 2/2 Twill weave laminate with “arbitrary” ply stacking sequence indicating the shell reference planes, shell offset, and shell thicknesses. Matrix pockets are shaded, circles represent feature edges (not nodes). The gap between the layers, i.e. the height of the cohesive elements, is only for visualization purposes.

phase stacking is possible, however, out-of-plane periodicity cannot be enforced due to the internal, hierarchical coupling of the proposed approach. Nevertheless, the fundamental focus on computational efficiency allows to simulate multilayer textiles with explicitly modeled individual layers. The applied unit cell approach requires that all these layers exhibit the same outer in-plane dimensions, i.e. this corresponds to equal or natural multiples of the periodicity vectors. There is no additional restriction on the individual tow geometries and material systems.

The proposed modeling of multiple layers of textile composites follows a hierarchical approach. The desired number of single layer shell element based unit cells are modeled and stacked appropriately without any gap between the layers. Optional interply shifts are to be introduced within the single layer modeling. The coupling between these individual layers are realized by cohesive elements, see Fig. 3.10, which are readily available in most common FEM codes. These elements allow for relative out-of-plane normal and in-plane shear separation of the faces forming the interface. Moreover, the elements break the master-slave sequence of the single layer unit cell tie constraints, which makes the coupling of the individual shell reference planes easier. Finally, the in-plane boundary conditions are applied to the complete stack. This

way the considered unit cell comprises the whole laminate thickness. Currently, no nesting effects are included in the approach.

3.6 Braid angles $\neq \pm 45^\circ$

So far the unit cell can only represent braids featuring a braiding angle of $\pm 45^\circ$. To overcome this limitation a geometrical, i.e. strain-free, skewing of the initially orthogonal unit cell is applied as proposed by Goyal [57]. This approach is feasible as 2D biaxial braids have the same structure as sheared woven fabrics, [85]. To this end, all the nodes are transformed using a pure-shear type skewing and a subsequent rotation, see Fig. 3.11. The total transformation can be expressed as

$$T(\alpha) = T_R(\alpha) \cdot T_S(\alpha) = \begin{pmatrix} \cos \alpha & \sin \alpha & 0 \\ -\sin \alpha & \cos \alpha & 0 \\ 0 & 0 & 1 \end{pmatrix} \begin{pmatrix} 1 & \tan \alpha & 0 \\ \tan \alpha & 1 & 0 \\ 0 & 0 & 1 \end{pmatrix}, \quad (3.31)$$

with $\alpha = 45^\circ - \varphi$, and φ being the braiding angle in degrees. The resulting unit cell exhibits a rhombus shape with one tow direction aligned with the unit cell coordinate \mathbf{e}_1 . This two step procedure, Fig. 3.11, ensures equal geometric conditions for the tows in both directions of the skewed unit cell. However, it changes the unit cell volume $V' = \det(T)V$ and the tow widths ($a \rightarrow a'$). The relation between the un-skewed and skewed tow width can be derived as

$$a = a' \frac{\cos \alpha}{2 \cos^2 \alpha - 1}. \quad (3.32)$$

This geometry change has to be taken into account when setting up the initial unit cell and during post-processing the master node results. As shell elements are used throughout the whole unit cell the local material orientations can be easily adapted by aligning the local fiber direction with the tow orientation. The other two directions are implicitly defined by the shell normal and the Cartesian nature of the material coordinate system.

During this skewing process the cross sectional shape implicitly changes along the tow length, see [57]. Figure 3.12 illustrates this variation of the cross section by

expanding of the shell thickness. This variation ensures compatible interfaces and is, strictly speaking, only exact for a three dimensional representation of the tows. In case of shell elements, the skewing leads to a slight deviation of the shell normals which in-turn result in no longer perfectly matching interfaces. However, within the assumptions of the modeling approach - small thickness-to-width ration and small crimp - this inaccuracy can be neglected.

The proposed modeling approach issues a generic unit cell to model various types of weaves and braids featuring braiding angles from $\pm 25^\circ$ to $\pm 65^\circ$.

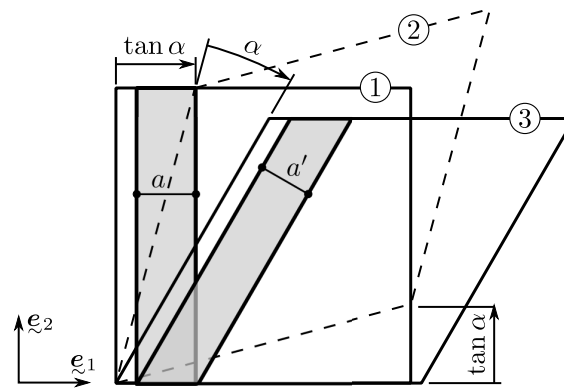


Figure 3.11: Sketch of the skewing and subsequent rotation process with indicated tow width change.

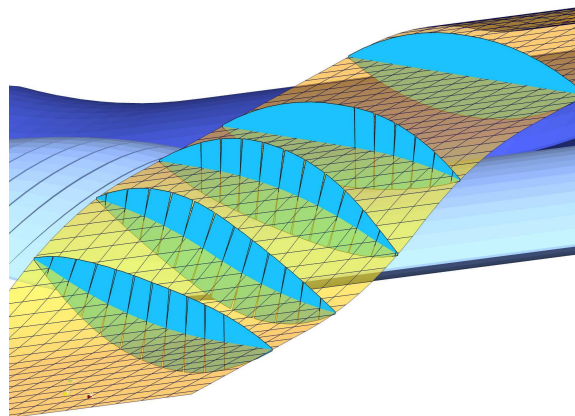


Figure 3.12: Implicit variation of the cross section of a $\pm 30^\circ$ braid model due to the skewing of the unit cell.

Chapter 4

Application to textile composites

This chapter addresses the capabilities of the proposed modeling approach in terms of accuracy, performance. To start with, the rectangular cross section based strategy (Sec. 3.3) is verified by comparison of a respective unit cell with its continuum element based counter part. Subsequently, this unit cell is used to conduct nonlinear simulations taking into account nonlinear constituents behavior.

Starting with Sec. 4.3 the lenticular cross section based strategy is applied for the rest of this chapter. A verification study of the lenticular cross section strategy shows its performance compared with a continuum element based unit cells (Sec. 3.4). Based on this, multilayer textiles are considered and some comments on their elastic and nonlinear behavior are given.

Finally, Regular (2/2 Twill type) braids featuring different braid angles are investigated. In this context, elastic considerations of single and multilayer braids are presented. Moreover, the predicted nonlinear result of three different braids is compared with experimental data. In the following, the rectangular and lenticular cross section based strategy, respectively, will be abbreviated as rectangular and lenticular strategy, respectively.

4.1 Verification of the rectangular cross section model

To check whether the shell element based discretization and the applied assumptions are admissible, the mechanical response of a carbon/epoxy 2/2 Twill Weave single layer unit cell model is compared to the results of a continuum element based reference model of the same weave in terms of global effective stiffness and local stress field predictions. The used UC geometry as well as continuum element based representation is based on the work of Marte [87]. During this section, the shell element based model is denoted as *shell model* and the reference model is called *continuum model*.

First, the effective initial shell stiffness matrices as well as the local stress fields are compared and the simulation time as well as the memory requirements are juxtaposed. In a second step, the response of the shell model with matrix material applied to all constituents is examined as well. This test is denoted as “isotropy test”. Finally, a geometric nonlinear simulation is conducted and the responses of the two models are compared. All simulation rely on linear elastic constituents behavior and the results are published in [44].

4.1.1 Geometry description - Unit cell

The unit cell of the 2/2 Twill Weave is taken as the smallest periodic repeating geometry pattern with orthogonal periodicity vectors and consists of four tows in each direction. The tows are modeled featuring a rectangular cross section and corresponding undulations paths with piece-wise linear segments. A sketch of the cross section and the required dimensions are given in App. B using the ID *Rect-1*. This weave architecture results in a tow volume fraction, i.e. volume of the tows with respect to the unit cell volume, of 74%. With an assumed fiber volume fraction of 70% of the tows, the considered weave exhibits a total fiber volume fraction of 51.8%.

4.1.2 FEM model

To predict the mechanical properties, the unit cell is set up in the framework of the FEM following the modeling strategy presented in Sec. 3.3. The modeled reference planes are meshed by 4-noded shell elements with linear shape functions. The elements used are fully integrated with five section points in the thickness direction applying Simpson rule integration. This integration scheme places a section point onto the shell surface which is suggested if surface results are of interest [64]. Due to the assumed rectangular tow cross section a uniform shell thickness is used for the tows. However, the elements representing the unreinforced matrix pockets, need a local variation of the thickness to represent the wedge-like geometry occurring due to the undulating tows, as shown in Fig. 3.4. All elements feature a typical element edge length of about $1/14^{\text{th}}$ of the tow width. Figure 4.1 (left) shows a detail of the resulting FEM model. The interfaces between the individual tows and between the tows and matrix are modeled by tie constraints implying perfect interfaces.

The tows are modeled as being linear elastic, transversally isotropic, whereas the unreinforced matrix pockets are represented by a linear elastic, isotropic material. The respective material data can be found in App. A Tab. A.1. To represent an infinite shell-like medium, plane periodic boundary conditions are used. Additional constraints on the master nodes prevent rigid body modes to occur.

4.1.3 Reference model

The same unit cell geometry (rectangular cross section, piecewise linear ondulation path) is discretized by continuum elements to serve as a reference model. Quadratic tetrahedral elements are used with a typical element edge length of about $1/18^{\text{th}}$ of the tow width to achieve a reasonable discretization in thickness direction. Figure 4.1 (right) shows a detail of the reference model with displayed element edges in comparison with the shell model (left). This model was originally set up in [87] and the same material data and macroscopic behavior are assumed as defined in the previous section. All interfaces are modeled as perfect, i.e. the opposing element faces forming the interfaces share the same nodes.

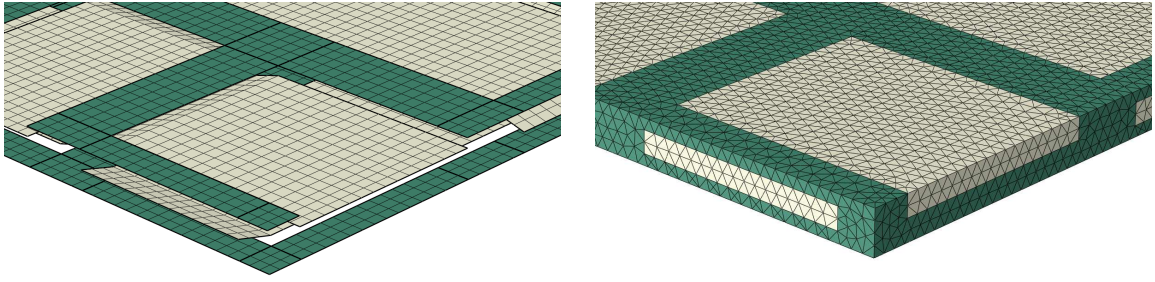


Figure 4.1: Details of the FEM models using shell elements (left) and continuum elements (right).

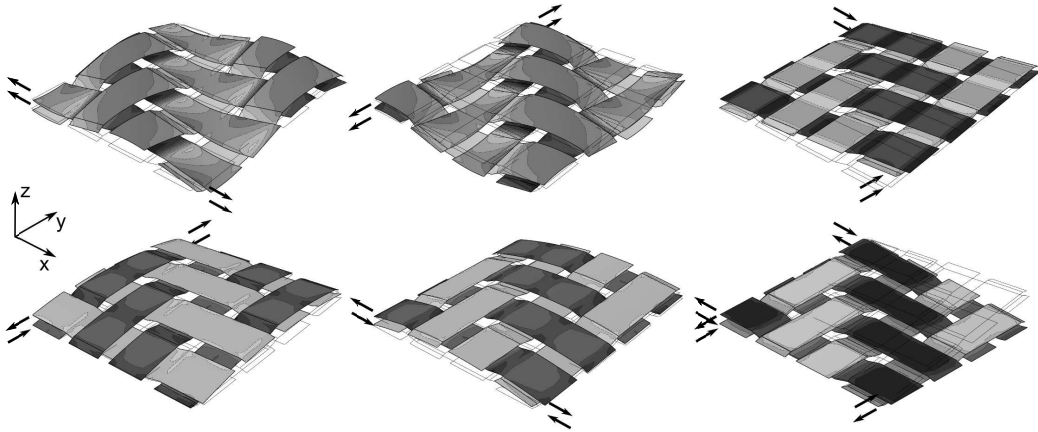


Figure 4.2: Six load cases (top row – uniaxial tension in x and y direction, in-plane shear; bottom row – bending around x and y , twist) with indicated master node forces and the corresponding unit cell deformations, matrix shells are suppressed.

4.1.4 Initial effective shell stiffness

To predict the initial effective shell stiffness matrix, the ABD matrix, six independent load cases are needed. The choice here is two uniaxial tensile load cases, one in-plane shear load case, two bending load cases and one twisting load case, see Fig. 4.2. Due to the shell element based modeling strategy the elastic constants in the out-of-plane direction cannot be predicted. Based on this ABD matrix, the engineering moduli $E_{x'}$ and $G_{x'y'}$ are computed where $x'-y'-z'$ denote a coordinate system, rotated with respect to the global z -axis. In Fig. 4.3 a polar plot of these two predicted moduli of the shell and continuum model shows that both responses are almost identical. The comparison of the bending submatrices, $\underline{\underline{D}}$, a case which is considered being

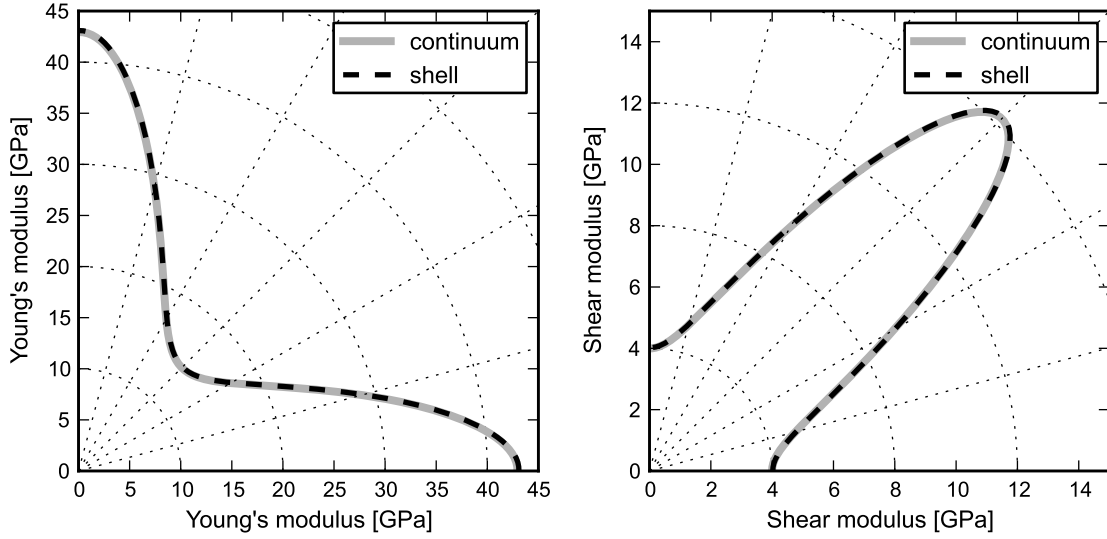


Figure 4.3: Polar plot of the predicted effective Young’s modulus $E_{x'}$ (left) and the predicted effective shear modulus $G_{x'y'}$ (right) of the shell and continuum model.

more “delicate”, reveal that the bending responses agree very well, too. Here, the dominant diagonal terms of both approaches show a deviation below 4%,

$$\underline{\underline{\mathbf{D}}}_{\text{shell}} = \begin{bmatrix} 113.9 & 2.6 & 0.9 \\ 2.6 & 113.9 & 0.9 \\ 0.9 & 0.9 & 14.9 \end{bmatrix}, \quad \underline{\underline{\mathbf{D}}}_{\text{cont}} = \begin{bmatrix} 109.9 & 2.4 & 0.9 \\ 2.4 & 109.9 & 0.9 \\ 0.9 & 0.9 & 14.9 \end{bmatrix}. \quad (4.1)$$

Further, it might be noted that the $\underline{\underline{\mathbf{B}}}$ matrix equals the $\underline{\underline{\mathbf{Q}}}$ matrix with a good accuracy, hence, pure membrane loads do not introduce additional macroscopic bending or twisting of the cell. Since there is no “macro” membrane-bending coupling, effective in-plane stresses can be considered as constant through the thickness. The latter will be used in the following to allow for classical (effective) stress-strain curves to be used.

Despite the fundamentally different modeling approaches applied, a comparison of the local stress fields at the UC top surface of both models shows very good agreement for all six load cases. As an example the stress fields (top side) due to in-plane shear are juxtaposed in Fig. 4.4 applying the same contour level delimiters. Here, the local tow coordinate system 1–2–3, with 1 being the fiber direction and 3 the out-of-

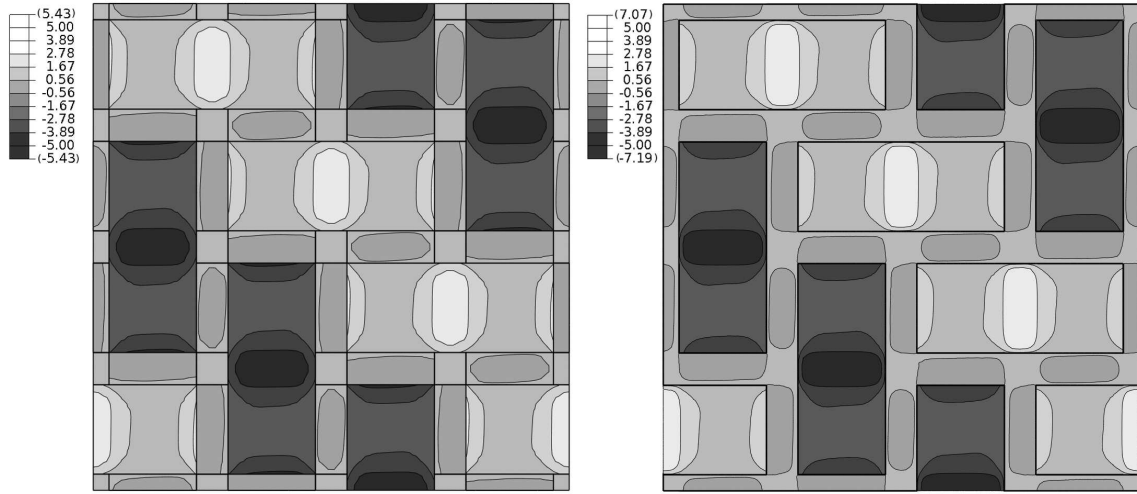


Figure 4.4: Predicted stress at the UC top surface, σ_{12} , due to in-plane shear loading of the shell model (left) and the continuum model (right), contour level delimiters are set equal in both plots.

Table 4.1: Computational requirements for the effective initial shell stiffness computation (left) as well as the geometric nonlinear simulation (right) comparing the shell and continuum model for a standard desktop PC.

	initial stiffness		geom. nonlinear	
	shell	continuum	shell	continuum
DOFs	92,352	1,133,592	92,352	1,133,592
Memory	209 MB	14,385 MB	239 MB	14,204 MB
Time	37 sec	546 sec	55 sec	13,405 sec

plane direction, is used. It can be seen that the predicted stress fields match quite well in a qualitatively and quantitatively view. The difference between the maxima and minima arises for the better part from the dissimilar discretization, i.e. different element types and element sizes. In Tab. 4.1 (left) the number of DOFs, the memory requirement, and the simulation time for the effective shell stiffness computation are given. Although these quantities are highly mesh dependent, a distinct gain in efficiency in terms of computational efforts is clearly visible. The listed simulation times are achieved with a standard desktop PC.

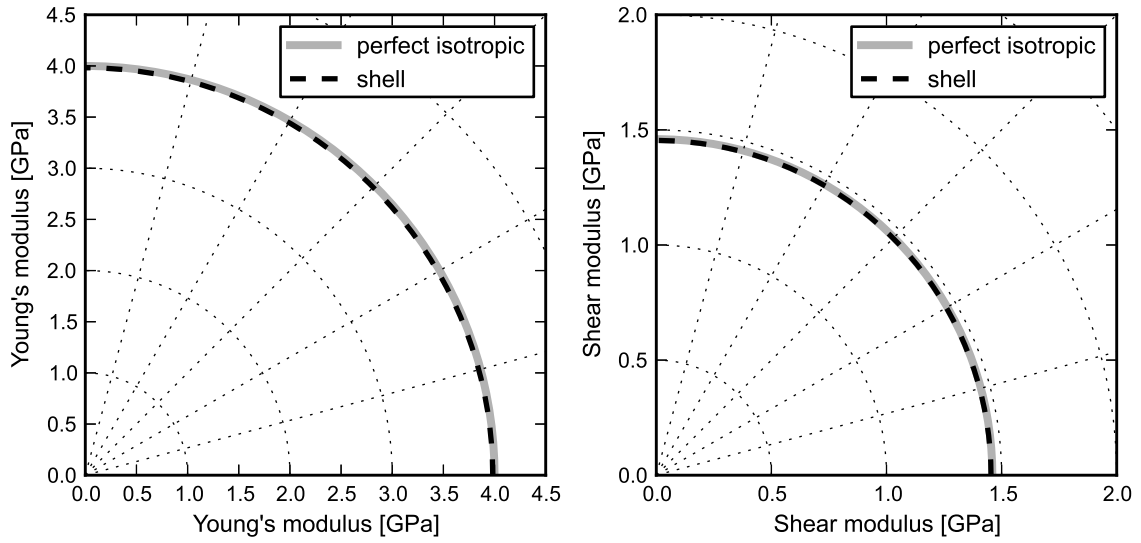


Figure 4.5: Polar plot of the predicted effective Young's modulus $E_{x'}$ (left) and the predicted effective shear modulus $G_{x'y'}$ (right) of the shell model (isotropy test).

At this point, attention might be called to the deformation of the UC with respect to loading in tow direction, see Fig. 4.2 (top left). As this figure shows the UC warps locally with a diagonal wave-like deformation. This deformation is typical for Twill type textiles and leads to some interesting features, as will be discussed later. Moreover, it is a local phenomenon and the UC shows no effective, macroscopic bending or twisting. Uniaxial loading in the 45° direction (braiding direction) does not introduce these local warping patterns.

4.1.5 Isotropy test case

Based on the six load cases, a further essential verification is conducted, i.e. the "isotropy test". To this end, the tow material is replaced by the isotropic resin material, resulting in a block of pure resin material but modeled by the shell approach. The predicted effective response is required to match the matrix properties which is satisfied with a deviation below 0.5%. Moreover, the typical warping deformation, see Fig. 4.2 (top left) does not appear. Considering all the assumptions applied, the result is quite remarkable for the proposed shell model.

4.1.6 Geometric nonlinear simulation under uniaxial tensile loading

In addition to the initial shell stiffness comparisons the geometric nonlinear response of both models subjected to uniaxial tensile stresses in global x -direction is examined. To this end, a displacement controlled load is applied and the number of equal solution increments is fixed to 20. A geometric nonlinear simulation is conducted to capture the effect of the rotation of the tows caused by the stretching of the undulations. Due to this stretching some stiffening is expected. Figure 4.6 shows the effective response of the unit cells plotted as engineering stress against linearized strains. It can be seen, that the predictions, including the stiffening, are in an excellent agreement. To highlight the nonlinearity, the initial stiffness is also plotted (dashed line). It may be noted, that the pronounced nonlinear response is caused by the single layer consideration. Moreover, no ply-failure criteria is used to assess overall strength. The computational efforts listed in Tab. 4.1 (right), reveal the tremendous potential of the shell model compared to the continuum model when conducting geometric nonlinear simulations.

4.2 Nonlinear behavior of a simplified Twill weave

The previous section showed that the shell based unit cell approach accurately predicts linear elastic fabric stiffnesses as compared to a three dimensional discretization of the same simplified Twill Weave model. Furthermore, the benefit in computational resources and time has been highlighted. The following investigation deals with the nonlinear response of the textile fabrics due to material induced nonlinearities. To this end, the same unit cell as defined before (rectangular cross section) is taken but the tows are equipped with the *EPD-model* constitutive law featuring elastic-plastic-damage behavior. The matrix pockets are modeled using a readily available elastic-plastic material model based on the Drucker-Prager formulations. The applied material system is Cycom977/HTS40 defined in App. A Tab. A.3.

Various load cases are examined as indicated in Fig. 4.7. Since a displacement controlled loading offers various benefits like capturing macroscopic softening, the application of a displacement controlled scheme is desired. The first and second load cases

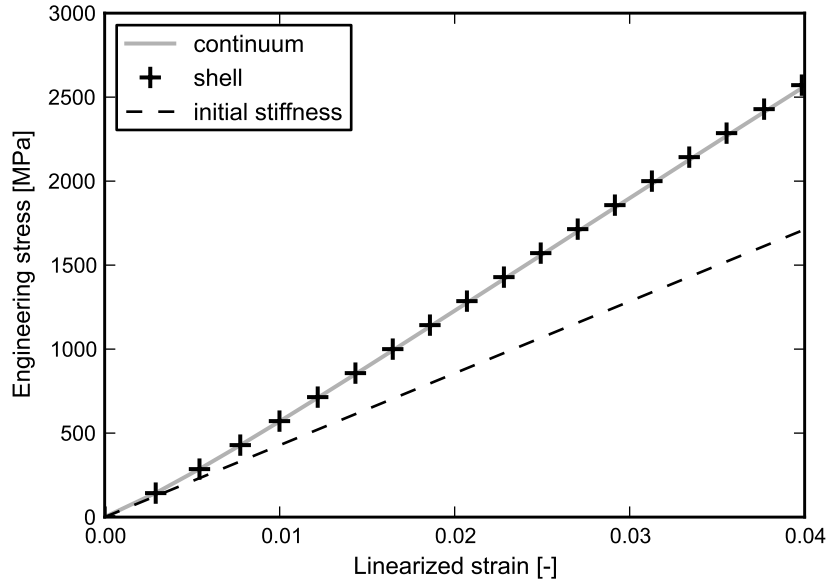


Figure 4.6: Predicted effective response, $\sigma_{xx} - \varepsilon_{xx}$, of the shell and continuum model due to macroscopic uniaxial tensile loading in a geometrical nonlinear simulation. The dashed line represents the initial stiffness (corresponding to the effective in-plane Young's modulus E_x).

investigated are a displacement controlled uniaxial tensile stress along the x -axis and a displacement controlled uniaxial compressive stress along x . Third, a displacement controlled in-plane shear is applied. The fourth load case, features a tensile loading along the 45° diagonal in a force controlled way. All these loading scenarios issue a nonlinear geometry formulation to account for the effects due to the deviation in tow orientations. As the applied tow material model is only formulated for small strains, the results predicted at large strains have to be treated with caution. For the sake of brevity, residual curing strains are not taken into account. However, if required they could be included easily.

Additionally, the intra-ply delamination, i.e. delamination within the ply, is investigated. Here, damageable interfaces are considered and the constituents are represented using linear elastic assumptions alone.

In the following the response of the unit cell is given in terms of engineering stress vs. linearized strain. These measures are derived from the master node forces and displacements. The macroscopic strength is predicted when fiber softening starts to evolve, and the simulation is terminated. The corresponding point in the stress-strain

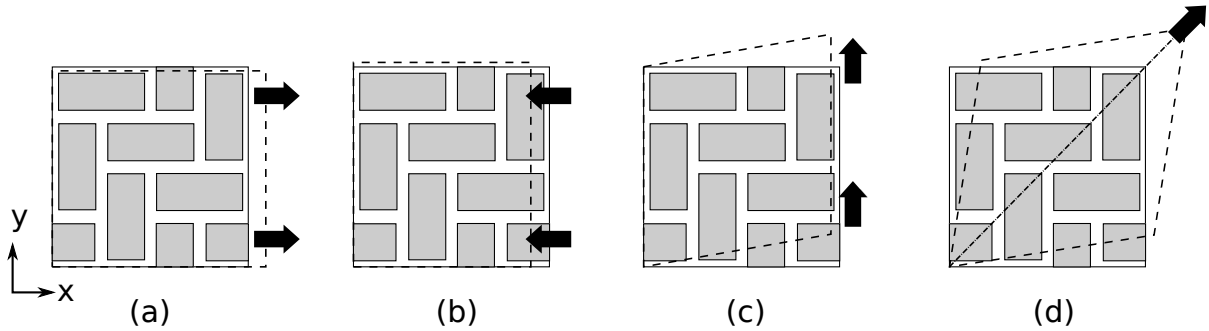


Figure 4.7: Sketch of investigated load cases, (a) uniaxial tension, (b) uniaxial compression, (c) in-plane shear, (d) uniaxial tension along 45° . The dashed shapes indicate the macroscopic, homogenized deformation but not the local periodic unit cell deformations.

plot is marked by a \times . It is noted that macroscopic localization within the periodic unit cell violates the basic principles of homogenization. It has been shown that localization is a structural phenomena, hence, no appropriate “representative volume element” can be found, except for the whole structure [54]. The presented results are published in [43].

4.2.1 Uniaxial tension in x -direction

Figure 4.8 gives the predicted nonlinear response of the unit cell subjected to uniaxial tensile stresses. For this loading scenario the nonlinearity is mainly influenced by the geometrical effect of flattening of the tow undulation which leads to stiffening. In the tows perpendicular to the loading direction some transverse damage occurs, starting at about 50 % of the peak load. This damage causes a reduction of the transverse Young’s modulus in the corresponding tow material but has no detectable effect on the macroscopic response. In the considered loading range hardly any plastic strains occur within the tows. Some plastic strains accumulate in the matrix pockets next to the transversely damaged tows areas. These plastic strains do not alter the global response. The simulation terminates due to emerging local fiber softening in loading direction. Since this fiber softening occurs in all four load bearing tows the corresponding load level is interpreted as the load carrying capacity of the fabric.

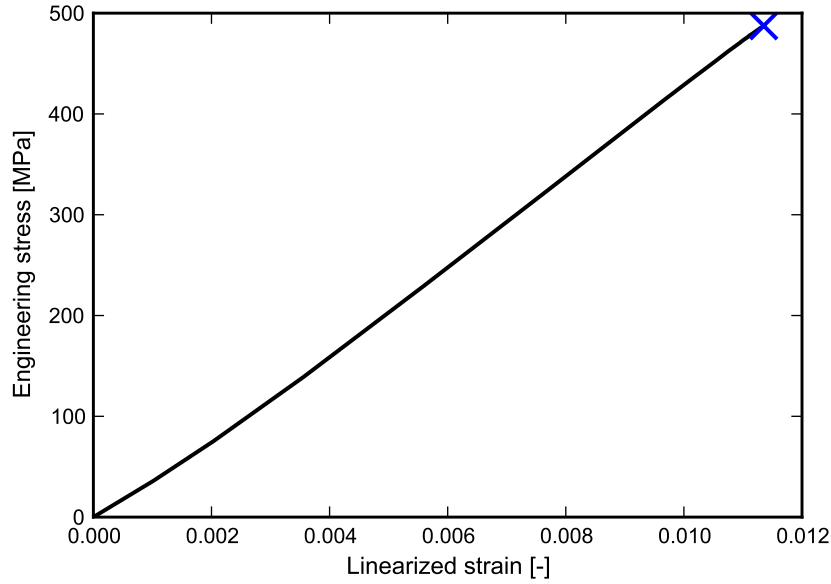


Figure 4.8: Predicted homogenized response of the unit cell due to macroscopic uniaxial tensile engineering stresses, σ_{xx} , vs. linearized strains, ε_{xx} . The cross marks the predicted peak load.

4.2.2 Uniaxial compression in x -direction

The response of the unit cell subjected to macroscopic uniaxial compressive stresses is plotted in Fig. 4.9. The pronounced nonlinearity in this curve arises from the local warping of the textile structure and the employed nonlinear geometry formulation. The unloading cycle, starting at about 1% compressive strain, reveals that some plasticity occurs during the compression. The plastic in-plane transverse and shear strains accumulation starts at a homogenized strain of about 0.4 % within both the tows and the matrix pockets. Furthermore, transverse damage evolves in the tows in loading direction. This damage has only minor influence on the response of the unit cell. The simulation is stopped due to fiber softening in loading direction.

4.2.3 In-plane shear loading

The in-plane shear is realized similar to a simple shear formulation by displacing the master nodes along the y -direction as sketched in Fig. 4.7. In contrast to the original simple shear formulation the displacements along the x -direction remain un-

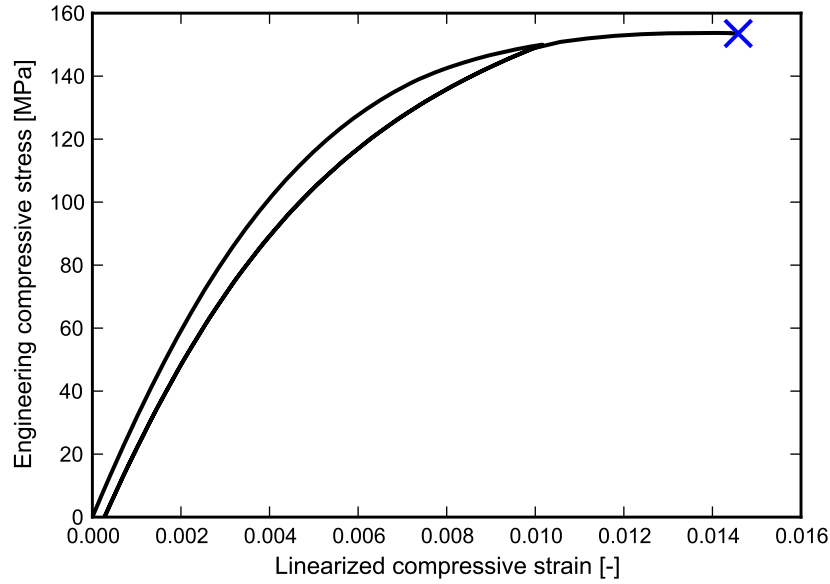


Figure 4.9: Predicted homogenized response of the unit cell due to macroscopic uniaxial compressive engineering stresses, $-\sigma_{xx}$, vs. the linearized compressive strains, $-\varepsilon_{xx}$. The cross marks the predicted peak load.

constrained to prevent additional tensile stresses in the tows at higher strains. During loading the resulting stress state changes from simple shear to a combined loading state. In Fig. 4.10 the response of the unit cell is plotted. Two unloading cycles reveal the dominant nonlinearity, as being caused by plastic strain accumulation in the tows. Damage onset is predicted at a linearized shear angle of about 0.07. Subsequent damage evolution takes place very localized at the undulating parts of both tow directions. Again, emerging fiber softening is considered as the failure load and the simulation is terminated.

4.2.4 In-plane tension along 45°

The employed concept of macroscopic DOFs does not allow to represent a displacement controlled uniaxial stress in an arbitrary loading direction different to the x and y direction. To realize a uniaxial stress along the diagonal of the unit cell, i.e. in the direction 45° relative to the tows, a force controlled approach has to be taken. To this end the displacements of the master nodes are coupled symmetrically with respect to the 45° direction. Additionally, master node forces are applied representing a uni-

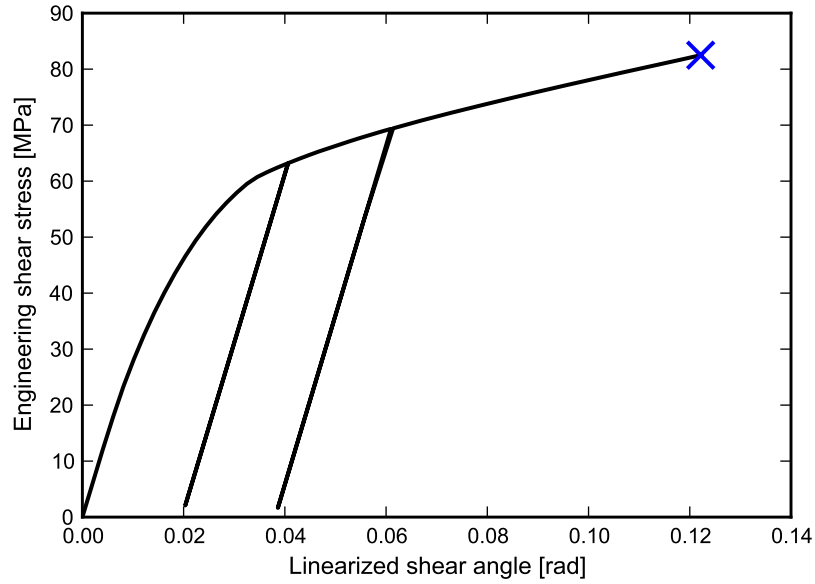


Figure 4.10: Predicted homogenized response of the unit cell due to macroscopic in-plane shear engineering stresses, τ_{xy} , with 2 unloading cycles (zero stress) vs. the linearized shear angle γ_{xy} . The cross marks the predicted peak load.

axial tensile stress state in a rotated coordinate system. In Fig. 4.11 the response of the unit cell subjected to the uniaxial stress along 45° is given. The unloading cycles reveal pronounced plasticity effects occurring in the tows and matrix pockets. Transverse damage evolving in the tows has no notable influence on the homogenized response of the unit cell. The dashed line indicates the strain range markedly influenced by the viscous regularization utilized for FEM convergence reasons. This range should be treated with caution since previous studies have shown that macroscopic softening, which cannot be predicted by force controlled loading, leads to a severe intervention of the viscous regularization scheme.

4.2.5 Intra-ply delamination

In this load case the delamination capabilities of the shell element based model are demonstrated. To this end the individual shells are coupled using the surface based cohesive contact formulation. Moreover, to overcome possible convergence issues all constituents are featuring linear elastic material properties. Respective interface and constituents data are again associated with the Cycom977/HTS40 material given in

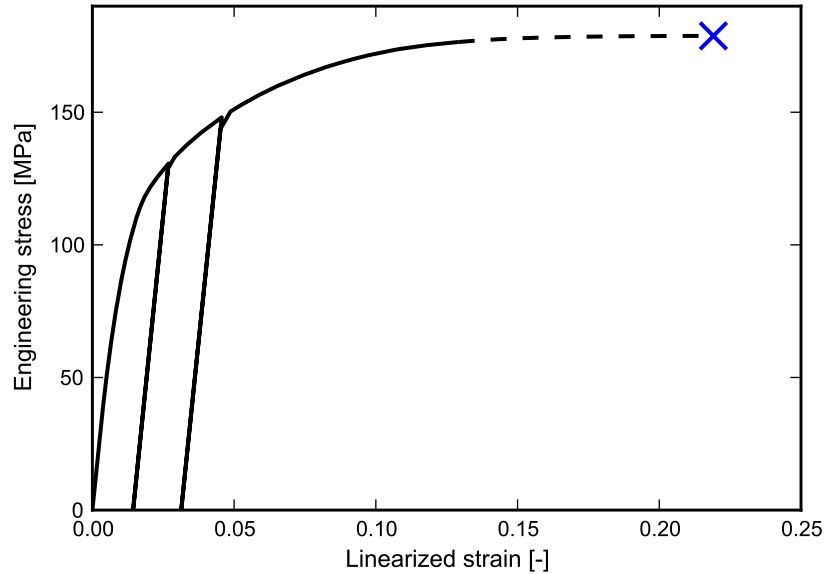


Figure 4.11: Predicted homogenized response of the unit cell due to macroscopic uniaxial in-plane tensile engineering stresses, $\sigma_{x'x'}$, in the 45° direction vs. the linearized strain, $\varepsilon_{x'x'}$, in 45° . The dashed line indicates the range heavily influenced by the viscous regularization; on the reloading curves time discretization artefacts are visible. The cross marks the predicted peak load.

App. A-Tab. A.3. The considered load situation is a displacement controlled in-plane simple shear load. For comparison, geometric linear as well as nonlinear assumptions are applied, however both yield nearly identical results in the reasonable regime. Therefore only the results of the geometric linear simulations are given next. A similar investigation is conducted for the Epoxy/IM6 material system in [44].

In Fig. 4.12 the engineering in-plane shear stress, σ_{xy} , is plotted against the linearized shear angle, γ_{xy} . To highlight the deviation from the linear response, the initial shear stiffness is plotted too (dashed line). The interface damage starts at a shear angle of about 0.015 but has no visible influence on the effective response in the beginning. With increasing load, interface damage accumulates at the edges of the overlapping tow areas. Starting at a shear angle of about 0.03, the response deviates from the linear solution and at about 0.06 delamination occurs locally (complete local failure of the interface). This quickly leads to the “peak load” after which the effective response shows a softening behavior. At this point the predicted shear stresses exceed realistic

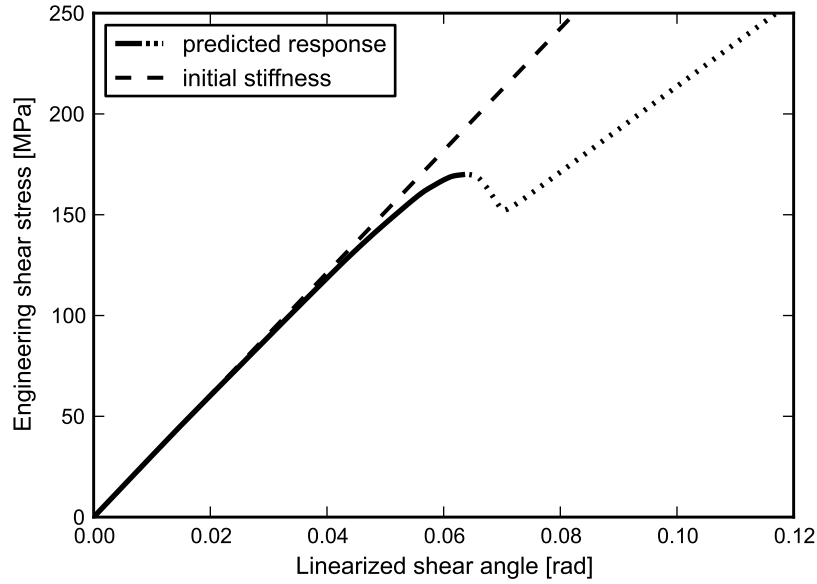


Figure 4.12: Predicted effective response, σ_{xy} vs. γ_{xy} , of the unit cell due to macroscopic in-plane shear loading with enabled delamination capabilities and linear elastic constituents behavior. The dashed line represents the initial stiffness (corresponding to the effective in-plane shear modulus G_{xy}), predictions exceeding the limits of applicability (see text) are indicated by the dotted line.

values because no other nonlinearities are included in the present model. In fact, tow plasticity would start at about 50% of the interface damage initiation load level, cf. Fig. 4.10. The stiffening (dotted line) behavior is attributed to the assumption of linear elastic materials and the undamageable couplings at the matrix edges, see Sec. 3.3. This is beyond the limits of applicability of the present approach but shows its robustness.

4.3 Verification of the lenticular cross section model

The additional matrix pockets and the accompanying change in the coupling scheme, require a verification for the lenticular tow cross section based unit cells as well. Similar to Sec. 4.1, the shell element based model of a 2/2 Twill weave is compared to a continuum element based model of the same weave. For the sake of brevity, only

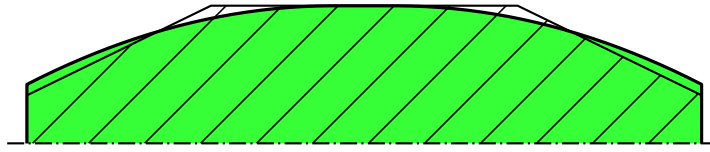


Figure 4.13: Comparison of the lenticular and trapezoidal tow cross sections. Note, the vertical direction is scaled by a factor of 5.

the initial stiffness and linear elastic stress field comparison is discussed next. The respective results have been published at [47].

4.3.1 Geometry and FEM model

The applied unit cell geometry tightly resembles the one used in the previous sections but originally features trapezoidal tow cross sections, see Marte [87]. As the current strategy relies on lenticular based cross sections, the respective dimensions are adapted to fit the original trapezoidal model in terms of fiber volume fraction and outer dimensions. Figure 4.13 illustrates the difference in the tow cross sections in an exaggerated way. The resulting geometry properties are listed in App. B denoted as *Lent-1*. A generic sketch of the UC cross section including dimensions is given in App. B Fig. B.2.

Again, a four times four tows UC is set up in the framework of the FEM using 4-noded shell elements with linear shape functions only. The elements used are fully integrated with five section points in the thickness direction applying Simpson rule integration. Due to the assumed lenticular based tow cross section a non-uniform shell thickness defined for the tows as well as for the unreinforced matrix pockets. All elements feature a typical element edge length of about $1/12^{\text{th}}$ of the tow width. The interfaces between the individual tows and between the tows and matrix are modeled by tie constraints implying perfect interfaces. The UCs lateral sides are coupled using plane periodic boundary conditions. For consistency reasons the same constituents properties are applied as defined in Sec. 4.1.

Reference model. The reference model was originally set up in [87] using quadratic tetrahedral elements with a typical element length of $1/26^{\text{th}}$ of the tow width. All in-

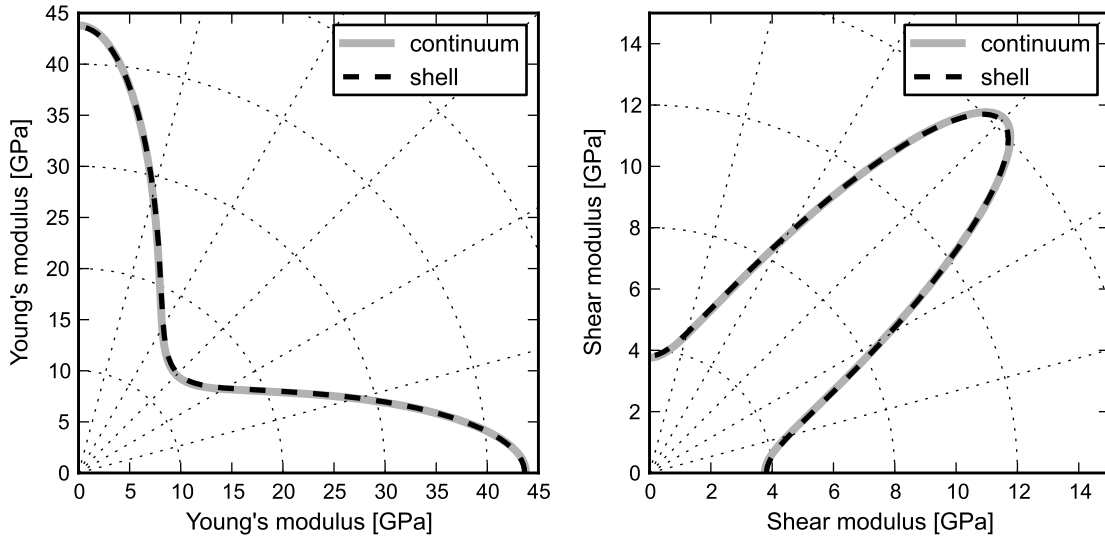


Figure 4.14: Polar plot of the predicted effective Young's modulus $E_{x'}$ (left) and the predicted effective shear modulus $G_{x'y'}$ (right) of the lenticular based shell and trapezoidal based continuum model.

interfaces are modeled as perfect and plane periodic boundary conditions are applied at the lateral sides.

4.3.2 Initial stiffness and elastic stress fields

The six independent load cases defined in Sec. 4.1.4 are simulated and the resulting effective stresses and strains are used to compute the homogenized shell stiffness matrix. Focusing on the in-plane elastic behavior, the shell element based model and the continuum element based model are juxtaposed in Fig. 4.14. It can be clearly seen, that both models are in an excellent agreement in terms of elastic stiffnesses. A similar statement can be given for the entries of the bending submatrix.

To give some comments on the predicted local stress fields, a uniaxial tensile loading along the x -axis applied to both models is used as an example. Figure 4.15 juxtaposes the predicted σ_{11} stresses at the tow top surface on the deformed meshes. For clarity the matrix pockets are removed in this plot. Both figures show qualitatively and quantitatively very similar results. However, a rather obvious difference in the stress fields can be seen as the local circular vs. deltoidal shaped compressive stress contours at the tow cross over points. The latter can be attributed to the lenticu-

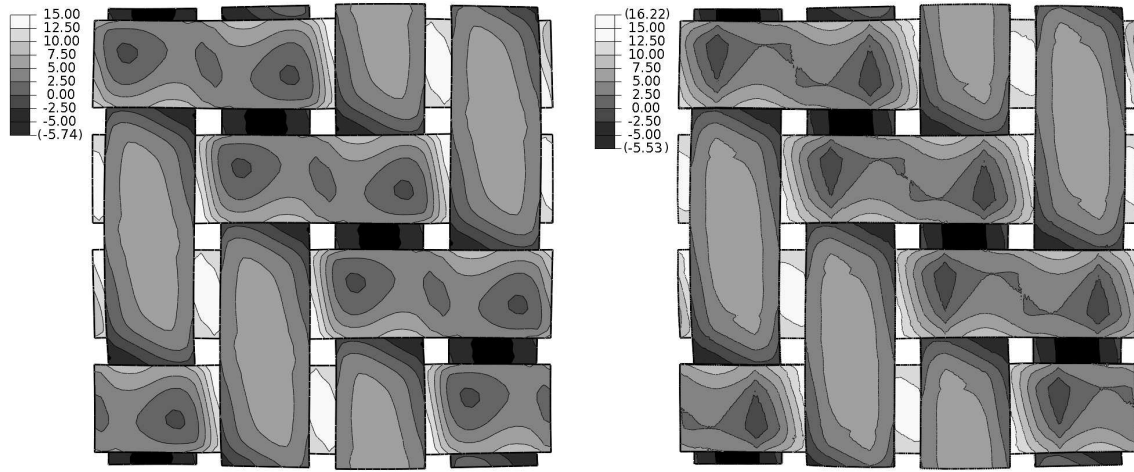


Figure 4.15: Predicted stress, σ_{11} , at the UC top surface due to uniaxial tensile loading along x of the lenticular based shell model (left) and the trapezoidal based continuum model (right), contour level delimiters are set equal in both plots and the matrix pockets are removed.

lar and trapezoidal, respectively, shaped cross sections and hence, is independent of the applied modeling approach. The difference between the maxima and minima, again, arises to the better part from the dissimilar discretization applied. Finally, the lenticular based approach also passes the isotropy test with a maximum deviation of 0.7%.

4.4 Multilayer composites

To demonstrate the capabilities of the proposed approach multilayer laminates comprising equal layers of 2/2 Twill weave are considered next.

To start with, the influence of the number of plies and the stacking scheme on the stiffness of the laminate is investigated and the initial shell stiffnesses are compared. In this context some comments are given on the locally different stress states in the interfaces are given as well. In a second step the geometric nonlinear response of single, double, and four layer laminates subjected to uniaxial stress states is juxtaposed and compared with experimental data. Finally, a load case giving rise to delaminations between the layers is discussed and respective results are given for a two layer laminate.

For all investigated laminates the individual layers are stacked with the same orientation. A variation of this angle within the laminate, as common with unidirectional plies, requires different in-plane periodicity vectors and, therefore, breaks the assumed periodicity. The presented results are published in [45].

4.4.1 Geometry and FEM discretization

The weave geometry is chosen to resemble the geometry studied in [33] and features truncated lenticular shaped tow cross sections. The corresponding undulation paths are modeled using straight and circular segments. The required dimensions are given in App. B using the ID *Lent-2*. The dimensions and the resulting fiber volume fraction are equal to the values defined in [33]. The single layer unit cell comprises four tows in each direction. This represents the smallest periodic repeating geometry pattern with orthogonal periodicity vectors. With an assumed fiber volume fraction of 70% in the tows, the considered weave exhibits a total fiber volume fraction of 45%, cf. [33].

Using the shell element based discretization approach described in Sec. 3.5 all constituents of the weave are modeled using shell elements only. The respective shell reference planes are meshed using 4 noded shell elements with linear shape functions. The elements used are fully integrated with five section points in the thickness direction applying Simpson rule integration. A typical element length of $1/10$ of the tow width is used. Depending on the conducted simulation a number of layers are modeled, stacked, and coupled appropriately. In the present section, only in-phase (IP) and out-of-phase (OP) stacked laminates are considered. However, other stacking sequences could be realised as well.

4.4.2 Material data

In the present study all layers are equal in terms of applied materials and architecture. The tows are modeled as being linear elastic, transversely isotropic, whereas the unreinforced matrix pockets are represented by a linear elastic, isotropic material. The respective data of the constituents are listed in the appendix Sec. A (Tab. A.2). The data was chosen in accordance with [33].

The cohesive elements applied to link the individual layers, feature a linear traction-separation law with a quadratic stress criterion and an energy based damage evolution, see [64]. If no delamination capabilities are required, only the initial (linear elastic) part is set active. Table A.2 gives the required material properties of the cohesive material. In this context, K_i denote the initial linear elastic interface stiffnesses, t_i^0 are the interface strength values, and \mathcal{G}_i are the critical energy release rates for delamination mode i . To deal with the mixed mode response a Benzeggagh-Kenane criterion is chosen with the parameter η as suggested in [13].

4.4.3 Initial effective shell stiffness of a multilayer weave

To compute the initial effective shell stiffnesses of a laminate six independent load cases are required as discussed before. Based on these simulations the ABD matrix can be derived for the considered laminates. The stacking schemes to be investigated are the extreme cases of in-phase and out-of-phase stacking, cf. Sec. 2.1.4.

In-phase stacking. To predict some lower estimate of the effective stiffness of a general, i.e. arbitrarily stacked, multilayer laminate a typical approach found in the literature is based on single layer UCs with distinct out-of-plane boundary conditions representing the in-phase stacking of an infinite number of layers. The respective conditions are realized by periodic boundary conditions in the out-of-plane direction. The question arises if laminates comprising only a few layers are reasonably assessed this way.

To give an answer to this question, six different laminates comprising (1), 2, 3, 5, 10, and 20 layers stacked in-phase are investigated. Figure 4.16 shows polar plots of the respective effective Young's moduli $E_{x'}$ (left) and effective shear moduli $G_{x'y'}$ (right) with $x' - y' - z'$ denoting a coordinate system, rotated with respect to the global z -axis. It can be seen that adding layers initially increases the effective stiffness of the laminate. This can be explained by the fact that neighbouring plies prevent the individual layers from warping. After reaching a certain amount of layer, the stiffness properties converge to stationary values. To highlight this convergence behavior, the Young's modulus in 0° direction as well as the shear modulus in 45° direction with respect to the number of layers is plotted in Fig. 4.17. Here, the moduli are normalized

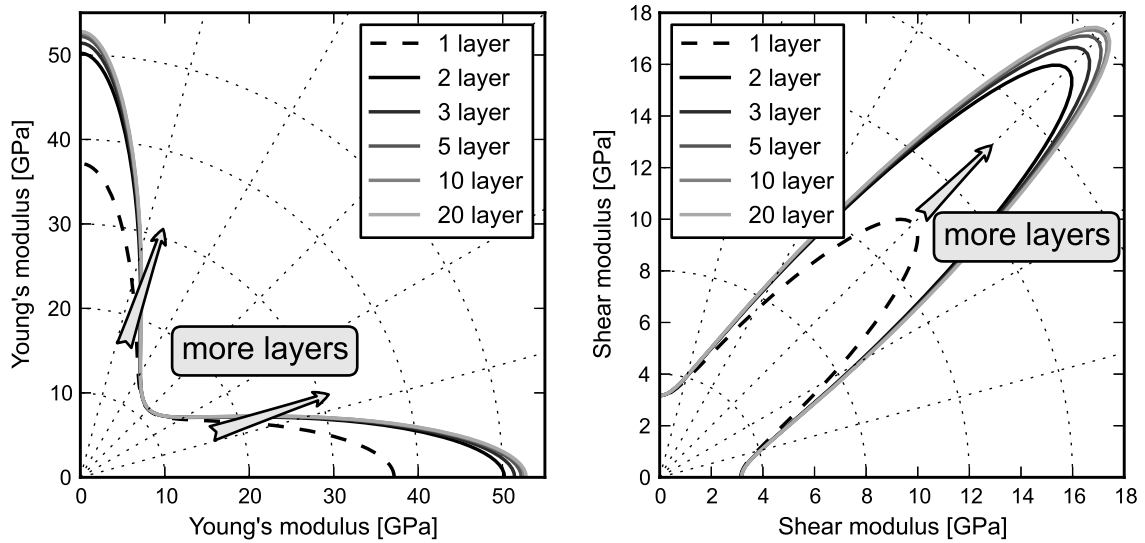


Figure 4.16: Polar plot of the predicted effective Young's modulus, $E_{x'}$ (left) and the predicted effective shear modulus, $G_{x'y'}$ (right) for a 2/2 Twill weave laminate comprising 1, 2, 3, 5, 10, and 20 layers, respectively, stacked in-phase.

to the periodic solution. As the present approach does not allow for the application of periodic boundary conditions in thickness direction, the periodic solution is roughly estimated based on the 10 and 20 layer laminate. Figure 4.17 shows that the periodic solution leads to an error in stiffness prediction of less than 1% if the in-phase laminate comprises at least 7 layers. A deviation of less than 5% in terms of effective Young's moduli can be expected for all laminates comprising more than one layer. Similar results are found if the effective shear moduli in the 45° direction are compared, see Fig. 4.16 (right). This time at least 9 layers are recommended to keep the deviation of the predicted shear stiffness below 1%.

An interesting phenomenon is that the effective Young's modulus in 45° direction as well as the shear moduli with respect to the x and y direction are insensitive to the number of layers. This can be explained by the pronounced $x - y$ shear component present under such loading conditions, which does not result in local warping of the single layered weave. Due to this lack of warping the out-of-plane constraint introduced by the adjacent layers has no effect on the effective stiffness of the laminate.

Out-of-phase laminates. To assess the influence of the number of out-of-phase stacked layers on the effective stiffness properties, similar considerations are applied as in the previous paragraph. Here, 2, 3, 4, 5, and 16 layers are simulated and the effective stiffnesses are plotted in Fig. 4.18. For comparison reasons this figure shows the respective curves of the single layer and the 20 layer in-phase stacked laminate as well. The results indicate that the response of the out-of-phase laminate is nearly independent of the number of plies. An uneven number of plies tend to be slightly more compliant as one layer lacks the compensating counterpart. This difference however, diminishes with increasing layer count. Again, the effective Young's modulus in 45° direction as well as the shear moduli with respect to the x and y -direction are insensitive to the number of layers and exhibit nearly identical values as the single layer and the in-phase stacked laminate.

Note on interface tractions. The common approaches of replacing the stack of plies by simple boundary conditions lacks the ability to accurately represent of the variation of stress fields with respect to the position of the layer within the laminate,

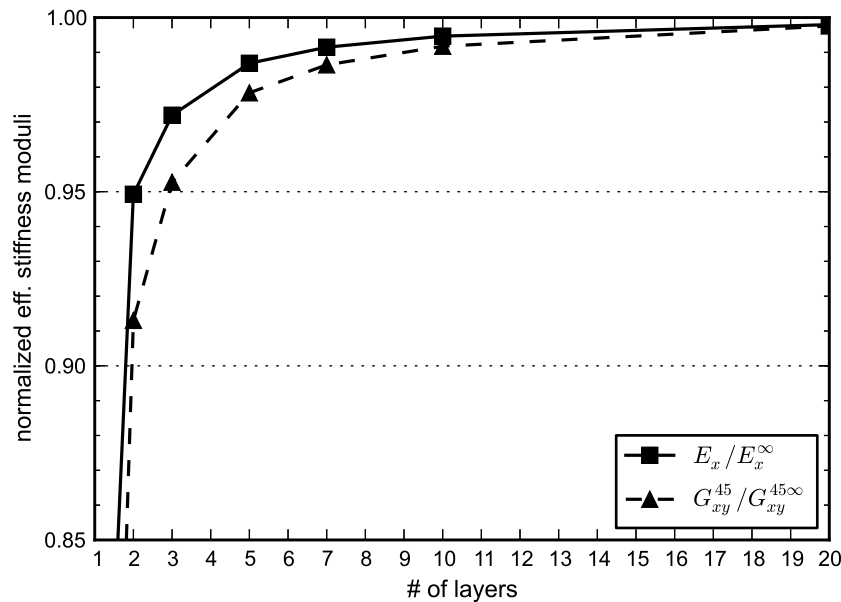


Figure 4.17: Predicted development of the normalized effective Young's modulus in x (solid line) and normalized effective shear modulus in 45° -direction (dashed line) with respect to the number of plies in the in-phase laminate.

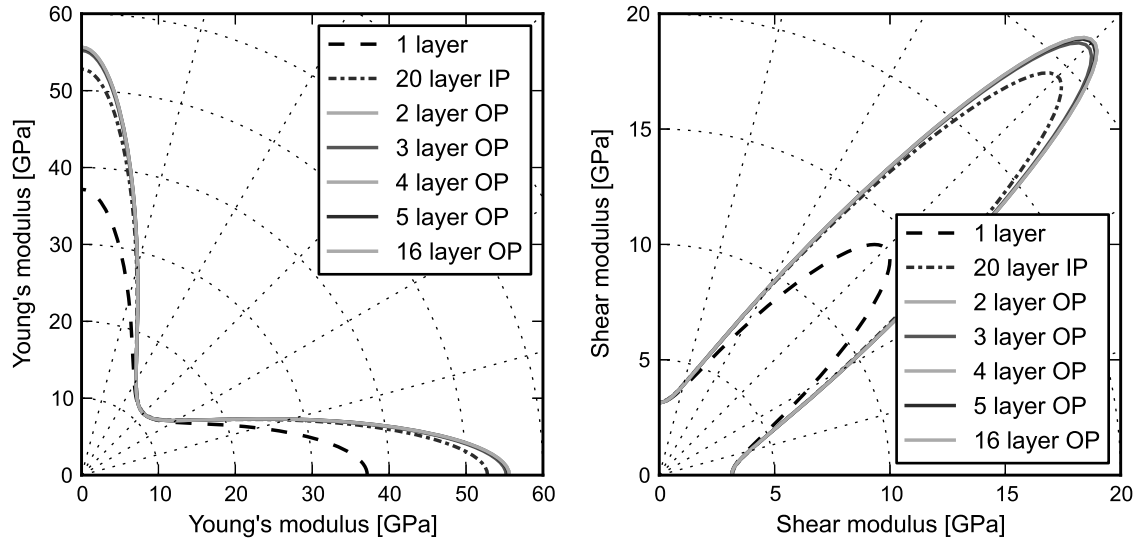


Figure 4.18: Polar plot of the predicted effective Young's modulus, $E_{x'}$ (left) and the predicted effective shear modulus, $G_{x'y'}$ (right) for a 2/2 Twill weave laminate comprising 2, 3, 4, 5, and 16 layers stacked out-of-phase. The moduli for stacks with an even number of layers are nearly coincident for all the conducted configurations. For comparison, the stiffness of a single layer and a 20 layer in-phase stacked laminate are given as well.

see e.g. [69]. Here, especially the interlaminar interface tractions are considered. Figure 4.19 shows the respective interface normal tractions of an 8 layer in-phase (left) and out-of-phase (right) stacked laminate subjected to uniaxial tensile stress in x -direction. To improve the visibility only the interface elements are shown and the z -coordinates are scaled by a factor of 10. The in-phase stacking shows a continuous variation in the normal interface tractions with respect to the z -position. These tractions follow the local warping pattern which develops during loading like in a single layer. The out-of-phase stacked laminate shows completely different interface stress fields. The counter warping of adjacent layers lead to high tensile and compressive stresses every second interface. The other interfaces are only slightly loaded.

4.4.4 Geometric nonlinear response

As shown by multiple authors, the geometric nonlinear response of a single layer of 2/2 Twill weave subjected to uniaxial tensile stresses in a tow direction exhibits

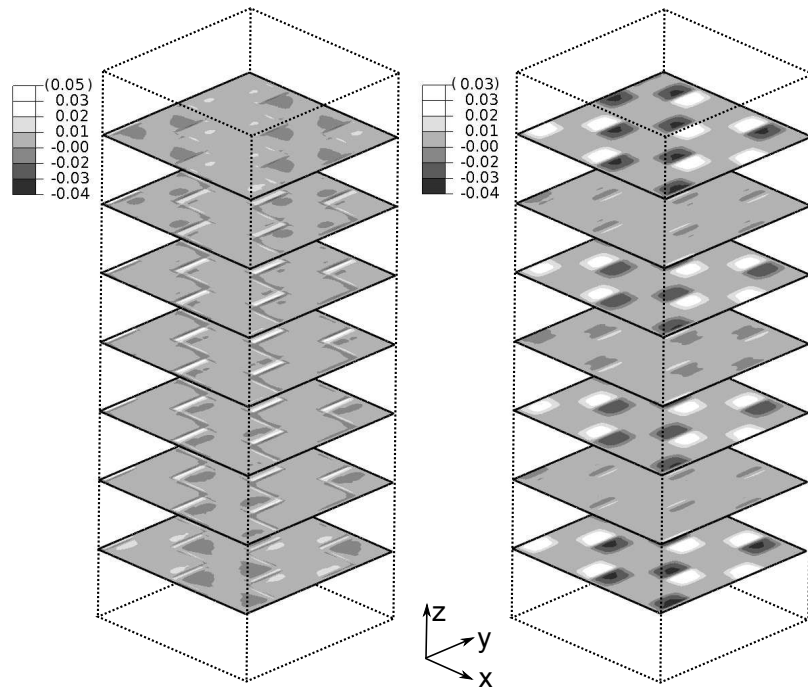


Figure 4.19: Predicted σ_{zz} tractions at the interlaminar interface elements due to uniaxial tensile stresses in x -direction for 8 layers stacked in-phase (left) and out-of-phase (right) with equal contour level delimiters. The z -coordinates are scaled by a factor of 10 to improve visibility.

stiffening behavior. This can be attributed to the flattening of the undulated tows. To investigate the respective behavior of multilayer laminates, 2 and 4 layers are stacked in-phase, and out-of-phase, respectively, and loaded in tension along a tow direction. Figure 4.20 shows the predicted responses in terms of effective engineering stresses against effective linearized strains. For comparison reasons the response of a single layer (thin, dashed, black line) and some experimentally determined curves (thin, black lines) are added. The latter are extracted from [33]. To give some strength measure, a cross marks the FPF point predicted using Hashin's criteria [63] and the experimental failure points are indicated using a circle.

The in-phase laminates follow the findings of the initial stiffness comparisons discussed before, i.e. more layers lead to an initially stiffer laminate. Due to the not totally restrained local warping in these laminates, some stiffening occurs with the 2 layer in-phase laminate. The 4 layer in-phase laminate shows already hardly any geometrical stiffening. As expected, the two out-of-phase laminates exhibit no geo-

Table 4.2: Computational requirements for the geometric nonlinear simulations of multilayer composites using the shell element based approach on a 4 CPU workstation.

Laminate	DOF	Simulation time [sec]	Memory requirement [MB]
1 layer	81,756	92	206
2 layer	163,512	120	552
4 layer	327,024	260	1,391

metrical stiffening and coincident responses. The latter laminates get more compliant with increasing deformation.

Comparing the predicted results with the experimental curves, a good agreement can be found. As expected the OP laminates are slightly to stiff, whereas the IP laminates are slightly to compliant. Both four-layer laminates and the two-layer IP laminate predict a FPF at about 0.96% effective strain. The two-layer OP laminate exhibits a slightly increased FPF strain. However, the predictions are in a good agreement with experiments. It may be noted, that for the present loading situation the weave shows a rather linear response, hence linear elastic constitutive behavior is sufficient. When loading changes, this is no longer true and nonlinear constituent models have to be included, see Sec. 4.2.4. In Tab. 4.2 the number of DOFs, the memory requirements, and the simulation times for geometric nonlinear simulations are presented. These numbers are based on a desktop workstation with 4 CPUs. Compared with respective requirement of continuum element discretized models, see e.g. Tab. 4.1, these numbers reveal the potential of the approach to enable nonlinear simulations of explicitly modeled multilayer textile laminates on typical workstations.

4.4.5 Delamination between layers

As already demonstrated, the combination of multiple layers stacked out-of-phase leads to an increase of the effective stiffness since the occurring local warping is inhibited by the adjacent layers. This prevention of the warping leads to interface tractions which, in turn, might give rise to delaminations. To investigate this phenomenon a two layer laminate in an out-of-phase stacking configuration subjected to

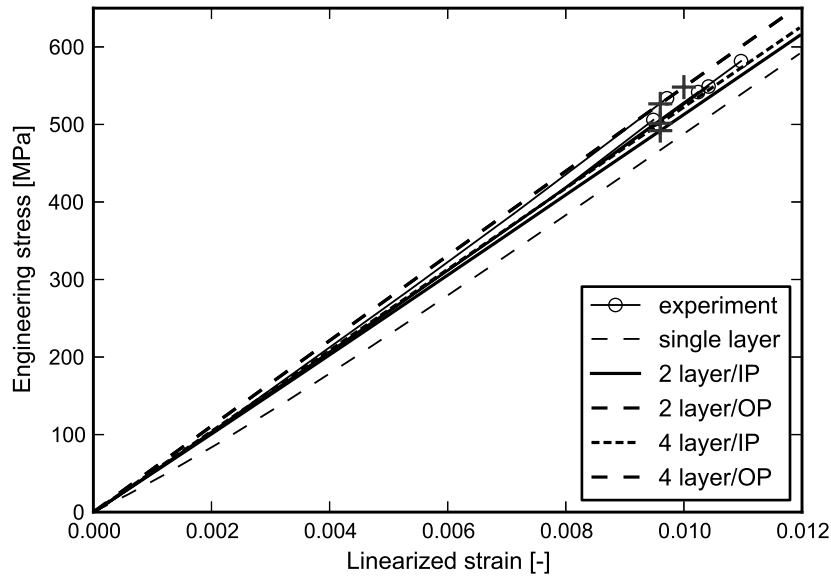


Figure 4.20: Predicted geometric nonlinear response in terms of engineering stresses, σ_{xx} , against linearized strains, ε_{xx} , due to uniaxial tensile loading in x direction for 5 different laminates. The two out-of-phase laminates exhibit coincident responses, the pluses denote the predicted FPF and the circles indicate the experimentally determined failure points.

uniaxial tensile stresses in x -direction is simulated. To ensure enough cohesive elements within the process zone, i.e. the zone between complete and zero damage of the interface, the element size of the cohesive elements is adapted following [132]. Figure 4.21 shows the interface normal tractions at an effective strain of $\varepsilon_{xx} = 0.014$. The respective interface shear tractions are well below the critical value and are therefore not presented here. As expected, the areas of high interface tractions, cf. Fig. 4.19, delaminate during simulation, respective cohesive elements are removed for clarity. However, in the present configuration the axial tensile tow stresses, σ_{11} , reach the tow strength earlier than the interface traction gets critical. The corresponding load levels for initiation of tow failure and delamination, respectively, differ about 10%. This suggests that failure of the tows is likely to occur first and the predicted delamination pattern is therefore somewhat academic. A delamination triggered by the local failure of tows is possible, of course.

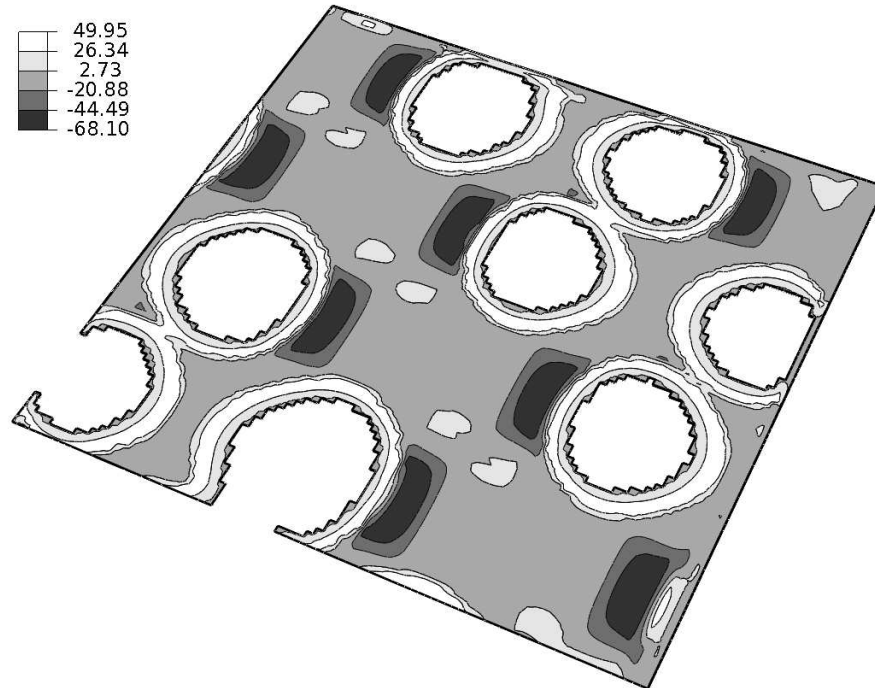


Figure 4.21: Predicted normal tractions σ_{zz} of the interlaminare cohesive elements due to uniaxial tensile stress at an effective strain of $\varepsilon_{xx} = 0.014$ applied to a two layer OP laminate of equal weaves, already failed elements are removed to indicate delaminated areas and the adjacent weave layers are suppressed.

4.5 Braided composites

So far only orthogonal textiles are considered, however as proposed in Sec. 3.6, an affine transformation can be used to generate unit cells representing braided textiles with braiding angles unequal 45° . Braided textiles in structural application often feature a dense topology. As latter cannot be modeled by most (including the present) geometric representations, an open topology is used to approximate the real textile. Therefore, the modeled UCs feature a larger periodic length than the measured “real” specimens. This results in a lack of fiber volume fraction and thus, in a different overall mechanical response. To cope with this problem the constituents material data is commonly scaled to achieve the required fiber volume fraction, see e.g. [14]. This procedure, also called “normalization”, is strictly speaking unphysical as the disability of the modeling approach is compensated with an artificial change of the material data. Nevertheless, it is common practice, as no better approach exists yet.

The scaling can be introduced based on various assumptions like linear correlation or micromechanical methods. In case of high volume fractions, micromechanical methods tend to give to high properties, hence for the current project a linear correlation between elastic material properties and fiber volume fraction is assumed. With this in mind, the two Young's moduli, the shear modulus and the (brittle) longitudinal tensile as well as compressive failure strength of the tow material are altered. All other properties are kept as originally defined.

Due to the underlying elastic symmetries imposed by the braiding topology, the major coordinate system is switched to the $\xi - \eta - \zeta$ coordinate system for the rest of this chapter.

In the following the influence of the braiding angle on the elastic properties of single and multilayer laminates featuring Regular braid (Twill type) topology is investigated. This considerations include the differences and similarities of braids with complimentary braiding angles. Subsequently, a $\pm 45^\circ$, $\pm 30^\circ$ and a $\pm 60^\circ$ braid is simulated including nonlinear tow behavior and compared with respective experimentally determined results obtained the cooperation partners PCCL and LCC.

4.5.1 Influence of braid angle on elastic properties

Assuming equal tow cross sections for all braiding angles, the initial stiffness properties of single and multilayer braids featuring different braiding angles are predicted and juxtaposed. The applied textile geometry dimensions are listed in Tab. B.1 denoted as *Braid-45*. It is based on micrograph measurements of a $\pm 45^\circ$ braid conducted by the cooperation partner LCC using samples provided by PCCL. This geometry is used for all investigated braiding angles to achieve a reasonable comparability despite the fact that in reality different braiding angles result in different tow cross sections. To account for the skewing the initially modeled tow cross sections have to be adapted appropriately.

Single layer unit cells are set-up using the lenticular tow cross section based approach defined in Sec. 3.4. Four noded fully integrated shell elements with a Simpson type thickness integration (5 section points) and a typical element size of $1/12^{\text{th}}$ are used. The resulting UCs feature a total fiber volume fraction of 53.7% based on a fiber volume fraction in the tows of 70%. The real $\pm 45^\circ$ braid was measured to features

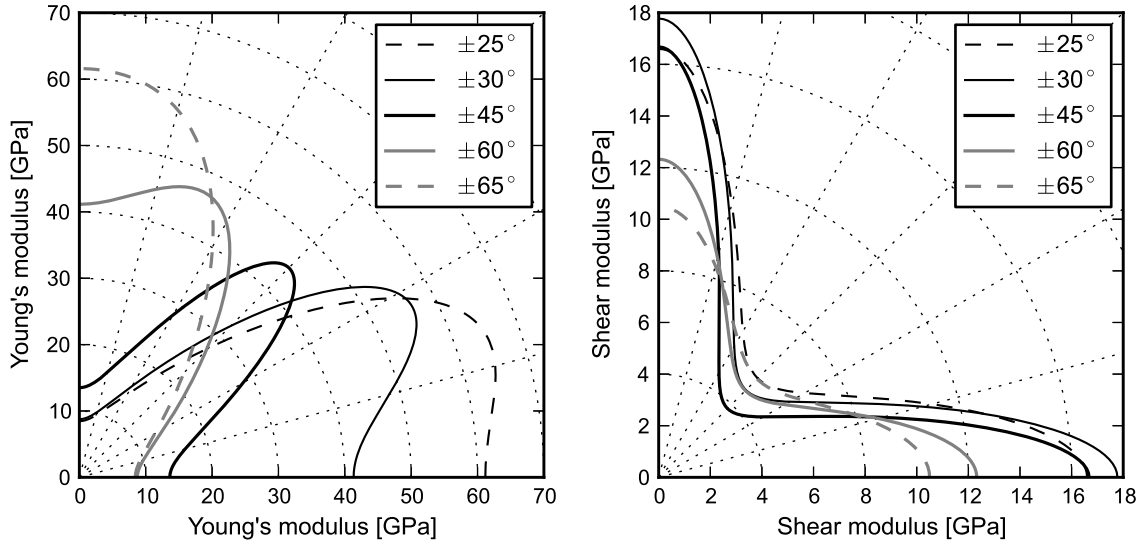


Figure 4.22: Polar plot of the predicted effective Young's modulus, E'_ξ (left) and the predicted effective shear modulus, $G_{\xi'\eta'}$ (right) for a single layer Regular braid featuring a braiding angle of $\pm 25^\circ$, $\pm 30^\circ$, $\pm 45^\circ$, $\pm 60^\circ$ and $\pm 65^\circ$, respectively.

a total fiber volume fraction of 60%, hence, the tow fiber volume fraction has to be increased to 78%. Respective scaled material data is given in Tab. A.4. All constituents feature linear elastic stress-strain relations and the interfaces are considered to be perfect.

Figure 4.22 shows the respective polar plots of the initial Young's moduli (right) and shear moduli (left) with respect to the loading direction of a single layer braid. It can be clearly seen, that there is a significant influence of the braiding angle on the elastic constants. As expected lower braiding angles lead to higher stiffness in braiding direction and vice-versa. A quick look at the Young's modulus curves suggests that the $\pm 45^\circ$ braid features a tetragonal symmetry whereas the other braids show an orthotropic symmetry, cf. [100]. This suggestion will be further discussed later.

When comparing the shear moduli in braiding direction, $G_{\xi\eta}$, (Fig. 4.22 right), one would expect the $\pm 45^\circ$ braid to feature the highest value as the shear loading in braiding direction can be transferred into a tensile-compression loading in a 45° rotated coordinate system. However, the $\pm 30^\circ$ braid shows an even higher value. To explain this somehow unexpected behavior, the Poisson's ratios have to be examined as well. Figure 4.23 (left) shows the first quadrant of the respective polar plots for some of

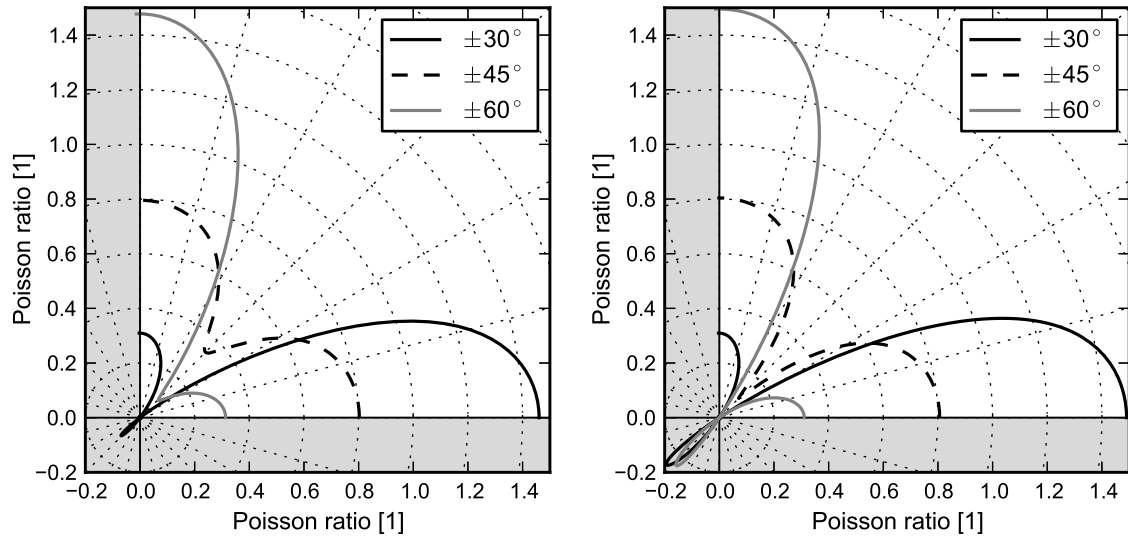


Figure 4.23: Detail of the polar plot of the predicted effective Poisson's ratio, $\nu_{\xi'\eta'}$ for a single layer Regular braid (left) and for a 4 layer IP stacked Regular braid laminate (right), both featuring a braiding angle of $\pm 30^\circ$, $\pm 45^\circ$ and $\pm 60^\circ$, respectively; only values related to the first quadrant are shown.

the braiding angles. The negative Poisson's ratio of the $\pm 30^\circ$ braid in 45° direction in conjunction with a tensile-compressive load pair leads to an increased shear stiffness compared to the $\pm 45^\circ$ braid. One may wonder why the response of the $\pm 30^\circ$ and $\pm 60^\circ$ braid is that different. This question will be answered in Sec. 4.5.2.

Multilayer braids. For comparison reasons, the same geometry (*Braid-45*) is used to setup a four layer in-phase laminate. Figure 4.24 shows polar plots of the initial elastic constants. Again a strong dependence of the elastic behavior on the braid angle can be seen. The Young's modulus curves look similar to the single layer ones except for the higher values. This increase in stiffness can be attributed to the adjacent layers as shown in previous sections. Compared with the single layer curves, the shear modulus polar plots have changed significantly. Here, the $\pm 45^\circ$ braid shows the highest value with respect to the braiding direction. Moreover, the curves of the $\pm \alpha^\circ$ and $\pm(90^\circ - \alpha^\circ)$ braids are nearly coincident. The polar plot of the Poisson's ratio (Fig. 4.23 right) reveals that the values at 45° are negative for the non-orthogonal braids. This, so called auxetic behavior is even more pronounced

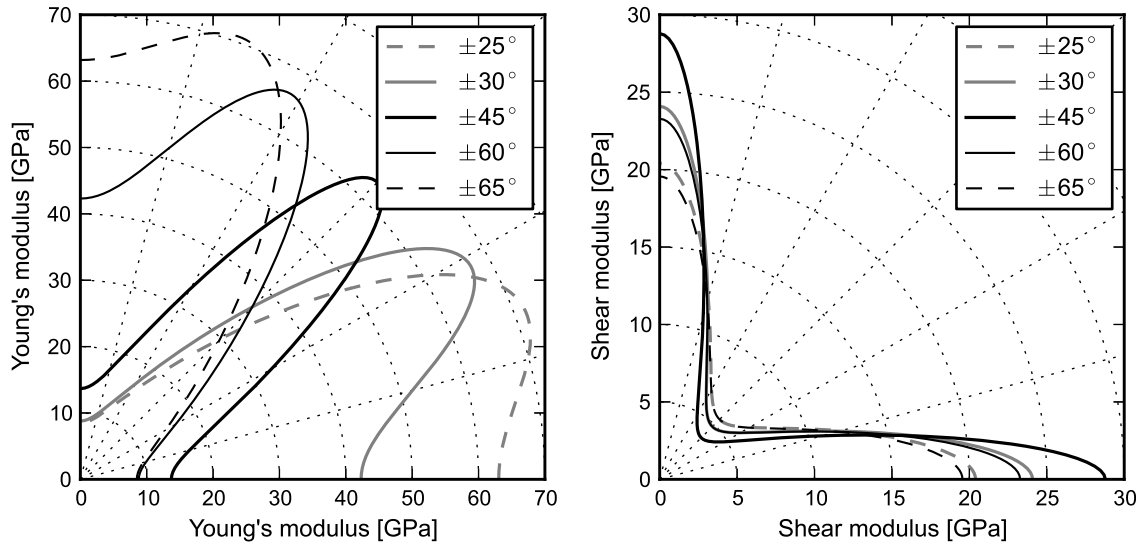


Figure 4.24: Polar plot of the predicted effective Young's modulus, E'_ξ (left) and the predicted effective shear modulus, $G_{\xi'\eta'}$ (right) for a 4 layer IP stacked Regular braid laminate featuring a braiding angle of $\pm 25^\circ$, $\pm 30^\circ$, $\pm 45^\circ$, $\pm 60^\circ$ and $\pm 65^\circ$, respectively.

than in the single layer case. Nevertheless, the fairly low Poisson ratio and the very high Young's modulus in 45° direction explains the maximum shear stiffness of the $\pm 45^\circ$ braid.

4.5.2 Complementary braid angles

When looking at the topology of a $\pm\alpha^\circ$ and $\pm(90^\circ - \alpha^\circ)$ braid, one would first expect both to feature the same orthotropic behavior, just rotated 90° , however, the moduli of such a pair may show a significant difference, see e.g. Fig. 4.25. In this figure, the response of the single layer $\pm 60^\circ$ is rotated to directly compare to the $\pm 30^\circ$ braid's. When looking at the multilayer responses, Fig. 4.26 this difference is not that pronounced. Hence the comparability depends on the number of layers. Or, to be more specific, on the deformation of the UC. As already shown in Sec. 4.1.4 a Regular braid tends to warp locally if loaded in tow direction. This warping always aligns with the braiding direction, i.e. the wave crest is parallel to the braiding direction. Figure 4.25 reveals that the difference is maximum at about 30° – a tow direction. In Fig. 4.27 the deformed UCs due to this particular loading condition is juxtaposed

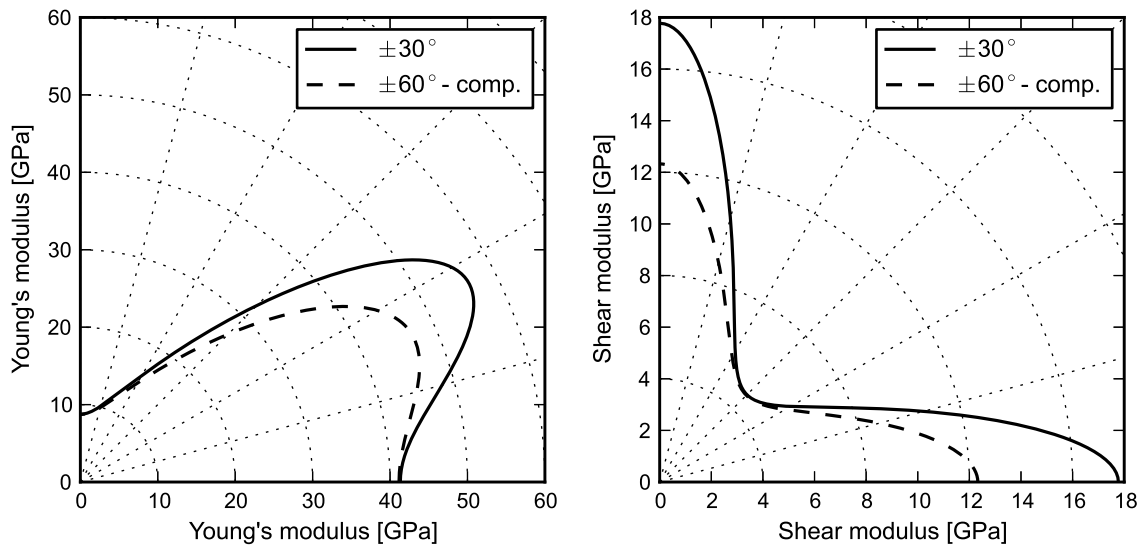


Figure 4.25: Polar plot of the predicted effective Young's modulus, E'_ξ (left) and the predicted effective shear modulus, $G_{\xi'\eta'}$ (right) for a single layer $\pm 30^\circ$ Regular braid and the complementary $\pm 60^\circ$ braid (rotated).

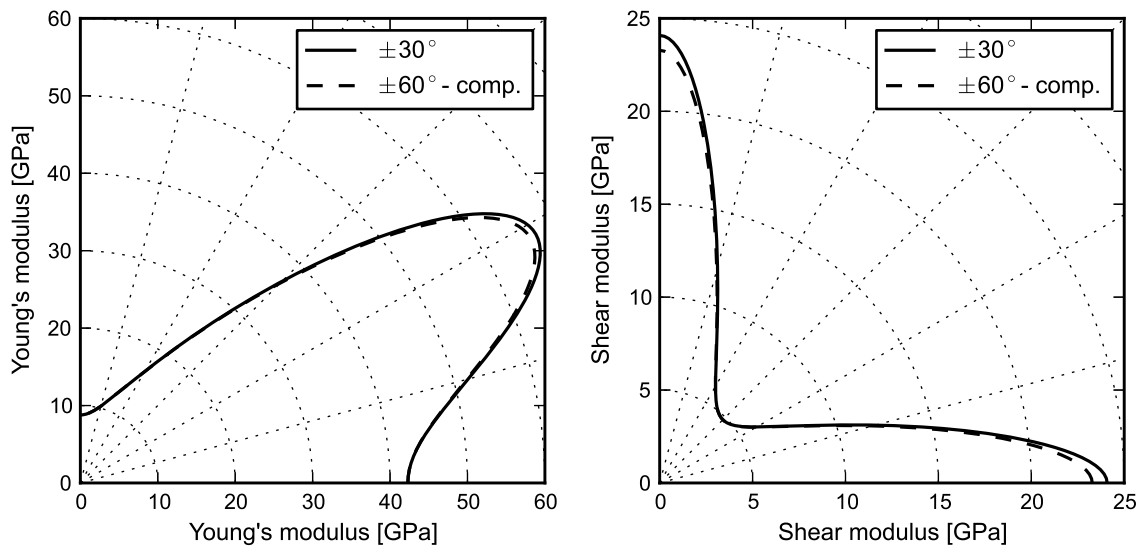


Figure 4.26: Polar plot of the predicted effective Young's modulus, E'_ξ (left) and the predicted effective shear modulus, $G_{\xi'\eta'}$ (right) for a 4 layer IP $\pm 30^\circ$ Regular braid and the complementary $\pm 60^\circ$ braid (rotated).

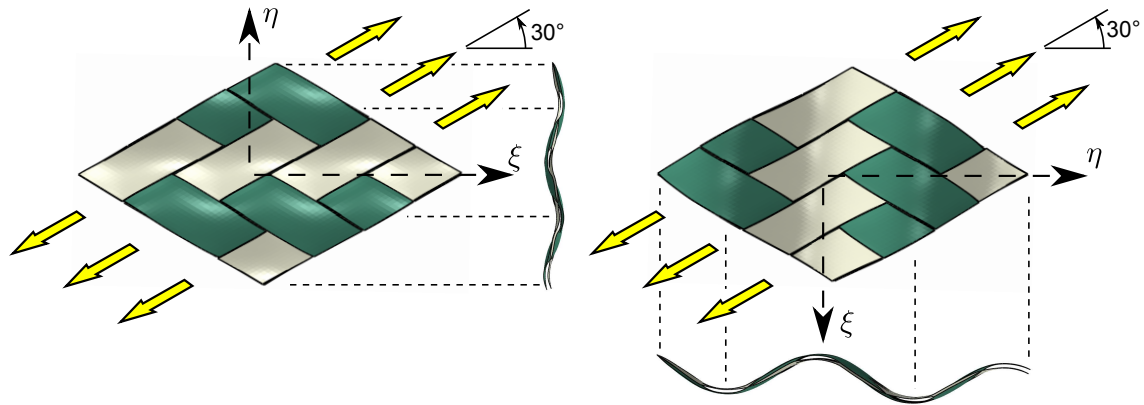


Figure 4.27: Comparison of the complimentary angle braids $\pm 30^\circ$ (left) and $\pm 60^\circ$ (right), including side-view showing the local warping.

for the two braids. Additionally, the local warping patterns are indicated by a cross sectional view. It is clearly visible that for the $\pm 60^\circ$ braid (right) the applied loading direction is in a better agreement with the wave direction than for the $\pm 30^\circ$ braid. This better alignment, leads to a more pronounced warping and thus, to a lower stiffness of the $\pm 60^\circ$ braid. Moreover, the local warping immediately explains why multilayer laminates lead to more similar responses as such ones alleviate this local deformation. Note that, loading directions which do not introduce warping, like the braiding direction, show equal results for both types of braids.

This investigations suggest that as long as multilayer Regular braids are considered, the assumption of equal, but rotated, material properties for braids with complimentary braiding angles is reasonable. However, in the rare case of single layer braids, one has to distinguish between the respective $\pm\alpha^\circ$ and $\pm(90^\circ - \alpha^\circ)$ textile.

4.5.3 Nonlinear simulation of a $\pm 45^\circ$ single layer braid

The nonlinear response of a $\pm 45^\circ$ braid subjected to uniaxial tensile stresses in braiding and tow direction, respectively, is investigated. To this end a UC is set-up using the lenticular based approach. The applied textile geometry is determined by micrograph measurement by the cooperation partner LCC and listed in Tab. B.1 denoted as *Braid-45*. These measurements describe a dense braid with the spacing of the tow center lines smaller than the tow width. As this cannot be modeled using the present approach the data is adapted to match the measured values in a feasible way.

Four noded fully integrated shell elements are used throughout the whole UC featuring a Simpson type thickness integration with 5 section points is specified. To get a reasonable compromise between simulation time and accuracy a typical element size of $1/12^{\text{th}}$ is used.

As already discussed in the previous section a normalized material data set accounting for the required fiber volume fraction is computed as given in Tab. A.4. To incorporate material induced nonlinear effects, the tows are equipped with the *EPD-model* model introduced in Sec. 2.2.3. This material model allows for residual strain accumulation as well as stiffness degradation accompanied by strain hardening and strain softening, respectively. The unreinforced matrix pockets are represented using a linear elastic material. All interfaces are treated as being perfect. The loading conditions are applied in a force controlled way, as the underlying master node concept does not allow for the direct application of arbitrary loading states in a displacement controlled way. Since the reorientation of the material coordinate systems have a pronounced effect on the structural response geometrical nonlinear simulations are conducted.

The predicted stress-strain curves are compared with experimental results. The latter are supplied from the cooperation partner PCCL and are based on 8 layer specimens comprising the $\pm 45^\circ$ braid, see [18]. Figure 4.28 shows the predicted response of the $\pm 45^\circ$ braid with respect to a uniaxial tensile load in braiding direction (black line) and a few experimentally determined curves (gray lines) in terms of linearized stresses and engineering stress. The black cross marks the point at which 1.5% of the total energy in the system is dissipated by the viscous regularization mechanism. This point is considered as the failure point as the increase in viscous regularization energy indicates pronounced softening phenomena within the unit cell.

It can be clearly seen that, with respect to this loading conditions the braid shows a pronounced nonlinear behavior. This nonlinearity can be attributed to the plasticity effect taking place in the tows and matrix pockets. The overall trend of the simulated curve corresponds well with the experimental data. The prediction looks to compliant, however it matches one of the experimental curves quite perfectly, which suggests that the chosen, adapted, braid geometry represents a rather compliant part of the investigated specimen. A statistical consideration of different tow cross section may be appropriate here. The predicted failure load is in a good agreement with the maximum experimental failure load. Some of the experimental curves exhibit a

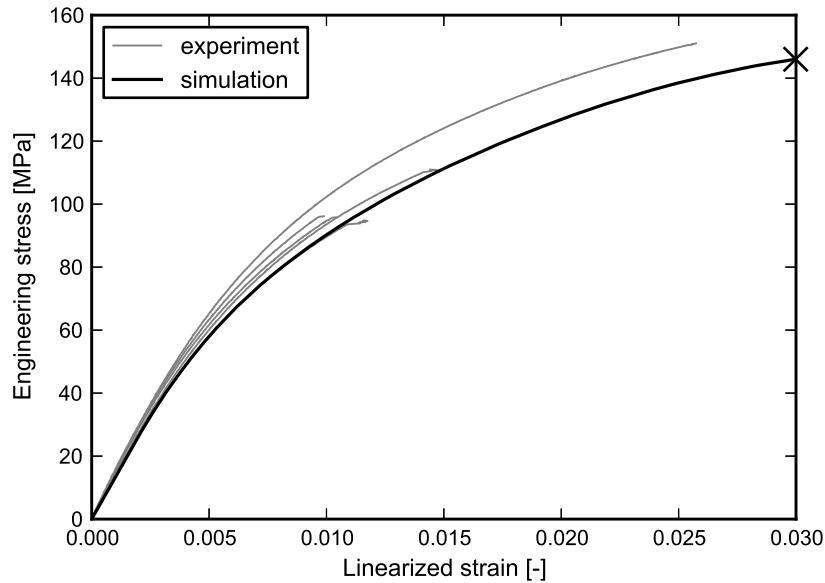


Figure 4.28: Predicted homogenized response of the $\pm 45^\circ$ Regular braid unit cell due to macroscopic tensile stress, $\sigma_{\xi\xi}$, in braiding direction (black) compared to respective experimentally determined curves (gray). The black cross marks the predicted failure state.

failure load which is about 47% lower. The reason of the premature failure of those experiments is not known to the author, but could be caused by non-uniform load distribution within the specimens. During load increase the model develops large plastic zones all over the tows. Simultaneously, transverse damage appears at the cross over points but remains very localized. At elevated loads, this matrix failure grows along the tows and finally leads to the failure of the UC.

The second considered load case is a uniaxial tensile loading along a tow direction. As been shown before, loading of a Regular braid in tow direction leads to local warping. The respective response is highly dependent on the number of layers in the laminate, thus, besides the simple (free) single layer simulation (Fig. 4.29, solid black line) a second simulation with locked out-of-plane DOFs is conducted (dashed black line). The latter represents the extreme case of a laminate with an infinite number of out-of-phase stacked plies, see Sec. 2.1.4. Figure 4.29 gives the predicted responses in terms of linearized stresses and engineering stresses juxtaposed with the experimental data (gray lines). The difference in initial stiffness of the two simulated curves can be clearly seen. The OP results are in a much better agreement with

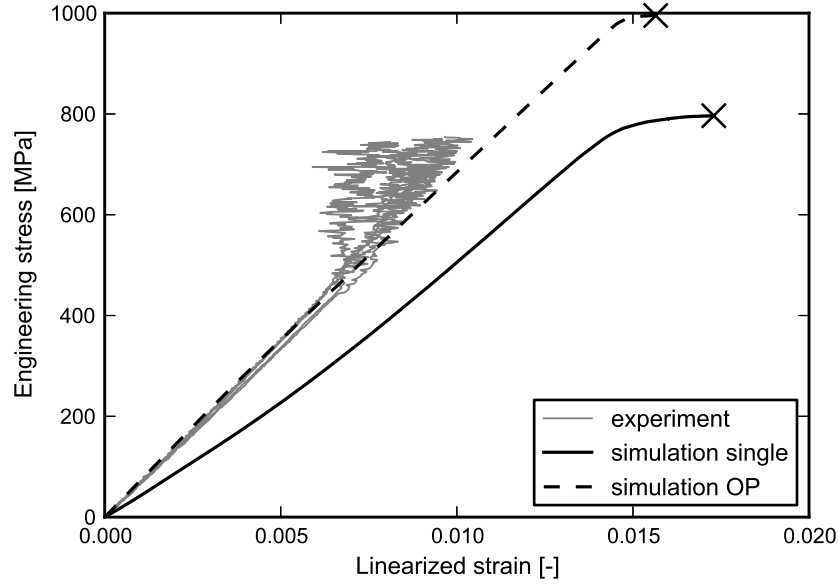


Figure 4.29: Predicted homogenized response of a free (black solid) and an OP-locked (dashed) single layer $\pm 45^\circ$ Regular braid unit cell due to macroscopic tensile stress, $\sigma_{\xi'\xi'}$, in x , i.e. a tow direction, compared to respective experimentally determined curves (gray).

the experimental data, which indicates that within the laminate the local warping is significantly suppressed, as discussed earlier in Sec. 4.4. The predicted failure strength for the free model is in good agreement with the experimentally determined strength. The increased strength of the OP case may be explained by the prevented local tow bending due to the additional boundary conditions. The latter effect is an artefact of the current modeling approach. For both simulation models the failure sequence is similar. At about 0.4% strain the tow normal to the loading direction starts to degrade in transverse direction. When reaching about 1.5% strain these tows split parallel to the fibers and concurrently the tows in loading direction start to fail.

4.5.4 Nonlinear simulation of a $\pm 30^\circ$ single layer braid

In this section the response of a $\pm 30^\circ$ braid is investigated. To this end the UC is subjected to uniaxial tensile loads in and perpendicular to the braiding direction as well as in tow direction and the respective results are compared with experimen-

tally determined ones. Like in the previous section the braid geometry is based on micrograph measurements provided by the cooperation partner LCC. The applied dimensions are listed in Tab. B.1 denoted as *Braid-30*. Again some adaption was necessary to derive a feasible set of geometrical data matching the measured values. The total fiber volume fraction achieved based on a tow fiber volume fraction of 70% is 47.7%. With a measured total fiber volume fraction of the real braid of 60%, some normalization is necessary. The UC is set-up using the lenticular based approach using 4 noded, fully integrated shell elements with a 5 section points Simpson based thickness integration. A typical element size of $1/12^{\text{th}}$ of the tow width is chosen. The braid comprises the same RTM6/HTS40 material system as used above, however, due to the changed geometry the required tow fiber volume fraction is adapted to 88%. Respective material data is given in Tab. A.5. The tows feature the *EPD-model* material model, the matrix pockets exhibit a linear elastic model and all interfaces between the constituents are set to be perfect.

The experimental results are taken from [19] and are determined for a 5 layer laminate of the same braid as defined as *Braid-30*. The first considered load case is uniaxial tensile stress in braiding direction. As this loading state does not lead to local warping, only a free single layer simulation is conducted, cf. 4.4.3. Figure 4.30 shows the predicted linearized strain vs. engineering stress response of the $\pm 30^\circ$ braid (black line) compared to the experimental result (gray line). In general both lines are in an excellent agreement, even though the predicted failure strength is about 7% off. At the same time, the predicted failure strain matches the experimentally determined one very well.

The second investigated load case is uniaxial tensile stress in a tow direction. As discussed in the previous section, two predictions are presented, one for a free single layer and one for an OP-constrained layer. Figure 4.31 shows the respective effective responses compared with the experimental results. Again, the free layer possesses a far to low initial stiffness but at higher strains, the stretching of the tows lead to a predicted tangential stiffness which corresponds very well with the experimental value. The OP results are somewhat too stiff at the beginning but fit quite well at higher strains. Both results can be explained by the fact that a 5 layer laminate still exhibits some local warping flexibility and hence, shows some stiffening behavior. The predicted failure strength of the free layer model is in a good agreement with

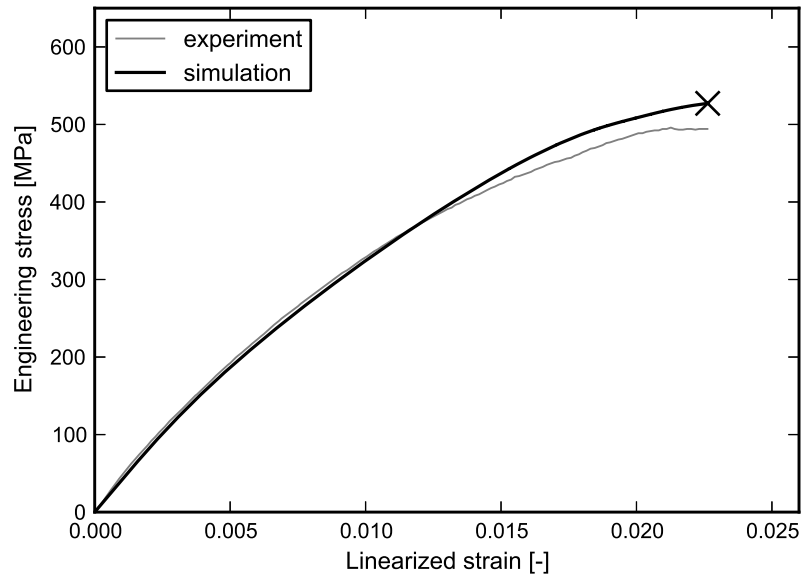


Figure 4.30: Predicted homogenized response of the $\pm 30^\circ$ Regular braid unit cell due to macroscopic tensile stress, $\sigma_{\xi\xi}$, in braiding direction compared to a experimentally determined curve.

the experimentally derived one, and, again, the OP model shows a to high strength as no local tow bending appears. The failure sequence highly resembles that of the $\pm 45^\circ$ braid, but this time also plasticity appears as loading in a direction, which is not an axis of orthotropy, induces shearing of the UC.

The third considered loading situation represents a uniaxial tensile load perpendicular to the braiding direction. Again, this loading state does not lead to local warping, thus, only a free single layer simulation is conducted. Figure 4.32 shows the predicted effective response in terms of linearized strains and engineering stresses compared with an experimentally determined result. As been clearly visible, the responses are significantly different. The initial stiffness still matches but starting at about 5 MPa the two responses deviate from each other. The UC gets to compliant and fails at about 50% of the experimental stress and strain. This pronounced difference can be explained by the perfect interface assumption in conjunction with touching tows applied within the shell element based modeling approach. The $\pm 30^\circ$ braid loaded perpendicular to the braiding direction tends to reorient the tow with respect to the loading direction. In the present model this scissoring can only be represented by shear deformation of the tows. In reality, however, the interfaces may break or

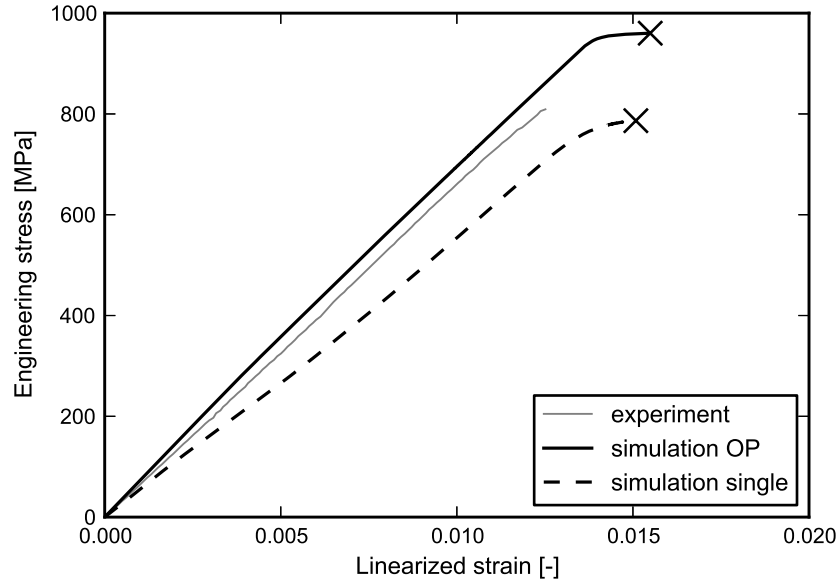


Figure 4.31: Predicted homogenized response of the $\pm 30^\circ$ Regular braid unit cell due to macroscopic tensile stress, $\sigma_{\xi\xi}$, in x , i.e. a tow direction, compared to a respective experimentally determined curve.

intermediate matrix areas may deform plastically. Thus, the model is locally too stiff and consequentially globally too compliant. The predicted failure mode is attributed to matrix dominated failure in transverse direction whereas experiments show a shear-off of the tows, see [19]. To cope with this problem degradable interfaces within the UC could be incorporated.

4.5.5 Nonlinear simulation of a $\pm 60^\circ$ single layer braid

The final consideration is the response of a $\pm 60^\circ$ braid with respect to uniaxial tensile loading in braiding direction. The investigated geometry is based on micrograph measurements conducted by the cooperation partner LCC using samples provided by PCCL. The real braid features an average tow centerline spacing which is about 10% smaller than the average tow width, hence some adaptation was necessary. The resulting tow geometry is listed in Tab. B.1 denoted as *Braid-60*. The theoretical total fiber volume fraction resembles the value of the *Braid-30* braid, thus the same material system featuring a tow fiber volume fraction of 88% is applied. The UC is

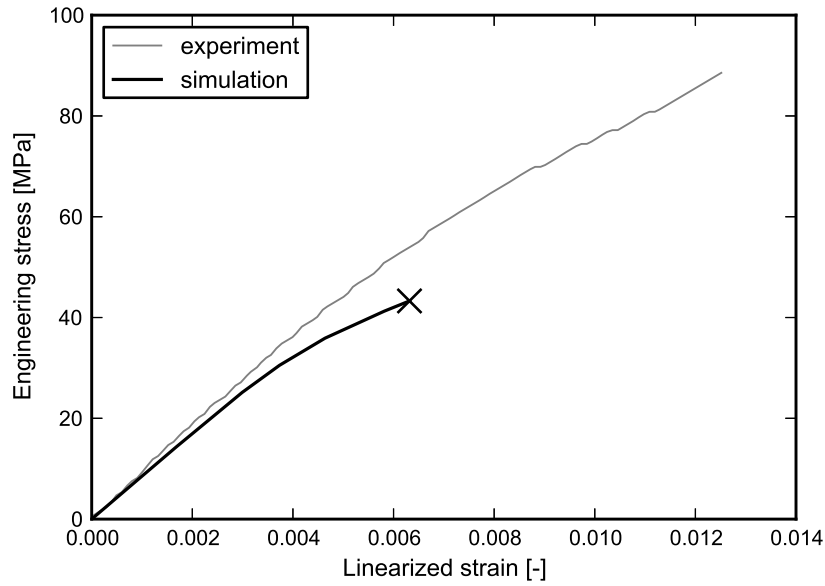


Figure 4.32: Predicted homogenized response of the $\pm 30^\circ$ Regular braid unit cell due to macroscopic tensile stress, $\sigma_{\eta\eta}$, perpendicular to the braiding direction compared to a respective experimentally determined curve.

set-up following the lenticular based approach with similar characteristics as defined before.

Figure 4.33 shows the predicted nonlinear response of the UC in terms of engineering stresses and linearized strains compared with some experimentally determined results. The latter are provided by a cooperation partner PCCL and are based on 4 layer specimens. As the present investigation resembles the $\pm 30^\circ$ braid loaded perpendicular to the braiding direction cf. 4.5.2, a similar response is expected. Comparing the last two figures reveals that indeed a similar trend can be found. The predicted initial stiffness is in a very good agreement with the experiments but at elevated strains the predicted response gets to compliant. This behavior can be explained in same way as for the $\pm 30^\circ$ braid. The difference between the last two figures can be explained to the better part by the different geometry dimension applied.

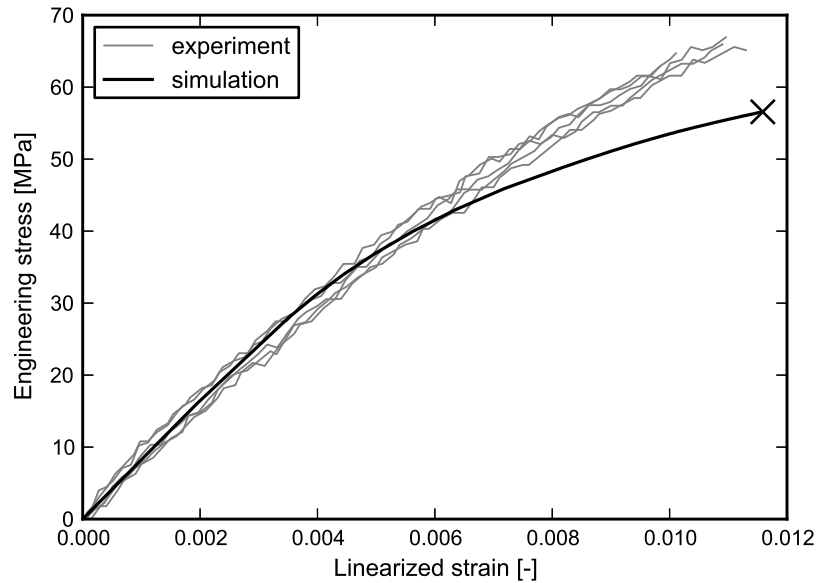


Figure 4.33: Predicted homogenized response of the $\pm 60^\circ$ Regular braid unit cell due to macroscopic tensile stress, $\sigma_{\xi\xi}$, in braiding direction compared to respective experimentally determined curves.

4.6 Conclusion

The shell element based unit cells of biaxial braided composites are shown to be able to accurately represent the stiffness and stress fields of comparable continuum element based cells. At the same time, the required simulation times and hardware specifications is significantly lowered. This is true for both, the rectangular cross section based and lenticular cross section based approaches. This performance gain allows for the simulation of explicitly modeled multilayer textiles as well as nonlinear simulations of the degradation and failure of respective braids. A comparison with experimental results reveal the good agreement with respect to stiffness and failure load predictions. In this context, the influence of the boundary conditions and statistical variations have to be pointed out. However, as shown for the last two simulations the proposed assumptions of perfect interfaces between two touching tows alleviates the local flexibility at higher loads and the resulting response becomes to compliant. Hence, for load cases leading to pronounced scissoring degradable interfaces might become necessary.

The proposed simulation strategy allows to numerically characterize braided and woven textiles at the mesoscale. To use the derived nonlinear material behavior during the design process of macroscopic parts additional measures are necessary as will be proposed next.

Chapter 5

Energy dissipation monitoring concept

The numerical material characterization conducted so far is limited to mesoscale considerations. However, the aspired application, i.e. design and evaluation of textile parts and structures, resides on the macroscale. A direct mapping of the mesoscopic results to the macroscale is only possible for some particular properties like the homogenized engineering constants and some failure measures. This implies that the nonlinear nature of the investigated braids cannot be accounted for, directly. To cope with this problem, a simulation methodology is proposed which combines linear elastic analyses of large scale laminated composite structures and nonlinear unit cell predictions.

The concept was published in [46] and [48]. Part of this work was carried out in the course of the master thesis of Meindlhumer [90] (load state distribution, radial stress computations) and Schwab [119] (matlab scripts, radial strain computations).

5.1 Background

In industry, a common approach to deal with laminated composites at the macroscale is using apparent or effective linear elastic properties of the plies or laminates (applying lamination theory) in combination with empirical or phenomenological based FPF criteria. These criteria use the acting stresses and strains, respectively, see

e.g. [67, 109], to reveal the loading state which is supposed to induce the “first” failure at ply level. Implicitly, they assume linear elastic material behavior. They do not account for any material degradation and cannot give any information on what is happening after this first ply failure. Moreover, in real composite parts, occurrence of first ply failure does not necessarily lead to the ultimate failure of the whole structure, it merely initiates nonlinear mechanisms within the composite. Clearly it would be of interest to obtain more information about the characteristics of the response beyond the elastic limit, i.e. the FPF, such as whether there is hardening or softening and whether or not there is some “strength reserve”.

This information may be gained by conducting detailed nonlinear simulations accounting for different damage and failure modes, like material degradation, plasticity, delamination, etc. In combination with numerical solution schemes, e.g. FEM, moderately sized macroscale nonlinear analyses can be performed (at least to some extent), which also account for stress redistribution due to the nonlinear material behavior. Even though this approach is widespread in academic and research institutions, see e.g. [39, 51], the accompanying computational demands prevent its applicability for large scale structures in industrial practice. This restriction is especially true if textile layers are present within the laminate. The complex microstructure requires highly refined meshes further heightening the computational requirements. In most cases, detailed investigations of textile laminates are restricted to the nonlinear behavior at the mesoscale. Recently, some research groups have been working on computational homogenization techniques bridging the lengths scales by concurrent nonlinear simulations of unit cells and macroscale structures [53, 78]. However, these strategies are still restricted to research type problems due to their vast computational requirements.

The aim of the current chapter is to propose a methodology combining detailed nonlinear predictions and simple linear elastic large scale simulations without direct coupling. This way the predictive capabilities of the linear elastic simulations can be extended without influencing the performance of the large scale simulations at all. In this context a central question arises, namely, “what are appropriate quantities to assess the nonlinear effects of an anisotropic material?” A scalar quantity would be advantageous compared to the tensor valued stresses and strains and their nonlinear evolution. The von Mises equivalent stress, commonly used with isotropic metallic

materials, cannot be used due to the present anisotropy. Here, the dissipated energies associated with the individual nonlinear (but dissipative) mechanisms will be used. In the following the proposed methodology will be denoted as energy dissipation monitoring concept.

5.2 Energy based assessment of the nonlinear state – database set-up

The failure surfaces of fiber reinforced composites found in the literature are typically based on FPF criteria. These criteria use the stresses and strains, respectively, of the acting loading state to compute a scalar value which is interpreted as some risk or load factor. As FPF criteria are based on linear elasticity, these scalar measures cannot be used directly to assess the current material state within the nonlinear regime. However, such criteria are commonly used within continuum damage mechanics to predict damage onset. Such damage models typically provide additional information on the accompanying dissipated energy - a monotonic increasing quantity - readily available to assess the current loading state, see Fig. 5.1. The same idea can be applied to evaluate the loading state with respect to nonlinear plastic response based on the dissipated energy accumulated based on the applied plasticity models. This allows for a distinct interpretation of the nonlinear mechanisms, e.g. damage, plasticity, but also delamination, and lays the foundation for the proposed evaluation concept. The phenomena can be assessed individually and the sequence of their occurrence and the progression upon load increase results naturally. Moreover, the approach is not limited to particular geometries and energy quantities are straightforward to be extracted from FEM simulations.

For the present case of laminated textile composites, the proposed technique is applied at the mesoscale. With respect to the applied assumptions, namely effective nonlinear tow and matrix pockets behavior, this length scale predominantly defines the nonlinear response of such material systems. The local macroscopic loading state is considered as an effective mesoscopic loading state and applied using the master node concept. In order to be able to assess arbitrary macroscopic loading states in a decoupled way, the evolution data of the whole space of possible macroscopic local stress

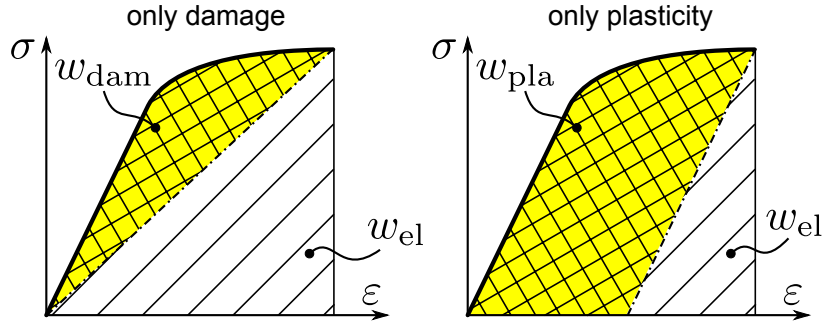


Figure 5.1: Uniaxial stress-strain curves of systems featuring either damage (left) or plasticity (right) as the only source of nonlinearity. The dissipated energy densities are crosshatched as well as shaded and the corresponding recoverable strain energy density is hatched.

and strain states including their load history has to be provided. This, obviously, would require an infinite number of simulations which is not possible. To overcome this limitations two fundamental assumption are applied, namely a discretization of the investigated mesoscopic effective loading space and radial, i.e. proportional, loading paths. The latter implies that the load history dependence is not considered, but is approximated by specific radial loading paths. These assumptions allow to represent the ‘whole’ space of possible loading states by a finite number of radial loading paths. Nevertheless, still a fair number of such load paths (effective stress and strain paths, respectively) are to be simulated at the mesoscale. The distribution of these mesoscopic loading paths, i.e. the discretization of the loading space, is such that the whole (plane) stress and strain space, respectively, is covered homogeneously with a sufficiently fine resolution. These nonlinear Finite Element simulations are conducted and the evolution of the dissipated energies is stored in a database to be used at a later stage. Consequently, no direct coupling between the macro- and mesoscale appears and the subsequent assessment can be conducted as a post-processing routine. To get a dimensionless measure the dissipated energies, W , are normalized using the current total energy of the system as

$$p_i(t) = \frac{W_i(t)}{W_{\text{tot}}(t)}, \quad i \in \text{pla, dam, } \dots, \quad (5.1)$$

with t denoting the (pseudo) simulation time which is associated with the load magnitude. The index i indicates the considered dissipation mode e.g. damage or plasticity.

The total energy, W_{tot} , is the sum of the dissipated energies associated with damage, W_{dam} and plasticity, W_{pla} , as well as the elastic strain energy. Note that “artificial” energy contributions associated with the numerical solution procedure, like energy dissipated by the viscous regularization technique, are not to be included in the total energy. Once any of the ratios defined by Eq. (5.1) becomes nonzero, onset of the particular mechanism is detected. As such, onset resembles the application of a classical FPF criterion in terms of the damage mechanism and of a yield criterion in terms of plasticity theory, respectively.

5.2.1 Radial stress vs. radial strain loading

The proposed approach is based on the stipulation that the stress components increase proportionally which load the unit cell – as well as at the considered location in the structure. In the linear regime this assumption holds true and for slightly nonlinear stress-strain responses it is approximated reasonably well. However, for pronounced nonlinear stress-strain behavior (which may set in at elevated loads) predictions may be expected to suffer from inaccuracy. Moreover, stress redistribution would occur at the macroscale model which cannot be accounted for by the present approach - the macroscopic simulations remain of linear type. To improve the predictive capabilities in such cases, the methodology is equivalently carried out under radial stress and strain loading of the unit cell. The strain paths are computed using the radial stress paths and the initial elasticity tensor. For the linear elastic case, stress and strain controlled simulations give the same results. However, beyond the elastic limit the responses will start to deviate from each other. Since stresses, as well as their strain equivalents, are based on linear elastic considerations, one cannot tell which loading scenario is the more realistic one. However, they are expected to state some upper and lower estimates on the possible behavior. Additionally, mildly deviating responses indicate that the assumptions are met in an approximate way. To visualize these estimates a simple one dimensional example is used. Figure 5.2 shows a stress-strain curve and corresponding evolutions of the energy ratios. In this particular case, a 1D problem, the stress and strain controlled loading leads to exactly the same results (black solid line). The plot further shows the evolution of dissipated energies associated with damage (solid, gray) and plasticity (dashed, gray). The mapping of the linear macroscale results to the nonlinear mesoscopic ones follows the underlying

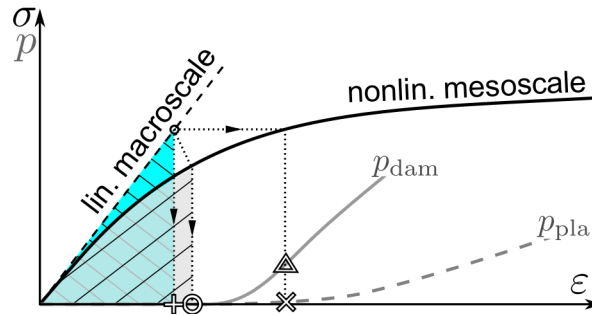


Figure 5.2: Sketch of a nonlinear stress-strain curve in a one dimensional example and corresponding evolutions of the dissipated energy ratios. The triangle and cross indicate the energy ratio based on (radial) stress evaluation, the plus denotes the (radial) strain one. The circle corresponds to the equal energy strategy.

loading strategies. Stress controlled load cases are evaluated at equal stress level (triangle and cross symbols) whereas strain controlled cases issue an equal strain assumption (plus symbol). Here, the plus symbol represent both values (damage and plasticity) for the strain controlled case as these are coincident at the considered load level. As already stated the resulting energy ratios can be treated as some upper and lower estimates.

A third mapping technique assumes equal total energy at both length scale (hatched and shaded areas). This result (circle) typically resides between the former two and can be used to qualitatively assess the difference between radial stress and radial strain based loading. It may be noted, that the corresponding dissipated energy levels can be used as an additional predictor for the current nonlinear state, however, the respective value is not to preferred against other values within the range of the computed upper and lower estimates. Again, for the considered load the two points for the damage and plasticity ratio coincide and only a single symbol is used.

For locations identified as critical by the proposed approach or showing doubtful results, a sub-modeling technique could be applied.

5.2.2 Additional remarks

Since some hundred nonlinear simulations are necessary to compute reasonable refined energy dissipation datasets, an efficient modeling and simulation strategy is

essential. Here, the number and the distribution of the precomputed mesoscopic loading paths can be optimized as well. The results of previous or preliminary computations may be used to incorporate non-uniform distributions better suited for the currently investigated mesostructure. Note, that the distribution of the load paths may affect the accuracy of the predicted results, cf. Appendix C.

Once determined, the datasets can be used for arbitrary large structures comprising the same textile ply. Of course, different material systems dictate different datasets. Interpolation between different datasets may be reasonable to minimize the number of required precomputed material system. Of course, the difference between such datasets has to be within a reasonable range, e.g. small variation of a constituents' dimension.

In case of laminates with reasonable thin layers, the proposed approach featuring a three dimensional loading space (plane stress and strain space, respectively) is sufficiently accurate. This implies that occurring macroscopic bending and twisting loads are translated into respective layer-wise membrane normal and shear loads, cf. classical lamination theory. If thick layers are considered, i.e. high gradients in thickness direction might appear, the energy dissipation monitoring concept can be enriched to cope with mesoscopic bending and twisting. Internally, this leads to a six dimensional loading space and therefore, more mesoscopic nonlinear simulations are necessary to accurately capture the effective loading space. For both types (thin and thick layers), single ply unit cells are sufficient for most cases. Nevertheless, whole-laminate unit cells can be used to include further damage modes like delamination between the individual layers. As bending and twisting might be important, a six dimensional approach is highly recommended for whole-laminate unit cells. Of course, such whole laminate approaches require substantially more computational demands and therefore, may be restricted to simple unit cell geometries.

Finally, it may be noted, that based on the derived total strain energy density data, a numerically based constitutive law could be constructed using hyperelastic assumptions like

$$\boldsymbol{\sigma} = \frac{\partial w_{\text{tot}}}{\partial \boldsymbol{\varepsilon}} . \quad (5.2)$$

However, as only radial path data is available, this constitutive model would only permit respective radial loading histories. Thus, once reaching the nonlinear state any

stress redistribution appearing immediately leads to a violation of the assumptions. Nevertheless, Eq. (5.2) gives a physical justification of the proposed approach.

5.3 Evaluation strategies – database usage

With the “energy dissipation evolution data” and corresponding stress and strain paths stored in a database any subsequent evaluation can be realised in a pure post-processing way. Here, two possible evaluation strategies will be introduced, namely “energy dissipation envelopes” visualizing the evolution of the incorporated nonlinear mechanisms of the microstructural material’s UC, and advanced post-processing of macroscopic structures. The former envelopes are drawn in stress and strain space, respectively, corresponding to various dissipation energy levels, e.g. for the initiation of the individual mechanisms and for selected relative energies. This way, an overview is given over damage evolution gradient, “strength reserve”, sensitivity to overloads, directional sensitivity, etc. Meaningful values of the plotted dissipated energy levels can be defined from simulations of selected load cases and, preferably, accompanying experiments. The initiation envelopes computed this way can be considered as numerically determined FPF and yield criteria, respectively.

The second proposed strategy aims at the application of the derived data to linear elastic macroscopic simulations. Here, the energy dissipation data is utilized in an automated way for which the predicted stresses at a certain location of the macroscopic structure is used as input. At this stage, the initiation envelopes defined before can be used as FPF and yield criteria respectively, to assess a prevailing stress state with respect to its severity. To this end, the intersection points between the envelopes and the loading path are computed using a ray tracing algorithm [93] and the corresponding safety and reserve factors are extracted. The stress state at locations identified as being critical (reserve factor > 1) is further evaluated as follows. First, the corresponding strain state and elastic strain energy is computed based on the homogenized elastic properties of the composite. This way the macroscopic local loading state is elastically defined. The subsequent evaluation is equally carried out based on the acting stress and strain state using the radial stress and radial strain based datasets, respectively. For the sake of brevity only the stress based steps are discussed here. The macroscopic local stress state is considered as a point on a meso-

Checking all locations while applying the energy dissipation evolution data gives information on critical spots and activated nonlinear mechanisms as well as their evolution and progress.

As the sensitivity of the critical loading state is not obvious, the question may rise if another structural location gets more critical during load increase. This can be answered by assessing the predicted macroscopic stress fields not only using the already proposed numerical FPF criterion, but using additional “post-initiation” data points associated with a certain amount of dissipated energy. The latter immediately indicates whether the critical point remains the same, or other locations have to be assessed as well. Of course, one has to be aware that nonlinear effects like stress redistribution, are not included in the macroscale simulations, hence the considerations should remain in a mild nonlinear regime or being interpreted with caution.

5.4 Application example

To demonstrate the usage of the energy dissipation monitoring concept an airplane engine nacelle structure built from a woven laminate will be used. The first step is to compute the energy dissipation evolution dataset for the applied textile ply at the mesoscale. To this end, a unit cell is set up within the FEM framework using the shell element modeling approach proposed in Sec. 3.3. The second step deals with the simulation of the macroscopic structure and the application of the energy dissipation evolution data.

All FEM simulations are carried out using the commercial solver Abaqus/Standard v6.12 (*Dassault Systèmes Simulia Corp., Providence, RI, USA*), the post-processing is realized by a user defined subroutine applying the energy dissipation data and a Matlab 2013a script (*The MathWorks, Inc., Natick, Massachusetts, United States*) to derive the respective evolutions. The communication is handled by several accompanying python scripts.

5.4.1 Mesoscopic unit cell: Twill weave

The material system under consideration is a carbon/epoxy 2/2 Twill weave. The investigated (incorporated) nonlinear mechanisms are damage of the tows and plasticity of the unreinforced matrix pockets. Since the computation of energy dissipation envelopes requires some 200 nonlinear computations a shell element based unit cell approach is applied. All these simulations rely on a single layer unit cell.

Geometry and mesh. The geometry of the considered weave is chosen to feature tows with a rectangular cross section and a piecewise linear ondulation path as defined in Sec. 4.1. The corresponding geometrical data is given in App. B Tab. B.1 denoted as *Rect-1*.

The reference surfaces of the shell elements are meshed by 4-noded shell elements with linear interpolation functions featuring a typical element size of $1/14^{\text{th}}$ of the tow width. In thickness direction a Simpson scheme with five section points is used. The individual shell elements are tied appropriately, representing perfect interfaces, i.e. no delamination is permitted. At the unit cell lateral boundaries the nodes are coupled appropriately to achieve plane periodic boundary conditions.

Applied material models. To incorporate the aspired damage and plasticity mechanisms the tows are represented featuring a transversely isotropic elasto-brittle behavior. The applied FRP damage model is readily available in Abaqus/Standard v6.12 [64] and is based on a Hashin criterion to assess damage initiation [63] accompanied by linear strain softening for both fiber and matrix dominated phenomena, see Sec. 2.2.2. This model does not account for possible plastic deformation, hence, strictly speaking, loading situations which lead to pronounced plastic responses in the tows should be avoided. The studied woven laminates feature plies in 0 and 45 degree direction, thus the latter criteria is met. The elements of the unreinforced matrix pockets are equipped with an elastic-perfect plastic isotropic material featuring a Drucker-Prager type plasticity model. All required material data can be found in Tab. A.3.

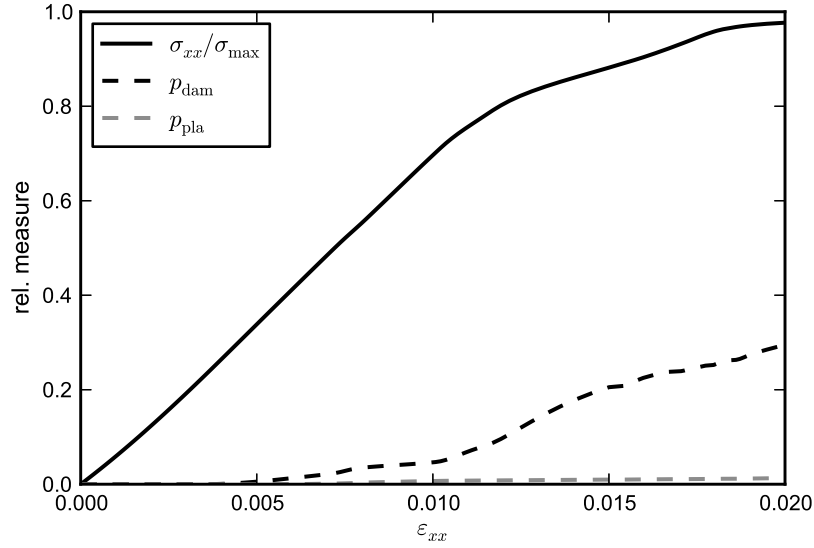


Figure 5.4: Normalized stress vs. strain plot of a nonlinear meso-scale simulation with $\boldsymbol{\sigma}^{\text{appl}} = [600, 0, 0]$ MPa including the corresponding energy ratio evolutions.

5.4.2 Energy Dissipation envelopes – mesoscopic results

Using the master node concept, Sec. 3.1.2, the required effective radial loading paths are applied to the unit cell. As an effective orthotropic material symmetry is expected, only one fourth of the investigated stress and strain space respectively, has to be considered. In total 81 different plane stress paths, and 81 plane strain paths are simulated. Using the strategy proposed in Sec. 5.2, the evolution of the individual energy ratios is extracted for each radial load path and stored in a database. Figure 5.4 shows the normalized response of an example simulation with $\boldsymbol{\sigma}^{\text{appl}} = [600, 0, 0]$ MPa indicating the individual energy ratios.

Based on this precomputed database, the initiation of the nonlinear mechanisms, can be assessed. The corresponding FPF and yield envelopes can be directly obtained by evaluation of the energy dissipation evolution data for an energy ratio slightly bigger than zero. Figure 5.5 shows the obtained surfaces for a ratio of 0.00001 in the plane stress space. These surfaces are based on the radial stress simulation data, however, as the FPF denote the elastic limit, the radial strain based surfaces coincide. Of course, this “identity” is only valid for the initiation surfaces. Such FPF surfaces can be directly used at macroscale simulations to assess the currently acting stress

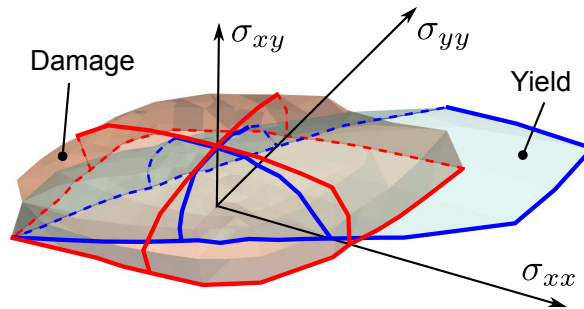


Figure 5.5: Stress envelopes of a 2/2 Twill weave showing damage (dark shaded) and yield (light shaded) initiation surfaces due to radial stress loading.

and strain state, respectively. Moreover, a visualization in the mesoscopic effective stress and strain space, respectively, helps to understand directional sensitivity of the considered meso-structure, see Fig. 5.5.

To obtain these failure surfaces, linear elastic simulations would have been sufficient, however, the main focus is laid on the nonlinear regime. To this end, additional surfaces of equal dissipated energy ratio can be evaluated to highlight the load factor sensitivity of the particular loading direction, i.e. what's happening if the load is increased proportionally. Figure 5.6 gives the evolution of the energy dissipation envelopes with respect to ply damage for radial stress loading in the $\sigma_{xx} - \sigma_{yy}$ sub-space. It is clearly visible that upon damage initiation compressive stresses are much more severe in terms of damage progression than tensile stresses. Similar to this, Fig. 5.7 shows the energy dissipation envelopes with respect to matrix plasticity for different energy ratios based on radial stress loading. Again, the compressive loading regime can be considered as more critical with respect to load increase. Note that due to the applied material models, plasticity only appears in the rather small areas of unreinforced matrix pockets. The fiber bundles – shown to possess plastic behavior [133] – are assumed to remain elastic throughout the whole simulation and, therefore, the amount of dissipated plastic energy may be under-predicted here. To cope with this problem, more advanced ply material models have to be used, cf. [46].

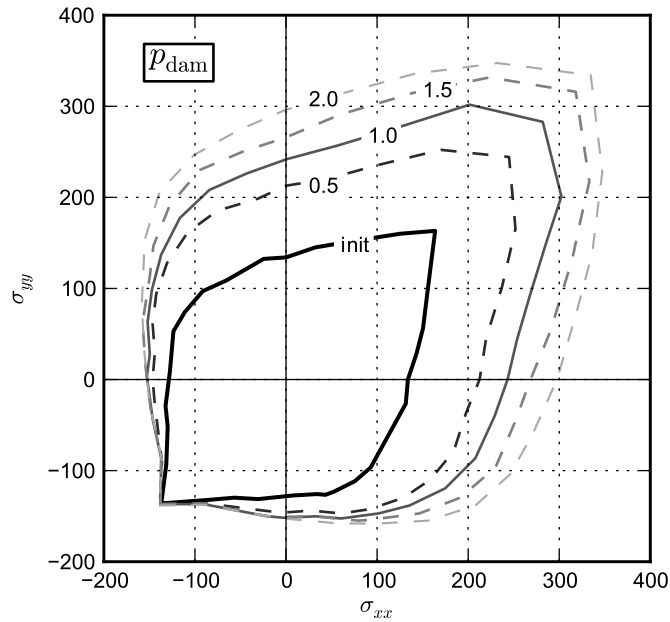


Figure 5.6: Energy dissipation envelope in the $\sigma_{xx} - \sigma_{yy}$ sub-space indicating the initiation (init) and different levels (in percent) of dissipated energy ratios associated with ply damage (radial stress loading).

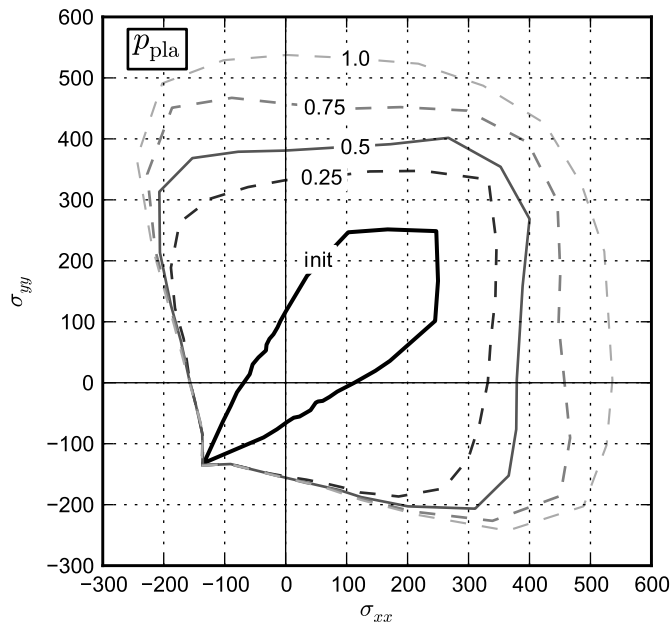


Figure 5.7: Energy dissipation envelope in the $\sigma_{xx} - \sigma_{yy}$ sub-space indicating the initiation (init) different levels (in percent) of dissipated energy ratios associated with matrix plasticity (radial stress loading).

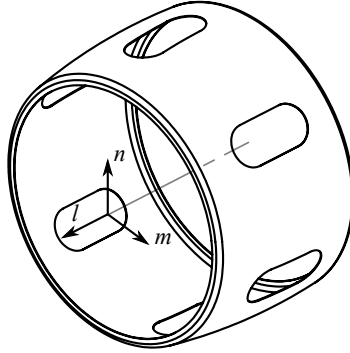


Figure 5.8: Isometric view of the macroscopic nacelle structure.

5.4.3 Macroscale structure: nacelle part

The considered macroscopic structure represents a generic part of some nacelle which might be part of an aircraft engine. It is considered to be subjected to some circumferential drag load due to air flow. A linear elastic simulation is conducted and the appearing stresses and strains are assessed using the proposed energy dissipation monitoring concept.

Geometry and mesh. The nacelle resembles a cylindrical shell structure with an outer diameter of about 2000 mm, a height of around 1000 mm and six slotted holes are distributed around the lateral surface. Figure 5.8 shows an isometric view of the nacelle. The whole structure is made of a 13 layer carbon/epoxy 2/2 Twill weave laminate featuring the same textile architecture as defined in the previous section. A stacking sequence of $[0_3/45_2/\bar{0}_3]_S$ is applied. Here, 0 indicates that the direction of the warp yarns corresponds to the axial direction of the structure.

Due to the symmetry of the structure, the loading as well as the material, only a sixth of the whole part has to be modeled. This sector is meshed using quadratic shell elements with reduced integration and a layered shell formulation. In thickness direction three section points per layer are used.

Applied material model. The required effective material data for the individual layers is computed based on a unit cell characterization of the chosen material system. As the initial stiffness of a single layer Weave-type textile is significantly lower than the stiffness of a laminate, see e.g. Sec. 4.4, two double layer versions of the unit cell,

Table 5.1: Effective single ply material data of the 2/2 Twill weave (structural scale); the transverse shear moduli (*) are estimated values.

$E_x = E_y$	ν_{xy}	G_{xy}	$G_{xz}^* = G_{yz}^*$
47 GPa	0.1	2.9 GPa	4.6 GPa

in-phase and out-of-phase stacked, are used to compute the effective linear elastic properties. The influence of adjacent layers is represented by taking the average of in-phase and out-of-phase stacking results. Table 5.1 lists the resulting engineering constants to be used with the large scale simulations.

Loading conditions. The macroscopic boundary conditions represent an artificial load case of a variable pressure. The two end sections of the nacelle are constraint axially by neighboring parts and the rear part of the tapered surface is subjected to an axisymmetric pressure load featuring a cosine based distribution as sketched in Fig. 5.9. The average pull per mm circumference is assumed to be 45 MPa/mm . Note that this value is not based on aerodynamic considerations.

5.4.4 Demonstrator evaluation – macroscopic results

To apply the proposed concept at the macroscale, a user subroutine capable of employing the previously computed data is implemented in Abaqus. With this tool, the energy dissipation envelopes can be used during post-processing like conventional FPF criteria indicating the reserve factor or safety factor with respect to the current

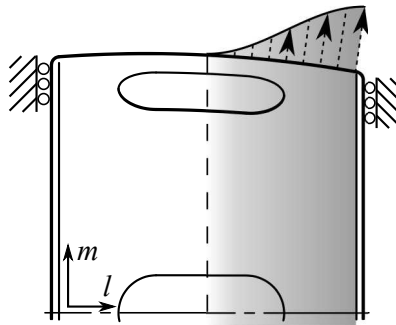


Figure 5.9: Sketch of the applied boundary conditions on the nacelle structure.

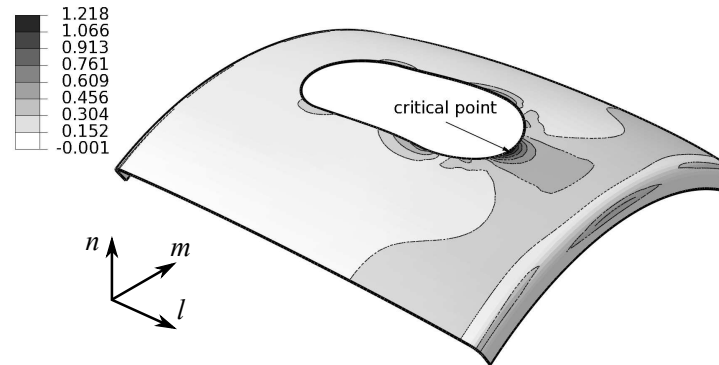


Figure 5.10: Contour plot of the predicted reserve factor at the inner shell surface (corresponds to the critical location) against damage initiation of the nacelle sector.

loading step. Figure 5.10 shows a contour plot of the reserve factor against FPF (i.e. damage onset) of the nacelle sector subjected to the prescribed pull load. By means of this figure the inner surface at the axial quadrant of the slotted hole is identified to be the most critical location in terms of ply damage. At this location the inner layer of the laminate gets loaded in tension in tow direction, and, as shown in Sec. 4.2, at the corresponding perpendicular tows damage starts to initiate. A similar evaluation giving the reserve factor with respect to yield initiation can be conducted as well, see Fig. 5.11. To evaluate the severity and sensitivity of this particular macroscopic critical location, the local stress state is used to extract the evolution of the individual damage and failure modes stored in the energy dissipation evolution database as described in Sec. 5.3.

Figure 5.12 shows the predicted evolution of the dissipated energy ratio associated with ply damage for the critical location with respect to the load factor. The black solid line represents the response for a radial stress based loading, whereas the gray solid line shows the corresponding radial strain based loading. The dashed lines denote the equal energy evaluation strategies with respect to radial stress and strain loading. Additionally, the load factor leading to damage initiation (dam init) is marked with a circle and the load factor associated with the first occurrence of a non-linear mechanism (NL init) is indicated with a cross. Note that the latter is defined as the minimum of the initiation load factors associated with damage and plasticity. The good agreement of the two equal energy lines indicate that the mesoscopic re-

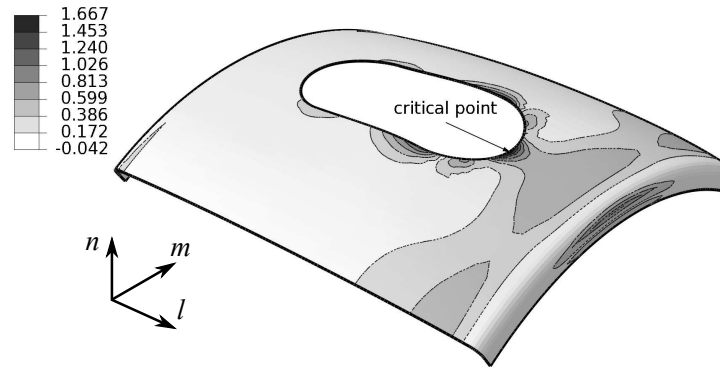


Figure 5.11: Contour plot of the predicted reserve factor at the inner shell surface (corresponds to the critical location) against yield initiation of the nacelle sector.

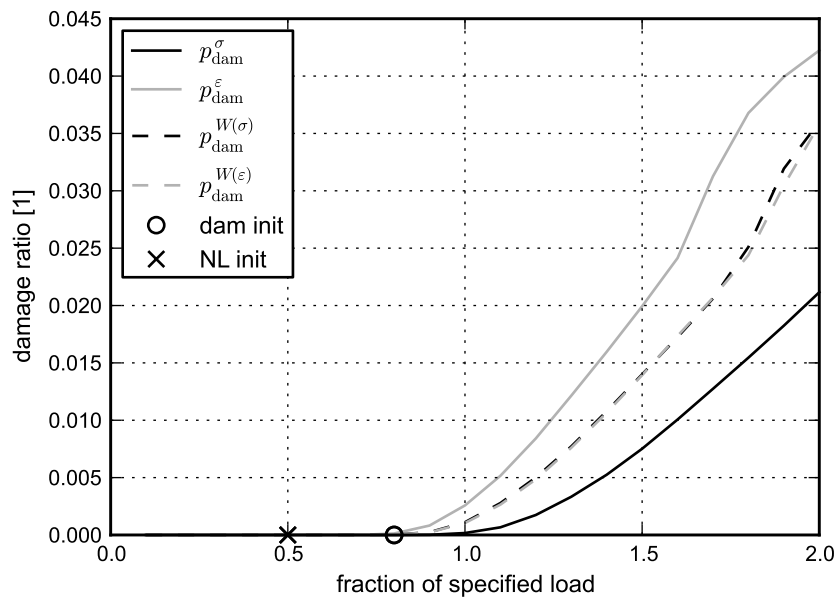


Figure 5.12: Predicted evolution of the dissipated energy ratios associated with ply damage due to radial stress and strain loading, respectively, at the critical location.

sponse of the unit cell subjected to radial stress based loading strongly resembles the response of the corresponding radial strain based loading for the particular loading path. Figure 5.13 gives the same type of information for the dissipated energy ratios associated with matrix plasticity.

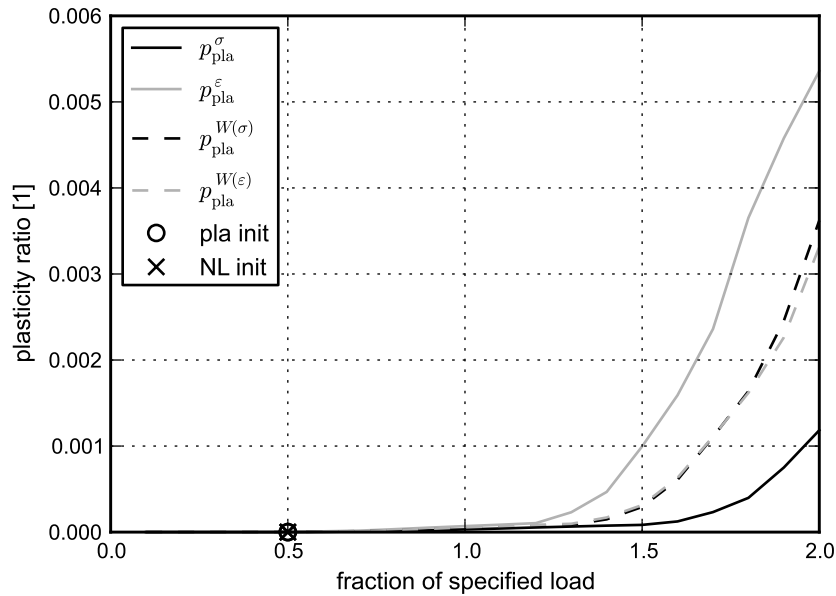


Figure 5.13: Predicted evolution of the dissipated energy ratios associated with ply plasticity due to radial stress and strain loading, respectively, at the critical location.

Following Fig. 5.12, the applied macroscopic loading state results in local stresses which are beyond the first ply failure of the textile composite. However, the amount of dissipated energy at load factor one and the rather moderate increase of the progression curve suggest, that the laminate might sustain further load increase. Until a load factor of two, the energy dissipated due to damage is below 4.5% and 2%, respectively. Note that the more critical state, the radial strain based curve (gray line), only represents some upper estimate.

The development of the dissipated energy associated with matrix pocket plasticity (Fig. 5.13) reveals that the yield criteria has been met at about 50% of the particular loading conditions. The energy evolution following this initiation shows that the associated nonlinearity plays a negligible role until load factors beyond one. At elevated load factors some notable energy dissipation occurs indication plastic strain accumulation. If the energy fractions are compared quantitatively with the ones attributed to tow damage, matrix pocket plasticity may be considered as less dominant for the acting loading state.

5.5 Conclusion on energy dissipation

A simulation methodology is proposed combining linear elastic analysis of large scale laminated composite structures and detailed nonlinear unit cell predictions to account for local nonlinear material behavior at the ply level. In a two-step procedure nonlinear unit cell simulations are conducted first and the dissipated energies of the individual damage, plasticity and failure mechanisms are computed. The latter are considered as a measure of unit cell exertion. In a second step this data can be used to draw “energy dissipation envelopes” in stress and strain space as well as to perform post-processing on linear large scale structural analyses. Based on the concept of energy dissipation monitoring, the macroscopic material point exertion is assessed with respect the local damage and failure phenomena at the unit cell level. The approach is not limited to textile composites but can be used with any type of multiscale material to enable the consideration of complex nonlinear behavior in a very efficient manner.

Chapter 6

Summary

The nonlinear simulation of the mechanical behavior of composite structures comprising braided or woven plies is a demanding topic. The complex architecture combined with the complex constituents' behavior requires sophisticated methods to accurately predict their response. In the framework of the FEM the most common approach to deal with the behavior of textile materials is to apply a homogenisation technique relying on continuum element based unit cells. This, however, results in vast computational requirements and prevents their economic application in an assessment of the nonlinear behavior. Moreover, the application of the computed results at macroscale structures is not well defined.

Motivated by this limitations, a shell element based modeling concept for braided and woven composites is developed, by which all constituents are represented using Finite elements of the shell type only. Applying common assumptions, like constant tow cross sections along the undulation path the strategy is defined for braids featuring rectangular cross sections as well as lenticular based cross sections. Braided unit cells featuring braiding angles different than 45° are realized using strain-free skewing of the initially orthogonal unit cell. All constituents are coupled appropriately and are equipped with plane stress material models. The latter may incorporate tow damage and plasticity as well as matrix pocket plasticity. The shell element based unit cells feature less DOFs than comparable continuum element based ones and consequently a substantial performance gain is achieved. A verification and comparison study shows that the proposed strategy obtains accurate predictions in terms of stiffness as well as strength measures and reduces the computational demands in terms

of simulation time as well as hardware requirements at the same time. The accomplished computational efficiency allows for the simulation of multilayer composites by modeling of the individual layers. This way, interlaminar delamination phenomena appearing between the plies can be simulated as well. Moreover, nonlinear simulations taking into account the degradation of and residual strain accumulation in the constituents can be conducted efficiently. Respective analyses are carried out for different braids and a comparison with experimental results reveal a good agreement.

To allow for the application of these mesoscopic results, a concept is proposed based on energy dissipation considerations. To this end, the unit cell is subjected to distinct effective loading paths and the evolution of individual energies is monitored and stored in a database. This data is subsequently used to assess the sensitivity of the nonlinearities with respect to load factor and direction variation. Moreover, the data is used in conjunction with macroscale, linear elastic simulations to post-process the computed macroscopic stresses. Critical points are identified and the occurring local stress states are used to derive the evolution of the individual energy dissipations based on proportional loading assumptions. The concept relies on a precomputed database, hence it proves itself as an effective tool to assess large scale structural parts comprising complex inhomogeneous materials taking into account material induced nonlinearities.

Finally, it shall be said, that the proposed modeling approach in combination with the energy dissipation concept allows for the efficient simulation of large scale structures comprising textile composites in the presence of material induced nonlinearities.

Appendix A

Material parameters

Throughout this thesis various composites are investigated. The corresponding material systems are listed in the following chapter.

Table A.1: Tow and matrix pockets material data for the Epoxy/IM6 material system, based on [87].

Tows (70% fiber volume fraction)					Matrix	
E_1	$E_2 = E_3$	$\nu_{12} = \nu_{13}$	ν_{23}	$G_{12} = G_{13}$	E_{Matrix}	ν_{Matrix}
190 GPa	11 GPa	0.35	0.44	5.9 GPa	4 GPa	0.36

Table A.2: Tow, matrix pockets and interface data for the T300-920 material system, based on [33].

Tows (70% fiber volume fraction)					Matrix	
E_1	$E_2 = E_3$	$\nu_{12} = \nu_{13}$	ν_{23}	$G_{12} = G_{13}$	E_{Matrix}	ν_{Matrix}
160.20 GPa	9.82 GPa	0.31	0.29	4.68 GPa	3.76 GPa	0.39
Cohesive element properties						
K_n, K_t, K_s	τ_n	$\tau_s = \tau_t$	\mathcal{G}_{Ic}	$\mathcal{G}_{\text{IIc}} = \mathcal{G}_{\text{IIIc}}$	p_{BK}	
10^8 MPa/m	50 MPa	80 MPa	210 J/m ²	800 J/m ²	1.5	

Table A.3: Essential material data for the tows, matrix pockets and cohesive interfaces of the Cycom®977/HTS40 material system, based on [27, 38, 141].

Tows (60 % fiber volume fraction)					
E_1	$E_2 = E_3$	$\nu_{12} = \nu_{13}$	ν_{23}	$G_{12} = G_{13}$	
146 GPa	9 GPa	0.34	0.61	4.27 GPa	
R_{11}^t	R_{11}^c	R_{22}^t	R_{22}^c	R_{12}	
2100 MPa	1407 MPa	82 MPa	249 MPa	110 MPa	
$\mathcal{G}_{(ft)}$	$\mathcal{G}_{(tc)}$	$\mathcal{G}_{(mt)}$	$\mathcal{G}_{(mc)}$	$\mathcal{G}_{(ps)}$	
89800 J/m ²	78300 J/m ²	200 J/m ²	800 J/m ²	1000 J/m ²	
Matrix pockets					
E_{Matrix}	ν_{Matrix}	σ_y^t	Friction angle	Dilation angle	K
3.52 GPa	0.39	81.4 MPa	25°	25°	1
Cohesive interface properties					
K_n, K_t, K_s	τ_n	$\tau_s = \tau_t$	\mathcal{G}_{Ic}	$\mathcal{G}_{IIc} = \mathcal{G}_{IIIc}$	p_{BK}
10 ⁹ MPa/m	60 MPa	110 MPa	133 J/m ²	460 J/m ²	2

Table A.4: Essential material data for the tows and matrix pockets of the RTM6/HTS40 material system scaled to 78% fiber volume fraction, original data based on [114, 115].

Tows (78 % fiber volume fraction)					
E_1	$E_2 = E_3$	$\nu_{12} = \nu_{13}$	ν_{23}	$G_{12} = G_{13}$	
179.9 GPa	10.6 GPa	0.24	0.68	4.97 GPa	
R_{11}^t	R_{11}^c	R_{22}^t	R_{22}^c	R_{12}	
2631 MPa	1240 MPa	33 MPa	175 MPa	76.4 MPa	
$\mathcal{G}_{(ft)}$	$\mathcal{G}_{(tc)}$	$\mathcal{G}_{(mt)}$	$\mathcal{G}_{(mc)}$	$\mathcal{G}_{(ps)}$	
89800 J/m ²	78300 J/m ²	200 J/m ²	800 J/m ²	1000 J/m ²	
Matrix pockets					
E_{Matrix}	ν_{Matrix}	σ_y^t	Friction angle	Dilation angle	K
2.89 GPa	0.38	75 MPa	25°	25°	1

Table A.5: Essential material data for the tows and matrix pockets of the RTM6/HTS40 material system scaled to 88% fiber volume fraction, original data based on [114, 115].

Tows (88 % fiber volume fraction)					
E_1	$E_2 = E_3$	$\nu_{12} = \nu_{13}$	ν_{23}	$G_{12} = G_{13}$	
203.2 GPa	11.99 GPa	0.22	0.68	5.61 GPa	
R_{11}^t	R_{11}^c	R_{22}^t	R_{22}^c	R_{12}	
2791 MPa	1400 MPa	33 MPa	175 MPa	76.4 MPa	
$\mathcal{G}_{(ft)}$	$\mathcal{G}_{(tc)}$	$\mathcal{G}_{(mt)}$	$\mathcal{G}_{(mc)}$	$\mathcal{G}_{(ps)}$	
89800 J/m ²	78300 J/m ²	200 J/m ²	800 J/m ²	1000 J/m ²	
Matrix pockets					
E_{Matrix}	ν_{Matrix}	σ_y^t	Friction angle	Dilation angle	K
2.89 GPa	0.38	75 MPa	25°	25°	1

Appendix B

Textile geometries

Based on the measurements of Marte [87] (*Rect-1*, *Lent-1*) and De Carvalho et al. [33] (*Lent-2*), Twill weaves with rectangular and lenticular, respectively, tow cross sections are designed using the dimensions (in mm) given in the table below. The total fiber volume fraction is given for a fiber volume fraction of the tows of 70%. Additionally, three types of braids geometries ($\pm 30^\circ$, $\pm 45^\circ$, $\pm 60^\circ$) based micrograph measurements conducted by the cooperation partner LCC are applied. The corresponding UC models featuring a lenticular tow cross section are defined as given below (*Braid- x*). Figure B.1 and Fig. B.2 display a sketch of the rectangular and lenticular, respectively, cross section based unit cell.

Table B.1: Geometric dimensions of the investigated textiles, all values are given in mm.

Id	Ref	w	t	w_c	t_c	p	l_{UC}	f_{vol}
Rectangular tow cross section (Fig. B.1)								
Rect-1	[87]	1.81	0.175	-	-	2.46	9.84	51.8%
Lenticular tow cross section (Fig. B.2)								
Lent-1	[87]	2.2	0.175	0.2	0.075	2.85	11.4	44.7%
Lent-2	[33]	1.58	0.15	0.23	0.0702	2.09	8.36	45.0%
Braid-30	-	2.749	0.311	0.19	0.042	2.968	11.87	47.7%
Braid-45	-	3.092	0.282	1.0	0.02	3.205	12.82	53.7%
Braid-60	-	2.424	0.366	0	0	2.47	9.87	46.2%

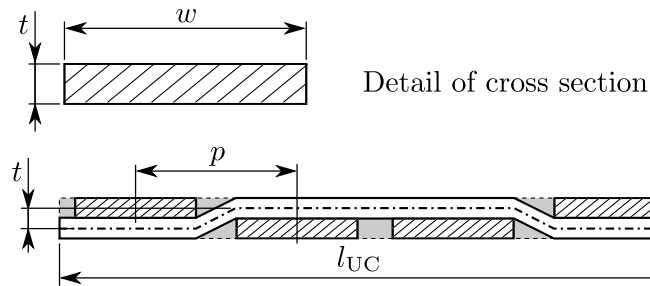


Figure B.1: Cross section of a generic 2/2 Twill Weave featuring rectangular tow cross sections (hatched). The dashed line represents the unit cell perimeter and the gray areas denote the matrix pockets.

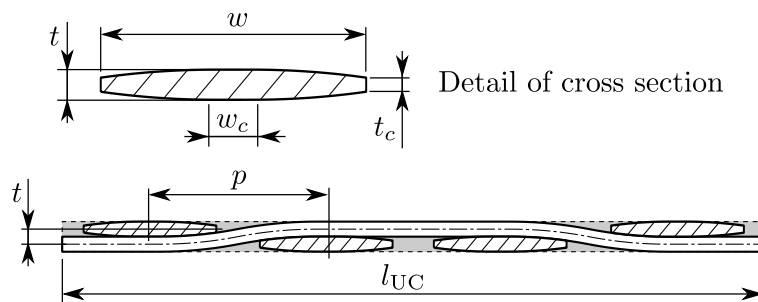


Figure B.2: Cross section of a generic 2/2 Twill Weave featuring lenticular based tow cross sections (hatched). The dashed line represents the unit cell perimeter and the gray areas denote the matrix pockets.

Appendix C

Load paths distribution

Common failure envelopes, like FPF criteria, are typically expressed as an implicit function with respect to the stress, and strain tensor, respectively, like $f(\boldsymbol{\sigma}) = 1$. Numerically computed envelopes, intrinsically get a similar implicit nature. A rather common way to extract an envelope of such an implicit function is to discretize the argument space, e.g. the plane stress space and solve the implicit equation at each sub-domain. This, however, results in a huge number of computations. Moreover, in the framework of incremental solution strategies, several intermediate solutions are created when aiming at a particular point in the arguments space. A more meaningful approach is to discretize the space by means of spherical coordinates and a fixed length. Such radial rays (actually load paths) start at the origin, i.e. the loading-free state. Depending on the aspired resolution, a fair number of radial load paths have to be computed. Moreover, the achieved accuracy also depends on the distribution of the paths. Without additional knowledge a homogeneous distribution will be a good choice. A possible strategy to derive respective directions is use evenly spaced points on a sphere. It may be noted that a sphere is beneficial due to implicitly constant loading rate (comparable influence of the viscous regularization scheme). There are several approaches to distribute points on a sphere (see e.g. [90]) like e.g. recursive definition based on platonic solids. In the present study a recursion based on an octaeder is used initially.

If the expected shape of the envelope is known beforehand, the distribution can be optimized. This optimization might be crucial to accurately capture specific feature of the envelope.

In case of (expected) strong anisotropic behavior, like plate or cigar shaped envelopes, evenly spaced points are clearly not the best choice. In such cases a pole or equator biased distribution can lead to significantly better predictions. A prominent example of such an anisotropic behavior is the Tsai-Wu failure surface [131]. Figure C.1 juxtaposes the load vector distribution for evenly spaced (258 points) and pole biased (306 points) cases. The resulting failure envelopes are given in Fig. C.2. It is immediately obvious that the pole biased based surface is a far better representation of the analytically defined Tsai-Wu surface than the evenly spaced based one. Nevertheless, for the common case of convex failure surfaces, the evenly spaced based surface is a conservative representation.

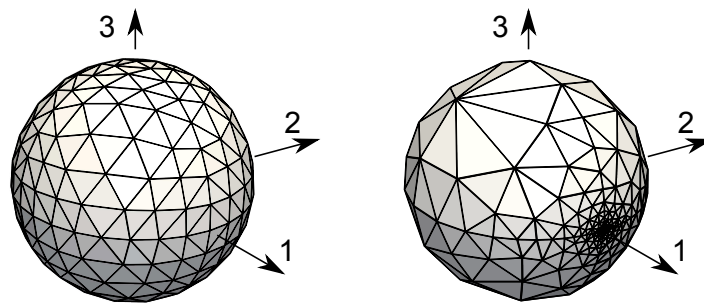


Figure C.1: Evenly spaced points (left) and pole biased points (right) on a virtual sphere in loading space.

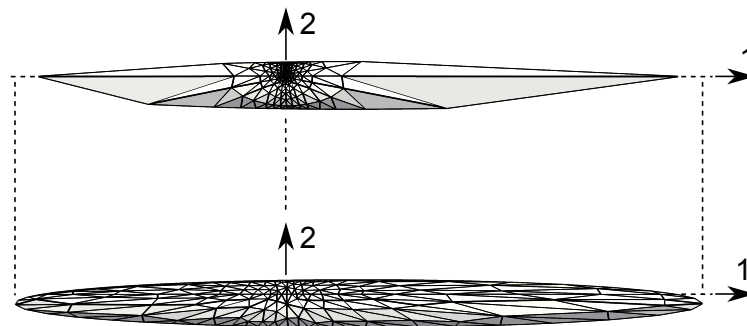


Figure C.2: Computed Tsai-Wu failure envelopes based on evenly spaced load paths (top) and pole biased load paths (bottom).

Bibliography

- [1] A. Adumitroaie and E. J. Barbero. Beyond plain weave fabrics - I. Geometrical model. *Composite Structures*, 93(5):1424–1432, 2011.
- [2] O. Allix and L. Blanchard. Mesomodeling of delamination: towards industrial applications. *Composites Science and Technology*, 66(6):731–744, 2006.
- [3] H. Altenbach. Modelling of anisotropic behavior in fiber and particle reinforced composites. In T. Sadowski, editor, *Multiscale Modelling of Damage and Fracture Processes in Composite Materials*, pages 1–63. SpringerWienNewYork, 2005.
- [4] A. Anthoine. Derivation of the in-plane elastic characteristics of masonry through homogenization theory. *International Journal of Solids and Structures*, 32(2):137–163, 1995.
- [5] A&P Technology. Case studies, June 2013. URL www.braider.com.
- [6] C. Ayranci and J. Carey. 2D braided composites: A review for stiffness critical applications. *Composite Structures*, 85(1):43–58, 2008.
- [7] P. Badel, E. Vidal-Sallé, E. Maire, and P. Boisse. Simulation and tomography analysis of textile composite reinforcement deformation at the mesoscopic scale. *Composites Science and Technology*, 68(12):2433–2440, 2008.
- [8] E. Barbero, P. Lonetti, and K. Sikkil. Finite element continuum damage modeling of plain weave reinforced composites. *Composites Part B: Engineering*, 37(2-3):137–147, 2006.

- [9] E. Barbero, G. Sgambitterra, A. Adumitroaie, and X. Martinez. A discrete constitutive model for transverse and shear damage of symmetric laminates with arbitrary stacking sequence. *Composite Structures*, 93(2):1021–1030, 2011.
- [10] D. Blackketter, D. Walrath, and A. Hansen. Modeling damage in a plain weave fabric-reinforced composite material. *Journal of Composites Technology and Research*, 15(2):136–142, 1993.
- [11] H. J. Böhm. A Short Introduction to Continuum Micromechanics. In H. J. Böhm, editor, *Mechanics of Microstructured Materials*, volume 464 of *CISM courses and lectures*, pages 1–40. Springer-Verlag Wien New York, 2004.
- [12] J.-H. Byun. The analytical characterization of 2-D braided textile composites. *Composites Science and Technology*, 60(5):705–716, 2000.
- [13] P. P. Camanho, C. G. Davila, and M. F. de Moura. Numerical Simulation of Mixed-Mode Progressive Delamination in Composite Materials. *Journal of Composite Materials*, 37(16):1415–1438, 2003.
- [14] K. M. Charlebois, R. Boukhili, O. Zebdi, F. Trochu, and A. Gasmi. Evaluation of the physical and mechanical properties of braided fabrics and their composites. *Journal of Reinforced Plastics and Composites*, 24(14):1539–1554, 2005.
- [15] L. Chen, X. M. Tao, and C. L. Choy. Mechanical analysis of 3-D braided composites by the finite multiphase element method. *Composites Science and Technology*, 59(16):2383–2391, 1999.
- [16] C. Cherif, editor. *Textile Werkstoffe für den Leichtbau: Techniken – Verfahren – Materialien – Eigenschaften (German Edition)*. Springer, 2011 edition, 8 2011.
- [17] J. Cichosz, T. Wehrkamp-Richter, R. Hinterhoelzl, and K. Drechsler. Material modeling of 2x2 braided composites using a beam approach. In *Proceedings of the 15th European Conference on Composite Materials (ECCM15)*, number 1945, page 8, 2012.
- [18] J. Cichosz, J. Bückle, R. Hinterhölzl, and W. M. Predicting the constitutive behavior of biaxial braided composites using beam unit cells. In *Proceedings of*

- the 19th International Conference on Composite Materials (ICCM19)*, page 9, 2013.
- [19] J. Cichosz, P. Huber, and R. Hinterhölzl. Off-axis testing of biaxial braided composites. In *Proceedings of the TEXCOMP-11 CONFERENCE*, Leuven, 2013.
- [20] E. Coenen, V. Kouznetsova, and M. Geers. Novel boundary conditions for strain localization analyses in microstructural volume elements. *International Journal for Numerical Methods in Engineering*, 90(1):1–21, 2012.
- [21] E. W. C. Coenen, V. G. Kouznetsova, and M. G. D. Geers. Computational homogenization for heterogeneous thin sheets. *International Journal for Numerical Methods in Engineering*, 83(8-9):1180–1205, 2010.
- [22] B. Cox, W. Carter, and N. Fleck. A binary model of textile composites—I. formulation. *Acta Metallurgica et Materialia*, 42(10):3463–3479, 1994.
- [23] B. N. Cox and G. Flanagan. Handbook of analytical methods for textile composites. Technical report, NASA Contractor Report 4750, 1997.
- [24] J. J. Crookston. Modelling mechanical performance including damage development for textile composites using a grid-based finite element method with adaptive mesh refinement. *8th International Conference on Textile Composites (TEXCOMP-8)*, Nottingham, UK, 2006.
- [25] J. J. Crookston, A. C. Long, and I. A. Jones. A summary review of mechanical properties prediction methods for textile reinforced polymer composites. *Proceedings of the Institution of Mechanical Engineers, Part L: Journal of Materials Design and Applications*, 219(2):91–109, 2005.
- [26] R. Cuntze and A. Freund. The predictive capability of failure mode concept-based strength criteria for multidirectional laminates. *Composites Science and Technology*, 64:343–377, 2004.
- [27] Cytec. Cycom 977-2 toughened epoxy resin – technical datasheet, 2002.
- [28] M. Dadkhah, J. Flintoff, T. Kniveton, and B. Coxt. Simple models for triaxially braided composites. *Composites*, 26:561–577, 1995.

- [29] E. D'Amato. Finite element modeling of textile composites. *Composite Structures*, 54(4):467–475, 2001.
- [30] C. Davila, P. Camanho, and A. Turon. Cohesive elements for shells. Technical report, NASA/TM-2007-214869, 2007.
- [31] N. De Carvalho, S. Pinho, and P. Robinson. A mathematical framework for reducing the domain in the mechanical analysis of periodic structures. *ArXiv e-prints*, Dec. 2010.
- [32] N. De Carvalho, S. Pinho, and P. Robinson. Reducing the domain in the mechanical analysis of periodic structures, with application to woven composites. *Composites Science and Technology*, 71(7):969–979, 2011.
- [33] N. De Carvalho, S. Pinho, and P. Robinson. Numerical modelling of woven composites: Biaxial loading. *Composites Part A: Applied Science and Manufacturing*, 43(8):1326–1337, 2012.
- [34] F. Desplentere, S. Lomov, D. Woerdeman, I. Verpoest, M. Wevers, and A. Bogdanovich. Micro-ct characterization of variability in 3d textile architecture. *Composites Science and Technology*, 65(13):1920–1930, 2005.
- [35] L. P. Djukic, I. Herszberg, W. R. Walsh, G. A. Schoeppner, B. G. Prusty, and D. W. Kelly. Contrast enhancement in visualisation of woven composite tow architecture using a microct scanner. part 1: Fabric coating and resin additives. *Composites Part A: Applied Science and Manufacturing*, 40(5):553–565, 2009.
- [36] M. V. Donadon, B. G. Falzon, L. Iannucci, and J. M. Hodgkinson. A 3-D micromechanical model for predicting the elastic behaviour of woven laminates. *Composites Science and Technology*, 67(11-12):2467–2477, 2007.
- [37] D. Durville. Simulation of the mechanical behaviour of woven fabrics at the scale of fibers. *International Journal of Material Forming*, 3:1241–1251, 2010.
- [38] T. Flatscher. *A Constitutive Model for the Elasto-Plasto-Damage Ply Behavior in Laminated FRP Composites: Its Development, Implementation, and Application in FEM Simulations*. PhD thesis, Vienna University of Technology, Austria, 2010. (also published as: VDI Fortschritt-Berichte VDI Reihe 18 Nr. 326. VDI-Verlag, Düsseldorf).

- [39] T. Flatscher and H. E. Pettermann. A constitutive model for fiber-reinforced polymer plies accounting for plasticity and brittle damage including softening - implementation for implicit FEM. *Composite Structures*, 93(9):2241–2249, 2011.
- [40] T. Flatscher, C. Schuecker, and H. E. Pettermann. Prediction of plastic strain accumulation in continuous fiber reinforced laminates by a constitutive ply model. *International Journal of Fracture*, 158:145–156, 2009.
- [41] T. Flatscher, M. Wolfahrt, G. Pinter, and H. E. Pettermann. Simulations and experiments of open hole tension tests — assessment of intra-ply plasticity, damage, and localization. *Composites Science and Technology*, 72(10):1090–1095, 2012.
- [42] M. Fouinneteau. *Damage and failure modelling of carbon and glass 2D braided composites*. PhD thesis, Cranfield University, 2006.
- [43] J. Gager and H. E. Pettermann. Elasto-plasto-damage modeling of FRP fabrics – a shell unit cell approach. In R. Rolfes and E. Jansen, editors, *ECCOMAS 3rd Thematic Conference on the Mechanical Response of Composites 2011*, pages 279–286. Leibniz University Hannover, Germany, 2011.
- [44] J. Gager and H. E. Pettermann. Numerical homogenization of textile composites based on shell element discretization. *Composites Science and Technology*, 72(7):806–812, 2012.
- [45] J. Gager and H. E. Pettermann. Multi-layered textile composites – a shell element based homogenisation approach. In *Proceedings of the 6th European Congress on Computational Methods in Applied Sciences and Engineering (ECCOMAS 2012)*. Vienna University of Technology, Austria, 2012.
- [46] J. Gager and H. E. Pettermann. Assessing the operation load range of non-linear textile composites by means of stress envelopes. In *Proceedings of the 15th European Conference on Composite Materials (ECCM15)*, number 1837, page 8, 2012.

- [47] J. Gager and H. E. Pettermann. Shell element based homogenization of textile composites. In *8th European Solid Mechanics Conference (ESMC2012)*, extended abstract, 2012.
- [48] J. Gager, M. Meindlhumer, M. Schwab, and H. E. Pettermann. Numerically predicted damage and failure envelopes of composites featuring nonlinear material behavior. In *Proceedings of the 19th International Conference on Composite Materials (ICCM19)*, page 9, 2013.
- [49] V. Ganesh and N. Naik. Failure behavior of plain weave fabric laminates under on-axis uniaxial tensile loading: I-laminate geometry. *Journal of Composite Materials*, 30:1748–1778, 1996.
- [50] F. Gao, L. Boniface, S. Ogin, P. Smith, and R. Greaves. Damage accumulation in woven-fabric cfrp laminates under tensile loading: Part 1. observations of damage accumulation. *Composites Science and Technology*, 59(1):123–136, 1999.
- [51] M. R. Garnich and V. M. K. Akula. Review of degradation models for progressive failure analysis of fiber reinforced polymer composites. *Applied Mechanics Reviews*, 62(1):010801, 2009.
- [52] M. Geers, E. Coenen, and V. Kouznetsova. Multi-scale computational homogenization of structured thin sheets. *Modelling and Simulation in Materials Science and Engineering*, 15(4):S393, 2007.
- [53] M. Geers, V. Kouznetsova, and W. Brekelmans. Multi-scale computational homogenization: Trends and challenges. *Journal of Computational and Applied Mathematics*, 234(7):2175–2182, 2010.
- [54] I. Gitman. *Representative Volumes and Multi-Scale Modelling of Quasi-Brittle Materials*. PhD thesis, Technische Universiteit te Delft, Delft, Netherlands, 2006.
- [55] B. Gommers, I. Verpoest, and P. V. Houtte. The mori-tanaka method applied to textile composite materials. *Acta Materialia*, 46(6):2223–2235, 1998.

- [56] C. González and J. LLorca. Mechanical behavior of unidirectional fiber-reinforced polymers under transverse compression: Microscopic mechanisms and modeling. *Composites Science and Technology*, 67(13):2795–2806, 2007.
- [57] D. Goyal. Analysis of 2x2 braided composites. Master’s thesis, Texas A&M University, 2003.
- [58] D. Goyal. *Analysis of linear elasticity and non-linearity due to plasticity and material damage in woven and biaxial braided composites*. PhD thesis, Texas A&M University, US, 2007.
- [59] D. Goyal and J. D. Whitcomb. Analysis of stress concentrations in 2×2 braided composites. *Journal of Composite Materials*, 40(6):533–546, 2006.
- [60] D. Goyal, X. Tang, J. D. Whitcomb, and A. D. Kelkar. Effect of various parameters on effective engineering properties of 2×2 braided composites. *Mechanics of Advanced Materials and Structures*, 12(2):113–128, 2005.
- [61] I. Guimatsia, J. Ankersen, and G. Davies. Cohesive elements: their problems and how to avoid them. *Composites 2009, 2nd ECCOMAS Thematic Conference on the Mechanical Response of Composites*, 2009.
- [62] A. Hallal, R. Younes, and F. Fardoun. Review and comparative study of analytical modeling for the elastic properties of textile composites. *Composites Part B: Engineering*, 50(0):22–31, 2013.
- [63] Z. Hashin. Failure criteria for unidirectional fiber composites. *Journal of Applied Mechanics*, 47(2):329–334, 1980.
- [64] *Abaqus/Standard User’s Manual, Version 6.12*. Hibbit, Karlsson & Sorensen Inc., Pawtucket, RI, USA, 2012.
- [65] R. Hill. Elastic properties of reinforced solids: Some theoretical principles. *Journal of the Mechanics and Physics of Solids*, 11(5):357–372, 1963.
- [66] Z. m. Huang. The mechanical properties of composites reinforced with woven and braided fabrics. *Composites Science and Technology*, 60(4):479–498, 2000.
- [67] U. Icardi, S. Locatto, and A. Longo. Assessment of recent theories for predicting failure of composite laminates. *Applied Mechanics Reviews*, 60(2):76–86, 2007.

- [68] T. Ishikawa and T.-W. Chou. Elastic behavior of woven hybrid composites. *Journal of Composite Materials*, 16:2–19, 1982.
- [69] D. S. Ivanov, S. V. Lomov, S. G. Ivanov, and I. Verpoest. Stress distribution in outer and inner plies of textile laminates and novel boundary conditions for unit cell analysis. *Composites Part A: Applied Science and Manufacturing*, 41(4):571–580, 2010.
- [70] D. S. Ivanov, S. G. Ivanov, S. V. Lomov, and I. Verpoest. Unit cell modelling of textile laminates with arbitrary inter-ply shifts. *Composites Science and Technology*, 72(1):14–20, 2011.
- [71] N. Jēkabsons and J. Byström. On the effect of stacked fabric layers on the stiffness of a woven composite. *Composites Part B: Engineering*, 33(8):619–629, 2002.
- [72] W.-G. Jiang and S. Hallett. Development of domain superposition technique for the modelling of woven fabric composites. In P. P. Camanho, C. G. Dávila, S. T. Pinho, and J. J. C. Remmers, editors, *Mechanical Response of Composites*, pages 281–291. Springer, 2008.
- [73] R. M. Jones. *Mechanics of Composite Materials*. Taylor & Francis Inc., Philadelphia, PA, USA, second edition, 1999.
- [74] M. Kashtalyan and C. Soutis. Analysis of composite laminates with intra- and interlaminar damage. *Progress in Aerospace Sciences*, 41(2):152–173, 2005.
- [75] M. Kästner, G. Haasemann, J. Brummund, and V. Ulbricht. Computation of effective stiffness properties for textile-reinforced composites using X-FEM. In P. P. Camanho, C. G. Dávila, S. T. Pinho, and J. J. C. Remmers, editors, *Mechanical Response of Composites*, pages 261–279. Springer, 2008.
- [76] M. Kästner, G. Haasemann, and V. Ulbricht. Multiscale XFEM-modelling and simulation of the inelastic material behaviour of textile-reinforced polymers. *International Journal for Numerical Methods in Engineering*, 86(4-5):477–498, 2011.
- [77] M. G. Kollegal and S. Sridharan. A Simplified Model for Plain Woven Fabrics. *Journal of Composite Materials*, 34(20):1756–1786, 2000.

- [78] V. Kouznetsova, M. G. D. Geers, and W. A. M. Brekelmans. Multi-scale constitutive modelling of heterogeneous materials with a gradient-enhanced computational homogenization scheme. *International Journal for Numerical Methods in Engineering*, 54(8):1235–1260, 2002.
- [79] R. Krueger. Virtual crack closure technique: History, approach, and applications. *Applied Mechanics Reviews*, 57(2):109–143, 2004.
- [80] P. Ladeveze and E. LeDantec. Damage modelling of the elementary ply for laminated composites. *Composites Science and Technology*, 43(3):257–267, 1992.
- [81] I. Lapczyk and J. A. Hurtado. Progressive damage modeling in fiber-reinforced materials. *Composites Part A: Applied Science and Manufacturing*, 38(11):2333–2341, 2007.
- [82] B. Le Page, F. Guild, S. Ogin, and P. Smith. Finite element simulation of woven fabric composites. *Composites Part A: Applied Science and Manufacturing*, 35(7–8):861–872, 2004.
- [83] A. Lobner. Auswirkungen von Unsicherheiten auf das mechanische Verhalten von Gewebelaminaten. Master’s thesis, Vienna University of Technology, Austria, 2009.
- [84] S. V. Lomov, G. Huysmans, Y. Luo, R. S. Parnas, A. Prodromou, I. Verpoest, and F. R. Phelan. Textile composites: modelling strategies. *Composites Part A: Applied Science and Manufacturing*, 32(10):1379–1394, 2001.
- [85] S. V. Lomov, I. Verpoest, T. Peeters, D. Roose, and M. Zako. Nesting in textile laminates: geometrical modelling of the laminate. *Composites Science and Technology*, 63(7):993–1007, 2003.
- [86] S. V. Lomov, D. S. Ivanov, I. Verpoest, M. Zako, T. Kurashiki, H. Nakai, and S. Hirose. Meso-FE modelling of textile composites: Road map, data flow and algorithms. *Composites Science and Technology*, 67(9):1870–1891, 2007.
- [87] C. Marte. Untersuchung von 2/2-Twill-Gewebe Laminate mit Hilfe von 3D-Finite Elemente Einheitszellen. Master’s thesis, Vienna University of Technology, Austria, 2004.

- [88] A. Matzenmiller, J. Lubliner, and R. L. Taylor. A constitutive model for anisotropic damage in fiber-composites. *Mechanics of Materials*, 20:125–152, 1995.
- [89] J. A. Mayugo, E. J. Barbero, and D. Trias. Meso-mechanical finite element modeling of fabric reinforced composites. In *ECCOMAS*, 2007.
- [90] M. Meindlhumer. Schädigungs- und Versagensvorhersage von Gewebelaminaten durch mechanismenbasierte Hüllflächen. Master's thesis, Vienna University of Technology, Austria, 2013.
- [91] A. Miravete, J. Bielsa, A. Chiminelli, J. Cuartero, S. Serrano, N. Tolosana, and R. G. de Villoria. 3d mesomechanical analysis of three-axial braided composite materials. *Composites Science and Technology*, 66(15):2954–2964, 2006.
- [92] N. Moës, M. Cloirec, P. Cartraud, and J. F. Remacle. A computational approach to handle complex microstructure geometries. *Computer Methods in Applied Mechanics and Engineering*, 192(28-30):3163–3177, 2003.
- [93] T. Möller and B. Trumbore. Fast, minimum storage ray-triangle intersection. *Journal of Graphics Tools*, 2(1):21–28, 1997.
- [94] N. Naik and V. Ganesh. Failure behavior of plain weave fabric laminates under on-axis uniaxial tensile loading: II-Analytical predictions. *Journal of Composite Materials*, 30:1779–1822, 1996.
- [95] N. Naik and P. Shembekar. Elastic behavior of woven fabric composites: I-lamina analysis. *Journal of Composite Materials*, 26:2196–2225, 1992.
- [96] R. A. Naik. Analysis of woven and braided fabric reinforced composites. Technical report, National Aeronautics and Space Administration, 1994.
- [97] A. T. Nettles and E. J. Biss. Low temperature mechanical testing of carbon-fiber/epoxy-resin composite materials. Technical report, NASA TP-3663, 1996.
- [98] T. D. Nguyen. Elastic properties of large tow 2-d braided composites by numerical and analytical methods. Technical report, Lawrence Livermore National Laboratory, 1998.

- [99] V. P. Nguyen, M. Stroeven, and L. J. Sluys. Multiscale continuous and discontinuous modeling of heterogeneous materials: A review on recent developments. *Journal of Multiscale Modelling*, 03(04):229–270, 2011.
- [100] J. F. Nye. *Physical Properties of Crystals: Their Representation by Tensors and Matrices*. Oxford University Press, USA, 1985.
- [101] B. C. Owens, J. D. Whitcomb, and J. Varghese. Effect of finite thickness and free edges on stresses in plain weave composites. *Journal of Composite Materials*, 44(6):675–692, 2010.
- [102] D. H. Pahr and F. G. Rammerstorfer. Experimental and numerical investigations of perforated cfr woven fabric laminates. *Composites Science and Technology*, 64(9):1403–1410, 2004.
- [103] D. H. Pahr and F. G. Rammerstorfer. Buckling of honeycomb sandwiches: Periodic finite element considerations. *Computer Modeling in Engineering and Sciences*, 12(3):229–241, 2006.
- [104] A. Pickett and M. Fouinneteau. Material characterisation and calibration of a meso-mechanical damage model for braid reinforced composites. *Composites Part A: Applied Science and Manufacturing*, 37(2):368–377, 2006.
- [105] S. T. Pinho, C. G. Dávila, P. P. Camanho, L. Iannucci, and P. Robinson. Failure models and criteria for FRP under in-plane or three-dimensional stress states including shear non-linearity. Technical report, NASA/TM-2005-213530, 2005.
- [106] P. Potluri and A. Manan. Mechanics of non-orthogonally interlaced textile composites. *Composites Part A: Applied Science and Manufacturing*, 38(4):1216–1226, 2007.
- [107] E. Potter, S. T. Pinho, P. Robinson, L. Iannucci, and A. McMillan. Mesh generation and geometrical modelling of 3d woven composites with variable tow cross-sections. *Computational Materials Science*, 51(1):103–111, 2012.
- [108] A. Puck. *Festigkeitsanalyse von Faser-Matrix-Laminaten: Modelle für die Praxis*. Carl Hanser Verlag, München; Wien, 1996.

- [109] A. Puck and H. Schürmann. Failure analysis of FRP laminates by means of physically based phenomenological models. *Composites Science and Technology*, 58(7):1045–1067, 1998.
- [110] A. Puck and H. Schürmann. Failure analysis of FRP laminates by means of physically based phenomenological models. *Composites Science and Technology*, 62(12–13):1633–1662, 2002.
- [111] A. Puck, J. Kopp, and M. Knops. Guidelines for the determination of the parameters in puck’s action plane strength criterion. *Composites Science and Technology*, 62(3):371–378, 2002.
- [112] R. G. Rinaldi, M. Blacklock, H. Bale, M. R. Begley, and B. N. Cox. Generating virtual textile composite specimens using statistical data from micro-computed tomography: 3d tow representations. *Journal of the Mechanics and Physics of Solids*, 60(8):1561–1581, 2012.
- [113] M. Samimi, J. van Dommelen, and M. Geers. An enriched cohesive zone model to deal with brittle interfaces. In ESIS, editor, *Fracture of Materials and Structures from Micro to Macro Scales*, 2010.
- [114] C. Schillfahrt. Bestimmung ausgewählter mechanischer Eigenschaften sowie der monotonen und zyklischen interlaminaren Risszähigkeit von gewickelten und geflochtenen Kohlenstofffaserverbundwerkstoffen. Master’s thesis, Montanuniversitaet Leoben, 2012.
- [115] M. Schubert. Vergleich eines Resin Transfer Moulding Exopoxidharzsystems mit einem Prepregharzsystem. In *17. Symposium "Verbundwerkstoffe und Werkstoffverbunde" der DGM*, 2009.
- [116] C. Schuecker. *Mechanism based modeling of damage and failure in fiber reinforced polymer laminates*. PhD thesis, Vienna University of Technology, Austria, 2005. (also published as: VDI Fortschritt-Berichte VDI Reihe 18 Nr. 303. VDI-Verlag, Düsseldorf).
- [117] C. Schuecker and H. E. Pettermann. Constitutive ply damage modeling, FEM implementation, and analyses of laminated structures. *Computers & Structures*, 86(9):908–918, 2008.

- [118] C. Schuecker, C. G. Dávila, and C. R. A. Comparison of damage models for predicting the non-linear response of laminates under matrix dominated loading conditions. Technical report, NASA/TP-2010-216856, 2010.
- [119] M. Schwab. Prediction of energy dissipation due to material nonlinearities and its application to textile composites. Master's thesis, Vienna University of Technology, Austria, 2013. (to be submitted).
- [120] D. Scida, Z. Aboura, M. L. Benzeggagh, and E. Bocherens. A micromechanics model for 3D elasticity and failure of woven-fibre composite materials. *Composites Science and Technology*, 59(4):505–517, 1999.
- [121] S. Z. Sheng and S. V. Hoa. Three dimensional micro-mechanical modeling of woven fabric composites. *Journal of Composite Materials*, 35:1701–1729, 2001.
- [122] D. Shepard. A two-dimensional interpolation function for irregularly-spaced data. In *Proceedings of the 1968 23rd ACM national conference*, ACM '68, pages 517–524, New York, NY, USA, 1968. ACM.
- [123] M. Sherburn. *Geometric and Mechanical Modelling of Textiles*. PhD thesis, University of Nottingham, UK, 2007.
- [124] S. Song, A. M. Waas, K. W. Shahwan, X. Xiao, and O. Faruque. Braided textile composites under compressive loads: Modeling the response, strength and degradation. *Composites Science and Technology*, 67(15-16):3059–3070, 2007.
- [125] A. Steinböck. Entwicklung einer Berechnungsmethode für Saugwalzen in Papiermaschinen. Master's thesis, Johannes Kepler University Linz, 2006.
- [126] P. Tan, L. Tong, and G. P. Steven. Modelling for predicting the mechanical properties of textile composites—a review. *Composites Part A: Applied Science and Manufacturing*, 28(11):903–922, 1997.
- [127] X. Tang, J. D. Whitcomb, A. D. Kelkar, and J. Tate. Progressive failure analysis of 2×2 braided composites exhibiting multiscale heterogeneity. *Composites Science and Technology*, 66(14):2580–2590, 2006.

- [128] J. S. Tate, A. D. Kelkar, and J. D. Whitcomb. Effect of braid angle on fatigue performance of biaxial braided composites. *International Journal of Fatigue*, 28(10):1239–1247, 2006.
- [129] I. Temizer and T. Zohdi. A numerical method for homogenization in non-linear elasticity. *Computational Mechanics*, 40(2):281–298, 2007.
- [130] K.-H. Tsai, C.-L. Hwan, W.-L. Chen, and C.-H. Chiu. A parallelogram spring model for predicting the effective elastic properties of 2D braided composites. *Composite Structures*, 83(3):273–283, 2008.
- [131] S. W. Tsai and E. M. Wu. A general theory of strength for anisotropic materials. *Journal of Composite Materials*, 5(1):58–80, 1971.
- [132] A. Turon, C. Dávila, P. Camanho, and J. Costa. An engineering solution for mesh size effects in the simulation of delamination using cohesive zone models. *Engineering Fracture Mechanics*, 74(10):1665–1682, 2007.
- [133] W. Van Paepegem, I. De Baere, and J. Degrieck. Modelling the nonlinear shear stress–strain response of glass fibre-reinforced composites. part II: Model development and finite element simulations. *Composites Science and Technology*, 66(10):1465–1478, 2006.
- [134] W. Van Paepegem, I. De Baere, and J. Degrieck. Modelling the nonlinear shear stress–strain response of glass fibre-reinforced composites. part I: Experimental results. *Composites Science and Technology*, 66(10):1455–1464, 2006.
- [135] G. van Rossum and F. Drake. *Python Reference Manual*. PythonLabs, 2001. URL <http://www.python.org>.
- [136] A. Vanaerschot, B. N. Cox, S. V. Lomov, and D. Vandepitte. Stochastic framework for quantifying the geometrical variability of laminated textile composites using micro-computed tomography. *Composites Part A: Applied Science and Manufacturing*, 44:122–131, 2013.
- [137] A. Vanaerschot, B. N. Cox, S. V. Lomov, and D. Vandepitte. Stochastic multi-scale modelling of textile composites based on internal geometry variability. *Computers & Structures*, 122:55–64, 2013.

- [138] I. Verpoest and S. V. Lomov. Virtual textile composites software WiseTex: Integration with micro-mechanical, permeability and structural analysis. *Composites Science and Technology*, 65:2563–2574, 2005.
- [139] Y. Wang and X. Sun. Digital-element simulation of textile processes. *Composites Science and Technology*, 61(2):311–319, 2001.
- [140] M. Whiteside and S. Pinho. Stochastic modelling of woven composites. In *Proceedings of the 15th European Conference on Composite Materials (ECCM15)*, 2012.
- [141] G. Wimmer. *Computational Methods for the Prediction of Emergence and Growth of Delaminations in Laminated Composite Components*. PhD thesis, Vienna University of Technology, Austria, 2009. (also published as: VDI Fortschritt-Berichte VDI Reihe 18 Nr. 320. VDI-Verlag, Düsseldorf).
- [142] K. Woo and J. D. Whitcomb. A post-processor approach for stress analysis of woven textile composites. *Composites Science and Technology*, 60(5):693–704, 2000.
- [143] J. Xu, B. Cox, M. McGlockton, and W. Carter. A binary model of textile composites–II. The elastic regime. *Acta Metallurgica et Materialia*, 43(9):3511–3524, 1995.
- [144] Q. Yang and B. Cox. Predicting failure in textile composites using the Binary Model with gauge-averaging. *Engineering Fracture Mechanics*, 77(16):3174–3189, 2010.